BAND GAP ENGINEERING OF METAL OXIDE (WO$_3$, MoO$_3$) THIN FILMS THROUGH ALLOYING WITH CADMIUM TELLURIDE

BY

Abdulmajeed Hasan Yahya Hendi

A Dissertation Presented to the

DEANSHIP OF GRADUATE STUDIES

KING FAHD UNIVERSITY OF PETROLEUM & MINERALS

DHAHRAN, SAUDI ARABIA

In Partial Fulfillment of the
Requirements for the Degree of

DOCTOR OF PHILOSOPHY

In

PHYSICS

December 2016

KING FAHD UNIVERSITY OF PETROLEUM & MINERALS

DHAHRAN- 31261, SAUDI ARABIA

DEANSHIP OF GRADUATE STUDIES

This thesis, written by **Abdulmajeed Hasan Yahya Hendi** under the direction
of his thesis advisor and approved by his thesis committee, has been presented and
accepted by the Dean of Graduate Studies, in partial fulfillment of the requirements for
the degree of **DOCTOR OF PHILOSOPHY IN PHYSICS.**

11.12.2016

Prof. Mohammad Fayyad Al-Kuhaili
(Advisor)

12/12/2016

Prof. Sardar M. A. Durrani
(Co-Advisor)

Dr. Abdullah A. Al-Sunaidi
Department Chairman

11.12.2016

Prof. Khalil Ali Ziq
(Member)

Dr. Salam A. Zummo
Dean of Graduate Studies

Dec. 11, 2016

Prof. Akhtar A. Naqvi
(Member)

7/1/17

Date

Dr. Anwar Ul-Hamid
(Member)

DEDICATION

To the pillars of my life: my parents, my wife and my daughters, who are everything for me.

My beloved late father, who was the source of my inspiration, his continued prayers for me that were lined up with the word of Allah got answer.

My beloved mother, without your continued prayers I would not be able to make it.

My lovely wife Om Tasnim thanks for your love, understanding and support.

My darling daughters (Tasnim, Shaima, Omima and Noor), you are the secret of my happiness and success.

ACKNOWLEDGMENT

All thanks and praise is due to Allah (azzawajal) who created me, blessed me with health, as well as provided me with patience and ambition to achieve this research.

I acknowledge deeply my advisor Prof. Mohammad Fayyad Al-Kuhaili who guided me in this research. Thanks very much for giving me the opportunity to learn the research skills. There are not enough words to describe his feedback, patience and priceless support as well as his highly professional ethics. I shall remain grateful for him forever, I ask Allah to bless him with success and happiness in his whole life.

I would like to extend my thanks to my thesis committee, including Prof. Sardar Mohammad Ayub for his cooperation, encouragement, feedback and continuous support; Prof. Khalil Ali Ziq for his great and beneficial discussions related to my research that proved all the time fruitful; Dr. Mohammed M. Faiz, for his continuous support and priceless discussions as well as for providing me with access to Surface Science Laboratory for executing XPS measurements. Great thanks go to Prof. Akhtar A. Naqvi for his continued encouragement. I also appreciate the input of Dr. Anwar Ul-Hamid in this research as well as the access he gave me to investigate the structural properties of my samples in his laboratory is highly appreciated. I owe a debt of gratitude to the Physics Department, and the chairman Dr. Abdullah A. Al-Sunaidi for his continued support and encouragement.

TABLE OF CONTENTS

LIST OF FIGURES

LIST OF TABLES

LIST OF SYMBOLS

E_g : Band gap of semiconductor

T : Temperature

K : Kelvin

E_e : Energy of electron in a quantum level

$\vec{k}$: Wave vector

E_c : Conduction band energy

E_v : Valence band energy

h : Planck's constant

ν : Frequency

E_p : Energy of phonon

n_0 : Concentration of electrons in an intrinsic semiconductor at thermal equilibrium

p_0 : Concentration of holes in an intrinsic semiconductor at thermal equilibrium

E_F : Fermi level

k_B	:	Boltzmann constant
N_c	:	Effective density of states function in the conduction band
N_v	:	Effective density of states function in the conduction band
m_e^*	:	Effective mass of electron inside a crystal
m_p^*	:	Effective mass of hole inside a crystal
n_i	:	Intrinsic electrons concentration
p_i	:	Intrinsic holes concentration
E_{Fi}	:	Intrinsic Fermi level
E_{midgap}	:	Energy at the middle of the band gap
E_d	:	Donor energy level
E_a	:	Acceptor energy level
x	:	Concentration of dopant in the semiconductor alloy $A_{1-x}B_x$ alloy
a_{alloy}	:	Lattice constant of the semiconductor alloy $A_{1-x}B_x$
a_A	:	Lattice constant of semiconductor A
a_B	:	Lattice constant of semiconductor B

U_A	:	Potential of atom A in the crystal lattice
U_B	:	Potential of atom B in the crystal lattice
$E_{g,A}$	:	Band gap of semiconductor A
$E_{g,B}$	:	Band gap of semiconductor B
$E_{g,alloy}$	:	Band gap of the semiconductor alloy $A_{1-x}B_x$
b	:	Bowing factor in the bowing equation
α	:	Absorption coefficient
$\hbar$	:	Reduced Planck's constant
ω	:	Angular frequency
$W_{i \to f}$	:	Transition rate of electrons in a quantum system from an initial eigenstate to a final eigenstate
I	:	Light incident density
c	:	Speed of light
$\vec{E}$	:	Electric field
$\vec{B}$	:	Magnetic field
$\vec{A}$	:	Vector potential of the radiation field

$\vec{A}_0$	:	Amplitude of the wave
$\vec{r}$	:	Vector displacement
H_0	:	Hamiltonian
H'	:	Perturbing Hamiltonian
ρ	:	Electron density of states
e	:	Free electron charge
m_0	:	Free electron mass
m^*	:	The reduced mass of the electron-hole pair
C	:	Scaling factor in Tauc's equation
L	:	Spacing between diffracting plans
θ	:	Bragg angle
j	:	The order of diffracted x-ray beam
λ	:	Wavelength of the x-ray beam
E_i	:	Binding energy of the photoelectron emitted from the atom
E_k	:	Kinetic energy of the photoelectron emitted from the atom
Φ	:	Work function of the spectrophotometer

d	:	Film Thickness
n	:	Refractive index
t	:	Transmittance
t_{mni}	:	Wavelength corresponding to a minimum transmittance
λ_1	:	Wavelength corresponding to a minimum
λ_2	:	Wavelength corresponding to a maximum transmittance
E_p	:	Photon energy
η	:	A power factor in Tauc's equation describes the process
β	:	A constant in Tauc's equation
E_T	:	Band gap of pure CdTe
E_W	:	Band gap of pure WO3
E_M	:	Band gap of pure MoO3
a	:	A factor in the quadratic form of the bowing equation which is given by $a = E_T - E_W - b$
ξ^6	:	Ratio of W^{6+} to the total W in the film
ξ^5	:	Ratio of W^{5+} to the total W in the film

LIST OF ABBREVIATIONS

LEDs	:	Light Emitting Diodes
DC	:	Direct Current
RF	:	Radio Frequency
CVD	:	Chemical Vapor Deposition
PLD	:	Pulsed Laser Deposition
PLA	:	Pulsed Laser Ablation
SP	:	Spray Pyrolysis
ICD	:	Impregnation Decomposition Cycles
VCA	:	Virtual Crystal Approximation
at%	:	Atomic Percentage
wt%	:	Weight Percentage
mL	:	milliliter
mmol/L	:	millimoles per liter
sccm	:	standard cubic centimeters per minute

XRD	**:**	X-ray Diffraction
AFM	**:**	Atomic Force Microscope
UV	**:**	Ultra Violet
XPS	**:**	X-ray Photoelectron Spectroscopy
HSA	**:**	Hemispherical Electron Energy Analyzer
PGSTAT	**:**	Potentiostat/Galvanostat
PEC	**:**	Photoelectrochemical Cell
WE	**:**	Working Electrode
CE	**:**	Counter Electrode
RE	**:**	Reference Electrode
JCPDS	**:**	The Joint Committee on Powder Diffraction Standards
ICDD	**:**	The International Center for Diffraction Data

ABSTRACT

Full Name: Abdulmajeed Hasan Yahya Hendi

Thesis Title: Band Gap Engineering of Metal Oxide (WO_3, MoO_3) Thin Films through Alloying with Cadmium Telluride

Major Field: Physics

Date of Degree: December 2016

This study was concerned with the development of a synthesis technique based on thermal evaporation for engineering the band gap of some metal oxide semiconductors, namely tungsten oxide (WO_3) and molybdenum oxide (MoO_3) by alloying them with a narrow-band-gap II-VI semiconductor, specifically cadmium telluride (CdTe). In this study, thermal evaporation, which is considered to be one of the simplest methods for the deposition of thin films, was employed to fabricate widely-tuned band gaps of WO_3 and MoO_3 films by mixing them with specific concentrations of CdTe. The novelty of this technique was that the band gap engineering of these oxides required merely evaporation of a powder mixture of each oxide with controlled concentrations of CdTe. Such a study was attempted to provide the opportunity for tuning other wide band gap metal oxide semiconductors through mixing with different narrow band gap compounds.

First, the influence of CdTe concentration of 5%, 10%, 15%, 20% and 25% on the band gap of WO_3 thin films was studied. Second, the influence of CdTe concentration of 2%, 4%, 6%, 8% and 10% on the band gap of MoO_3 thin films was investigated. X-ray

diffraction showed that the obtained pure WO_3 and MoO_3 films had an amorphous structure, while CdTe thin films were polycrystalline. The addition of CdTe to WO_3 and MoO_3 did not improve their structures. However, at high CdTe concentrations, WO_3 thin films still had an amorphous phase but the polycrystalinity of CdTe was decreased. The films showed an increase in the surface roughness with the increase in CdTe concentration as revealed by atomic force microscopy. Optical analysis based on transmittance measurements revealed that the band gap of WO_3 thin film was significantly red-shifted due to alloying with CdTe. The band gap values of the fabricated films were found to decrease from 3.30 eV for pure WO_3 to 2.47 eV at CdTe concentrations of 25%. Similarly, a remarkable red-shift in the band gap of MoO_3 thin films through mixing with CdTe was observed. The band gap of the fabricated films was decreased from 2.90 to 2.60 eV as the CdTe concentration increased from 0% to 10%, respectively. The experimental variation of the band gap values with CdTe was described by the standard bowing quadratic equation for the whole range of CdTe concentration. The obtained results indicated that a wider portion of the visible spectrum can be harvested rather than only single wavelength, corresponding to the band gaps of pure WO_3 or MoO_3 thin films. Chemical analysis of pure WO_3 and MoO_3 films performed by X-ray photoelectron spectroscopy showed that a sub-stoichiometric $WO_{2.96}$ and an almost stoichiometric $MoO_{2.98}$ films were obtained. Depth profiling analysis of the films alloyed with CdTe confirmed a nonhomogeneous distribution of the constituents throughout the depth of the WO_3 alloyed films. However, the constituents were homogeneously distributed throughout the thickness of the MoO_3 alloyed films.

Photocurrent measurements showed a significant increase in the photocurrent response of the CdTe-alloyed WO_3 and the CdTe-alloyed MoO_3 films with the increase of the CdTe concentration due to the enhancement of the light absorption in the long wavelength region. The obtained results support the potential of these alloyed films for improving the photo-to-current conversion efficiency in the photovoltaic and photoelectrochemical solar cell applications.

ملخص الرسالة

الإســـــم: عبدالمجيد حسن يحي هندي

عنوان الرسالة: هندسة فجوة الطاقة لأغشية رقيقة من أكاسيد التنجستن و الموليبدينوم عن طريق خلطها مع تيلوريد الكادميوم

التخصـــص: فـيزيـــاء

تاريخ التخرج: ديسمبر 2016م

هذه الدراسة معنيه بتطوير تقنية لإنتاج أغشية رقيقة بالاعتماد على التبخير الحراري بغرض هندسة طاقة الفجوة لبعض من

أكاسيد المعادن شبه الموصلة بالتحديد أكسيد التنجستن وأكسيد الموليبدينوم عن طريق إشابتهما بشبه موصل – ينتمي إلى

المجموعة الثانية والسادسة في الجدول الدوري– ذو طاقة فجوة ضيقة يسمى بتيلوريد الكادميوم. في هذه الدراسة تم توظيف تقنية

التبخير الحراري – و التي تعتبر واحدة من أسهل الطرق لترسيب الأغشية الرقيقة – لهندسة فجوات الطاقة لأغشية رقيقة من أكسيد

التنجستن وأكسيد الموليبدينوم على مدى واسع وذلك بخلط تراكيز محددة من تيلوريد الكادميوم مع كل منهما. الجديد في هذه

التقنية يتمثل في سهولة هندسة فجوات الطاقة لهذه الأكاسيد والتي نتطلب فقط تبخير مسحوق خليط من كل أكسيد مع تيلوريد

الكادميوم حيث يتم التحكم بتراكيز تيلوريد الكادميوم للحصول على قيم مختلفة لفجوة الطاقة لهذه الأكاسيد. لقد حاولت هذه

الدراسة إتاحة الفرصة لتعديل أو هندسة فجوات الطاقة الواسعة لأكاسيد المعادن (شبه الموصلة) الأخرى من خلال خلطهم مع

مركبات مختلفة ذات فجوات طاقة ضيقة. أولا تم دراسة تأثير تراكيز مختلفة من تيلوريد الكادميوم (5٪، 10٪، 15٪، 20٪، 25٪) على فجوة الطاقة لأغشية رقيقة من أكسيد التنجستن. ثانيا تم دراسة تأثير تراكيز أخرى من تيلوريد الكادميوم (2٪, 4٪, 6٪, 8٪، 10٪) على فجوة الطاقة لأغشية رقيقة من أكسيد الموليبدينوم. الخواص البنيوية للأغشيه الرقيقه المصنعة تم فحصها باستخدام جهاز حيود الأشعة السينية بينما الخواص الشكلية فحصت باستخدام مجهر القوة الذرية. التحليل الكيميائي للأغشيه الرقيقه المصنعة تم إجراؤه باستخدام جهاز مطياف الأشعة السينية الالكتروضوئي أما القياسات البصرية فقد أجريت باستخدام المقياس الطيفي. إضافة إلى ذلك تم فحص إمكانية استخدام هذه الأغشية الرقيقة بعد هندسة (تعديل) فجوات طاقاتها في تطبيقات الطاقة الشمسية والخلايا الكهروكيمياضوئيه من خلال إجراء قياسات التيار الكهروضوئي بإستخدام جهاز (Potentiostat) للتأكد من مدى قدرتها على تحويل الطاقة الضوئيه إلى طاقة كهربائية.   التحاليل البنيوية أثبتت أن الأغشية الرقيقة المصنعة من أكسيد التنجستن و أكسيد الموليبدينوم كانت غير متبلوره (بلا شكل منتظم) بينما الأغشية الرقيقة المصنعة من تيلوريد الكادميوم كانت تمتلك الشكل البلوري.إضافة إلى ذلك فإن إضافة تراكيز مختلفة من تيلوريد الكادميوم إلى أكسيد التنجستن و أكسيد الموليبدينوم لم يحسن من الشكل البلوري لكل منهما. أظهرت التحاليل الشكلية زيادة في خشونة أسطح هذه الأغشية الرقيقة مع زيادة تركيز تيلوريد الكادميوم. أما التحاليل البصرية فقد أثبتت أن نفاذية الضوء في أفلام أكسيد التنجستن و أكسيد الموليبدينوم المخلوطة مع تيلوريد الكادميوم تناقصت مع زيادة تركيزالأخير وهذا يعود لزيادة الإمتصاص في هذه الأغشية الرقيقة نتيجة لزيادة تركيز مع تيلوريد الكادميوم. إضافة إلى ذلك لوحظت زياده عالية في معامل إمتصاص الضوء لهذه الأغشية الرقيقة مع زيادة تركيز تيلوريد الكادميوم نتيجة لقدرتة العالية على الإمتصاص. كذلك فجوة الطاقة في الأغشية الرقيقة المصنعة من أكسيد التنجستن حصل لها إزاحة ملحوظة باتجاه الطول الموجي الأحمر (أي تناقصت) خلال خلطها مع تيلوريد الكادميوم. قيم فجوة الطاقة لهذه الأغشية الرقيقة انخفضت من 3.30 إلكترون فولت عندما كان تركيز تيلوريدالكادميوم 0 ٪ إلى 2.47 إلكترون فولت عندما زاد تركيز تيلوريد الكادميوم إلى 25٪. و بالمثل، لوحظ أيضا إزاحة ملحوظة لفجوة الطاقة في الأغشية الرقيقة المصنعة من أكسيد الموليبدينوم باتجاه الطول الموجي الأحمر

نتيجة الخلط مع تيلوريد الكادميوم. وقد انخفضت فجوة الطاقة في هذه الأغشية الرقيقة من 2.90 إلى 2.60 إلكترون فولت عندما

زاد تركيز تيلوريد الكادميوم من 0% إلى 10%، على التوالي. و تشيرهذه النتائج إلى أن الأغشية الرقيقة لأكسيد التنجستن وأكسيد

الموليبدينوم المخلوطة مع تيلوريد الكادميوم يمكن توظيفها لإستغلال طاقة الضوء على مدى واسع في منطقة الطيف المرئي بدلا من

الإقتصار على طاقة طول موجي واحد (المتوافق مع فجوة الطاقة لأكسيد التنجستن أوأكسيد الموليبدينوم), وبالتالي يمكن توظيفها في

تطبيقات الطاقة الشمسية . وكشفت التحاليل الكيميائية أن الأغشية الرقيقة الغير مخلوطة مع تيلوريد الكادميوم عبارة عن مركبات من

أكسيد التنجستن و الموليبدينوم ($WO_{2.96}$ و$MoO_{2.98}$) بينما تحليل عمق الأغشية الرقيقة المخلوطة مع تيلوريد الكادميوم

أوضح أن المكونات (العناصر الكيميائية) موزعة بشكل غير متجانس على مدى عمق الأغشية الرقيقة المصنعة من أكسيد التنجستن

المخلوط مع تيلوريد الكادميوم بينما كانت موزعة بشكل متجانس في الأغشية الرقيقة المصنعة من أكسيد الموليبدينوم المخلوط مع

تيلوريد الكادميوم. علاوة على ذلك لم تكن النسبة الذرية (الوحدة) بين الكادميوم والتليورايد في تيلوريد الكادميوم محفوظة كذلك

النسبة الذرية للأكسجين إلى التنجستن و الموليبدينوم في مركب أكسيد التنجستن وأكسيد الموليبدينوم (3 إلى 1) محفوظة. و يمكن

أن تعزى مثل هذه النتيجة للتغير في الحالة الكيميائية بسبب تشعيع هذه الأغشية الرقيقة بأيونات الأرجون عند إجراء التحليل

الكيميائي لطبقات (عمق) هذه الأغشية الرقيقة. أخيرا القياسات الكهربائية أظهرت زيادة كبيره في التيار الكهروضوئي للأغشية الرقيقة

المصنعة من أكسيد التنجستن وأكسيد الموليبدينوم المخلوطة مع تيلوريد الكادميوم مع زيادة تركيز الأخير. هذه الزيادة في التيار ناتجة

عن تعزيز إمتصاص الأطوال الموجية الطويلة من منطقة الضوء المرئي. وقد لوحظ أن أفضل وأعلى قيمة لإستجابة التيار الكهروضوئي

كانت في الأغشية الرقيقة المصنعة من أكسيد التنجستن المخلوطة مع نسبة 20% من تركيز تيلوريدالكادميوم. من ناحية أخرى, زادت

إستجابة التيار الكهروضوئي باضطراد مع زيادة تركيز تيلوريدالكادميوم في الأغشية الرقيقة المصنعة من أكسيد الموليبدينوم المخلوطة

مع تيلوريد الكادميوم. هذه النتائج التي تم التوصل إليها تدعم إمكانية توظيف هذه السبائك من الأغشية الرقيقة لتحسين كفاءة تحويل

الضوء إلى تياركهربائي في الخلايا الشمسية والخلايا الكهروكيمياضوئية .

CHAPTER 1

INTRODUCTION and LITERATURE REVIEW

1.1 Introduction

Solids can be classified into three different categories: conductors, semiconductors and insulators. The electrical conductivity of a solid material is determined by the response of electrons to an applied electric field. According to the band theory of solids, the electrons occupy allowed energy bands separated by forbidden regions in which no electron orbital exists. The uppermost allowed band is fully filled at $T = 0$ K, and is known as the valence band. The next bottommost allowed band is known as the conduction band. The energy gap between these two bands is known as the band gap, denoted by E_g. The band gap results from the interaction of the ion core of the crystal in the semiconductor with the conduction electron wave [1]. Figure 1.1 shows the energy bands for the above three categories. A material behaves as a conductor when one or more bands are partially-filled with electrons and the neighboring bands (valence and conduction) overlap. The material behaves as a semiconductor if the allowed energy bands are either empty or filled, and the band gap is small. The material behaves as an insulator when the allowed energy bands are either empty or completely filled with electrons and the band gap is large [2,3].

	Conductors	Semiconductors	Insulators

Empty band

Conduction band — Partially filled — Empty band — $E_g > 5eV$

$E_g < 5eV$

Valence band

Lower filled band
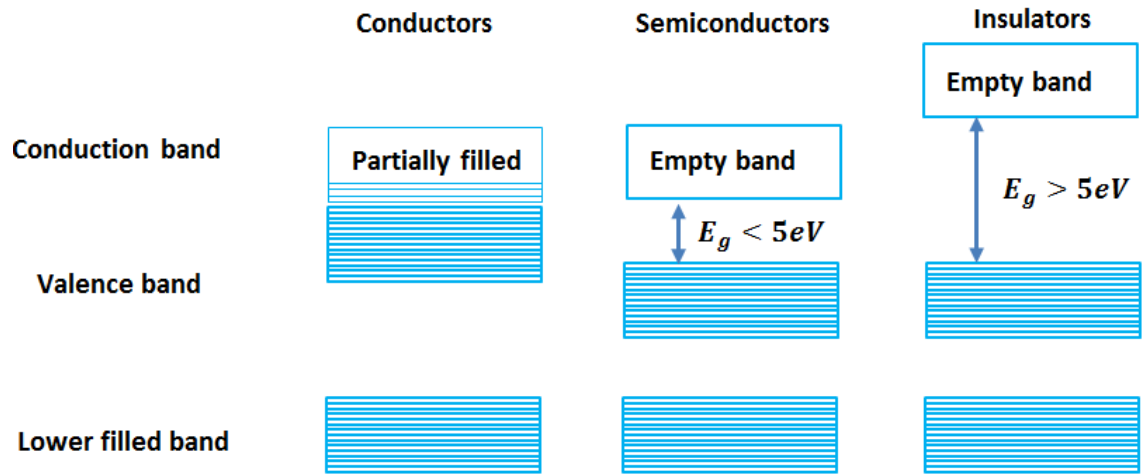
Fig. 1.1 A schematic diagram for allowed and forbidden energy bands in conductors, semiconductors and insulators.

In semiconductors, electrons can be excited from the valence band into the conduction band (leaving a hole state in the valence band) by absorbing thermal, electrical or optical energy. This process is called electron-hole pair production. Inversely, electron-hole recombination occurs when an electron is transferred from the conduction band into the valence band to fill an empty state. Thus, there are two kinds of charged particles that can carry electric current; electrons and holes. The above two processes represent the main key of the operation of all optoelectronic devices. The absorption of a photon results in the creation of an electron-hole pair. The mobile electrons resulting from the absorption can tune the electrical properties of the semiconductor, which results in the change of the photoconductivity of the material [4].

Semiconductors can be further classified into two types: direct band gap semiconductors and indirect band gap semiconductors. Figures 1.2 and Fig. 1.3 show plots of the energy of the electron (E_e) versus wave vector ($\vec{k}$) for both direct and indirect band gap semiconductors, respectively. The energy difference between the bottom of the conduction band (E_c) and the top of the valence band (E_v) varies with $\vec{k}$. The band gap of the semiconductor represents the energy difference between the bottom of the conduction band and the top of the valence band. If both the top of the valence band and the bottom of the conduction band are located at the same value of $\vec{k}$, the semiconductor is called a direct band gap semiconductor (Fig. 1.2). In such a semiconductor, the electron transition between these two bands results from the absorption or emission of a photon. If the value of $\vec{k}$ corresponding to the minimum energy of the conduction band is different from that corresponding to the maximum energy of the valence band, the semiconductor is called an indirect band gap semiconductor (Fig. 1.3). In this type of band structure, the transition between the minimum energy of the conduction band and the maximum energy of the valence band involves releasing a photon and a phonon. This phonon possesses a wave vector $\Delta\vec{k}$ (Fig. 1.3) that is equal to the difference in the $\vec{k}$ values of the two above-mentioned bands. In such a case, the energy gap of the semiconductor is given by

$$E_g = h\nu + E_p \tag{1.1}$$

where $h\nu$ is the energy of the emitted photon and E_p is the energy of the phonon **[2,3,5].**
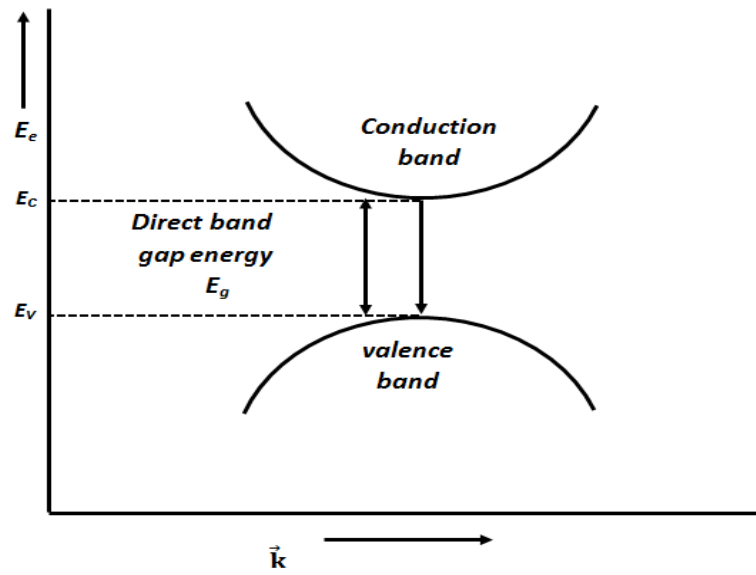
Fig. 1.2 Energy-momentum diagram for a direct band gap semiconductor.
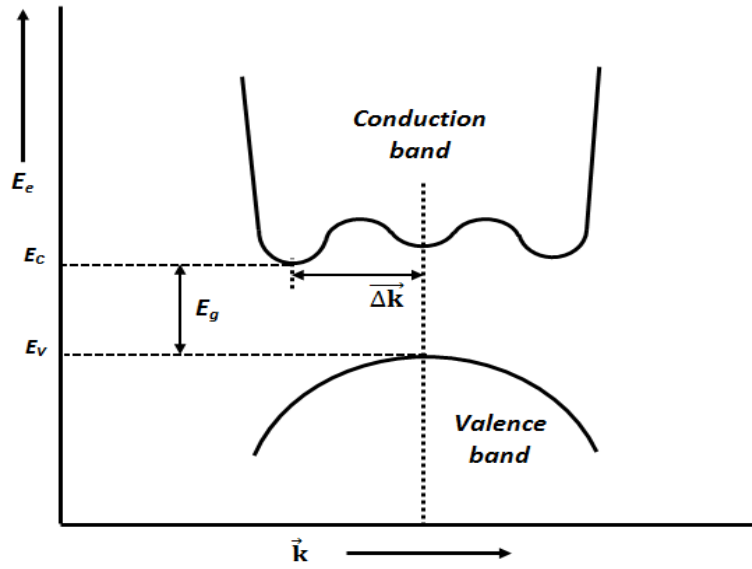
Fig. 1.3 Energy-momentum diagram for an indirect band gap semiconductor.

1.2 Band gap engineering

The band gap has a critical influence on the material properties and performance of photovoltaic and optoelectronic devices. Fabrication of optoelectronic devices such as light emitting diodes (LEDs) and detectors with widely varying properties, as well as lasers operating over the whole visible spectrum, requires engineering new materials that have their band gaps at custom-designed energies. Such tuning of the band gap is called band gap engineering [6,7]. Indeed, band gap engineering enables semiconductors such as Si, Ge, ZnSe, ZnS, GaN AlN and ZnO to be widely used in laser diodes, solar cells, and ultraviolet photodetectors [8]. In the field of high efficiency solar cells, there is a need for materials that are able to convert photon energy in the range of 2.3-2.5 eV. In the field of LEDs, a need exists for highly efficient green LEDs in the wavelength range 555-

5

560 nm [9]. The concept of band gap engineering has found various applications through fabrication of quantum dots of II-VI compound semiconductors. These include non-linear optical materials for X-ray detectors, thin film transistors with high field mobility, and LEDs in photovoltaic cells [10]. Band gap tunability of quantum dot materials, such as amorphous silicon quantum dots demonstrated that superior electrical and optical properties can be obtained [11]. Some applications like fiber-optic windows require binary semiconductors with band gaps of 0.95 eV and 0.82 eV (emission at 1.3 µm and 1.5 µm). Binary semiconducting systems do not exist at these wavelengths so one has to use alloys to engineer the band gap by varying composition [7]. Therefore, it is of great importance to engineer the band gap into the desirable values to fulfill specific optoelectronic applications.

1.3 Synthesis techniques for band gap engineering

Many techniques have been developed for band gap engineering of semiconductors. These include:

1.3.1 Quantum dots (nonostructures)

In this technique, very small particles of semiconducting materials having sizes of the order of nanometer (quantum dots) are fabricated. The band gap is blue-shifted with reduction of the nanostructure sizes. This increase is due to the modification of the band structure, narrowing of both the conduction and valance bands with decreasing the size of

the nanostructures. This is called the quantum confinement effect. Such an effect results in tuning the band gap with the changes in the quantum dots sizes [12,13].

1.3.2 Core/shell semiconductor heterostructures

This technique is based on alloying of core semiconductor quantum dots with shell nanostructures [12,14-16]. This leads to the formation of core/shell semiconductor hetrostructures, in which the conduction and valence bands of the core semiconductor is higher or lower than those of the shell [17]. Such a band is called type II- alignment, to be distinguished from type I-alignment. In type I-alignment, the band gap of the core semiconductor lies completely within the band gap of the shell so that the electrons and the holes overlap in the space inside the core semiconductor. In type II-alignment, the band gaps of the two materials (core and shell) overlap but no one totally encloses the other, leading to the separation of the two carriers (electrons and holes) between the core and the shell materials [16,18]. As a consequence, type II-alignment has reduced band gaps compared to those of the constituent core and shell components, which results in the tunability of the band gap of the core semiconductor [16,17,19].

1.3.3 Doping or alloying

This technique is based on the compositional variation via impurity doping or mixing of multiple semiconductors [20-22].

1.3.3.1 Doping

Doping involves adding very small concentrations of impurity atoms or compounds to the semiconductor material leading to changes in its properties [23], with corresponding tuning of the band gap. Doping can narrow or widen the band gap of the semiconductor, depending on the characteristics of the semiconductor and the dopant. For instance, subsitutional doping of semiconductor oxides with nitrogen leads to the narrowing of their band gaps due to the mixing of nitrogen p and oxygen p states [21]. On the other hand, widening of the band gap can be achieved by heavily n-type doping of a semiconductor, in which the donor electrons occupy states at the bottom of the conduction band leading to the blocking of low-energy transitions, which is known as the Burstein-Moss effect [24,25].

1.3.3.2 Alloying

A crucial technique for modifying the properties of materials is the fabrication of an alloy or solid solution. Alloys may be formed by mixing two or more solid materials [26]. In this technique, the band gap of the material is engineered by alloying multiple semiconductors [27]. An alloy with two semiconductor materials is termed a binary semiconductor alloy; one with three is a ternary semiconductor alloy; and one with four is a quaternary semiconductor alloy [28]. Binary semiconductors have fixed band gaps and lattice constants [29], while fabrication of a binary alloy results in the tuning of the band gap to take intermediate values between those of the parent compounds. For instance, the band gap of ZnSe-CdTe alloy was tuned precisely between the band gap of ZnSe (2.7 eV)

and that of CdTe (1.5 eV) by compositional variation of both ZnSe and CdTe [30]. In contrast to the fixed band gaps of the binary semiconductors, ternary alloys $A_xB_{1-x}C$, permit adjustment of the band gap and lattice constant. However, Quaternary alloys, $A_xB_{1-x}C_yD_{1-y}$ have an additional degree of freedom, and thus afford independent tuning of lattice constant and band gap over a limited range [29]. Additionally, wider band gap materials can be obtained via synthesis of nano-semiconductor alloys which is a better way than adjusting the sizes of the nano-compounds. This is because the latter leads to system instability, and requires more involved fabrication while modulating the composition can avoid these drawbacks [31].

1.4 Motivation

Wide band gap semiconductors exhibit emission /absorption wavelengths in the green, blue, and ultraviolet regions of the electromagnetic (EM) spectrum [32]. Among these, wide band gap metal oxide semiconductors have drawn growing interest, due to their unique optical, electrical, chemical and mechanical properties. Besides non toxicity, they are also of low cost and easy to fabricate [33]. These unique properties make them candidates for a variety of applications, including gas sensing [34,35], solar cells [36,37], water splitting [38,39], transparent conductors [40,41], as well as photocatalysis [42-45]. Although the large band gaps make metal oxides suitable for short wavelength optoelectronics [46-49], they are of limited applicability in the fabrication of photovoltaic devices.

9

Motivated by a necessity of extending their optoelectronics applications over a wide spectral range for solar and photovoltaic devices, I aim to achieve band gap engineering through alloying different wide band gap metal oxide semiconductors. Specifically, I propose to alloy the wide band gap metal oxides tungsten oxide (WO_3) and molybdenum oxide (MoO_3) with the narrow-band-gap II-VI compound semiconductor cadmium telluride (CdTe). To the best of my knowledge, mixing of these two oxides with CdTe has not been investigated. This field of knowledge would open the door for numerous applications of other wide band gap metal oxide semiconductors.

1.5 Materials selection and literature survey

1.5.1 Tungsten oxide (WO_3)

WO_3 is an *n*-type semiconductor which possesses different polymorphs such as monoclinic ($17 - 330 \, ^oC$), orthorhombic ($330–740 \, ^oC$,) and tetragonal ($> 740 \, ^oC$) [50,51]. Thin films of WO_3 have been extensively investigated for electrochromic devices [52-55], gas sensing [56-58], photoelectrochemical, photocatalytic and optoelectronic applications [59-62]. Amorphous WO_3 thin films have a wide indirect band gap value of 3.4 eV [46]. Consequently, these band gap values limit the photoabsorption to the near ultraviolet and blue regions of the EM spectrum. Thus, the ability to extend light harvesting further into the whole visible region (1.7-3.1 eV) requires the modulation of the band gap. Numerous researches have been devoted to modulate or engineer the band gap of WO_3.

Bose *et al.* succeeded in the tuning of the band gap of WO_3 thin films prepared by RF magnetron sputtering [63]. Band gap tuning of WO_3 was achieved by doping WO_3 with silver. The effect of silver addition on the phase formation and band gap modulation of WO_3 thin films was significant. It was found that the enhancement of silver content improved texturing and phase formation. Doping with silver content resulted in grain size increase, which in turn decreased the band gap of WO_3 thin films from 3.14 eV to 2.7 eV. It was also found that the thickness of the films increased with silver leading to a decrease in the transmittance of the films.

Band gap renormalization in titania (TiO_2) modified tungsten oxide thin films was studied by Lethy *et al.* [64]. In their work, pulsed laser ablation (PLA) was utilized for the fabrication of pure and titania doped WO_3 films. Optical measurements showed that the band gap values reduced from 3.17 eV for pure WO_3 films to 2.7 eV for 10 wt% titania modified WO_3 films. Consequently, the photoresponce of the modified films was enhanced in the visible region, indicating their promising applications in photovoltaic cells and photocatalysis. The reduction in the band gap of WO_3 thin films by introducing titania has been attributed to the lattice disorder of the WO_3 matrix as titania additives increased.

Haijin *et al.* reported the synthesis of WO_3/CdS core/shell nanowire arrays by a rational, two-step chemical vapor deposition (CVD) process [65]. The WO_3 nanowires were coated by the narrow band gap semiconductor (CdS) shell. Compared to the band gap of WO_3 nanowires, of 2.7 eV, the band gap of WO_3/CdS core/shell arrays was decreased to 2.32 eV, indicating the enhancement of the light absorption range of WO_3 to

11

the visible region. Furthermore, the WO_3/CdS core/shell nanowire heterostructures demonstrated efficient charge separation and high transfer efficiency of photogenerated electrons compared to WO_3 nanowire arrays. This is due to the presence of nano-size heterointerface between the WO_3 nanowire core and the CdS shell.

Xilian *et al.* investigated the modulation of the band gap of WO_3 thin films by doping with nitrogen [66]. They prepared N-doped WO_3 thin films using reactive DC-pulsed magnetron sputtering employing nitrous oxide (N_2O) gas as the nitrogen dopant source instead of nitrogen (N_2). There was a systematic decrease in the band gap values of WO_3 thin films with nitrogen incorporation. These values were 3.44, 3.40, 3.36, and 2.97 eV corresponding to the amount of N concentration of 0, 4.7, 6.1 and 12.5 (at. %), respectively. Such a decrease in the band gap was attributed to the higher negative potential of the valence band of the N 2p orbital.

Band-gap tuning of WO_3 quantum dots was successfully achieved by Hiroto *et al.* [67]. They used a template method with mesoporous silica as a facile synthetic technique for size-tuned WO_3 quantum dots. In their technique, a precursor solution [$WO_2 (O_2)$ H_2O] was introduced into mesoporous silica templates followed by particulation or chemical reactions for conversion to quantum dots. A blue shift in the band gap was realized with reduction of the particle size. This shift was varied from 2.93 eV at a particle size of 1.8 nm to 3.7 eV at a particle size of 0.7 nm. Such a blue shift in the band gap with the reduction of the particle size was attributed to the quantum confinement effect.

12

Mohammed *et al.* reported the deposition of WO_xN_x thin films by dual magnetron sputtering of tungsten with various nitrogen/oxygen ratios [68]. They controlled the optical band gap of WO_3 thin films by varying the partial pressure of nitrogen. They observed a reduction in the optical band gap values of WO_3 from 3.2 to 2.93 eV with the variation of the normalized partial pressure of nitrogen from 0.029 to 0.999, respectively. This reduction was interpreted based on the difference in ionicity between metal-O and metal-N bonds. The ionicity in single bonds is enhanced with the increase of the electronegativity difference between the two elements forming a single bond. Since the electronegativity of oxygen (3.5) is larger than that of nitrogen (3.0), the W-O bond implies a larger charge transfer than the W-N bond. Therefore, the red-shift of the band gap may be ascribed to the decrease in the ionicity and hence an increase of the polarizability in W-N bond with increasing nitrogen content.

A decrease in the band gap of WO_3 thin films with vanadium doping was reported by Karuppasamy *et al.* [69]. The band gap of vanadium-doped WO_3 thin films prepared using reactive DC magnetron sputtering was found to decrease with the vanadium content. It was inferred that vanadium creates impurity levels below the conduction band of WO_3, making the band gap decrease. Thereafter, the authors tested the photocatalytic activity of the tuned band gap films and observed a maximum photocatalytic activity for the lower band gap sample containing 11 wt% vanadium.

Band gap narrowing of WO_3 thin films was also demonstrated by Lethy *et al.* [70]. They reduced the band gap of WO_3 thin films prepared by pulsed laser deposition (PLD) through nitrogen incorporation. Their results revealed that a systematic decrease in the

band gap of the films was observed with the increase in the nitrogen content. The explanation of the reduction in the band gap due to the nitrogen content was similar to that previously mentioned in ref 58.

Yanping *et al.* investigated the effect of carbon doping on the photo-electrochemical performance of WO_3 thin films [71]. In their study, undoped and C-doped WO_3 thin films were deposited using spray pyrolysis (SP). The results showed that the absorption of the C-doped WO_3 thin films was red-shifted compared to the undoped WO_3 thin film. The band gap narrowing was ascribed to the doping of C into the WO_3 lattice. The photo-electrochemical analysis showed that C-doped WO_3 thin films produced approximately 50% more enhanced photocurrent densities from visible light compared to the undoped films, indicating that C doping improved the photoactivity of WO_3 thin films.

A facile deposition-annealing method was employed for synthesizing tuned-band gap WO_3 thin films by Song *et al.* [72]. The band gap tuning was achieved through doping of WO_3 with Fe_2O_3. In their report, a series of Fe_2O_3 modified WO_3 thin films were synthesized through variation of the Fe_2O_3 concentration. The band gap of WO_3 thin film was about 2.7 eV, while the Fe_2O_3 modified WO_3 thin films were found to have band gaps of 2.64, 2.60, and 2.55 eV corresponding to iron concentrations of 10, 20, and 40 mmol/L, respectively. The tuned band gap Fe_2O_3 modified WO_3 thin films exhibited higher photocurrent response compared to the pure WO_3 thin films, due to the enhanced visible light absorption.

1.5.2 *Molybdenum oxide (MoO₃)*

MoO$_3$, as *n*-type semiconductor with wide indirect band gap ranging from 2.8 to 3.2 eV, possesses three different crystalline structures: a stable orthorhombic phase (α-MoO$_3$), a metastable monoclinic phase (β-MoO$_3$), and an open hexagonal structure [73,74]. MoO$_3$ thin films have attracted great interest due to its interesting structural, chemical, electrical, and optical properties [75]. Several applications have been reported for MoO$_3$, including electrodes for rechargeable batteries and electrochromic devices [75], solar cells [76,77], gas sensing [78,79], optoelectronic devices [49,80,81], display [82] and photocatalytic applications [83]. Owing to its large band gap, MoO$_3$ is capable of absorbing only the short-wavelength portion of the solar spectrum, which limits its application. Therefore, the success in narrowing its band gap would cover a wider portion of the visible spectrum, and thus, further photocatalytic, optoelectronic, and photovoltaic applications may be developed.

Many methods were utilized to tune the band gap of MoO$_3$ to meet the requirements for specific applications. In the following, I summarize some of these methods:

SP was used to prepare undoped and lithium 1–5 wt%) doped MoO$_3$ thin films by Kovendhan *et al.* [84]. X-ray diffraction analysis showed that the stable α-MoO$_3$ phase was obtained for the undoped MoO$_3$, while Li-doped MoO$_3$ thin films contained mixed phases of hexagonal and stable α-MoO$_3$. The conductivity of the Li-doped MoO$_3$ thin films showed a gradual decrease with the increase of Li concentration. This decrease was attributed to scattering of charge carriers at grain boundaries induced by the hexagonal

phase. The direct band gap was reduced from 3.72 eV for MoO_3 thin films to 3.42 eV for Li-doped MoO_3 thin films and the indirect band gap was reduced from 2.38 eV for MoO_3 thin films to 1.84 eV for Li-doped MoO_3 thin films. The authors believed that such a reduction in the band gap was due to the presence of mixed phases present in the doped films.

Mahajan *et al.* modulated the band gap of MoO_3 thin films by titanium doping using SP [85]. The band gap of the doped films was found to increase from 3.04 to 3.25 eV with titanium doping. The increase in the band gap was attributed to the increase in carrier density leading to the increase in the Fermi level in the conduction band towards higher energy, which is known as the Burstein-Moss effect.

Lee *et al.* succeeded in the fabrication of MoO_3 thin films using CVD and post-annealing [86]. The band gap of MoO_3 thin films was altered via heating the substrate and annealing in an oxygen atmosphere. The transmittance reached 80% with low reflectivity and the refractive index was around 1.55 with a flat dispersion curve across the visible. The band gap was 3.00 eV for the as-deposited films, 3.14 eV for the films heated at 500 ^{o}C, and 3.50 eV for the films annealed at 500 ^{o}C in an oxygen atmosphere. They attributed the increase in the band gap of MoO_3 thin film to the increase of the film's oxidation state and improved crystallinity with annealing.

Deposition of niobium-doped MoO_3 films via SP was reported by Mahajan *et al.* [75]. The structural analysis displayed the formation of polycrystalline stable α-phase for the undoped MoO_3 thin film; however, the Nb-doped films were amorphous. The band gap of the MoO_3 thin film was tuned by variation of the Nb concentration and was found to

16

increase from 3.04 eV to 3.25 eV with the increase of Nb doping. Furthermore, electrochemical measurements showed that the color efficiency and electrochemical stability of MoO_3 thin film increased with increasing the Nb concentration.

Vasilopoulou *et al.* exploited CVD to prepare hydrogenated and oxygen-deficient molybdenum oxide thin films [80]. The measured band gap values were found to be 3.00, 2.60, and 2.00 eV corresponding to MoO_3, H_yMoO_{3-x}, and MoO_{3-x} thin films, respectively. The reduction of the band gap of the H_yMoO_{3-x}, and MoO_{3-x} thin films was ascribed to the presence of occupied gap states within their forbidden gap. The beneficial role of the substoichiometric Mo oxides (H_yMoO_{3-x}, and MoO_{3-x} thin films) in organic optoelectronic devices was tested through designing an organic photovoltaic cell in which the open circuit voltage, the fill factor, and the cell power conversion efficiency were significantly enhanced for substoichiometric Mo oxides compared to the stoichiometric MoO_3.

Thermal evaporation was utilized to deposit ZnSe-doped MoO_3 by Tomás *et al.* [87]. X-ray diffraction confirmed the formation of amorphous undoped and ZnSe-doped MoO_3 films. The indirect band gap was varied with the irradiation time from 3.07 eV to 3.14 eV for the undoped films, from 3.19 eV to 3.39 eV for the 5% ZnSe doped-films, and from 2.97 eV to 3.28 eV for the 10% ZnSe-doped films. The increase of the band gap values of the ZnSe-doped MoO_3 thin films was related to crystallinity improvement.

Bouzidi *et al.* reported the effect of substrate temperature on the structural and optical properties of MoO_3 thin films prepared by SP [88]. The substrate temperature was in the range 200 to 300 °C. The structural analysis demonstrated that the films deposited at 200

^{o}C were monoclinic, while a polycrystalline orthorhombic phase was obtained in the temperature range 250 to 300 ^{o}C. The grain size of the films was found to increase with increasing the substrate temperature. Low transmission was observed in the films prepared at 200 ^{o}C, while those prepared at 250 ^{o}C showed a maximum transmission of 71%. Further increase in the substrate temperature to 300 ^{o}C led to a decrease in the transmission. The direct band gap of MoO_3 thin films was estimated and found to vary from 3.14 to 3.34 eV. For the films prepared at 200 ^{o}C, the band gap was 3.30 eV and increased slightly to 3.34 eV at 250 ^{o}C and then decreased to 3.14 eV at 300 ^{o}C. The authors attributed the increase of the band gap at 250 ^{o}C to the partial filling of the oxygen vacancies, and the decrease at higher temperatures was attributed to the oxygen vacancies that capture electrons and act as donor centers in the forbidden gap below the conduction band.

Electron beam evaporation was utilized to prepare MoO_3 thin films by Sivakumar *et al.* [89]. In their work, the optical properties of the films were modified by varying the substrate temperatures like room temperature (RT), 30 ^{o}C, 100 ^{o}C and 200 ^{o}C. At RT, the films had a transmittance in the range of about 91-95%. However, with increasing the substrate temperature, the transmittance was shifted towards longer wavelengths. The band gap of MoO_3 thin films was red-shifted with the increase of the substrate temperature and was found to lie between 2.8 and 2.3 eV. Such a reduction in the band gap was ascribed to the oxygen vacancies.

Sivakumar *et al.*[90] investigated the effect of MeV nitrogen-ion irradiation on electron-beam evaporated MoO_3 thin films grown at RT. The films were irradiated using

2-MeV nitrogen ions. The crystalline structure of the pristine and irradiated MoO_3 thin films was a polycrystalline orthorhombic α-phase, which implied that there was no structural change in the MoO_3 thin films due to nitrogen-ion irradiation. The band gap of pristine MoO_3 film was evaluated to be 2.92 eV. However, for the MoO_3 films irradiated with nitrogen, the band gap values were reduced from 2.90 – 2.78 eV, respectively. The reduction of the band gap with the increase of the nitrogen ion fluencies was attributed to the effect of the band tailing due to the defects created during irradiation.

Santos *et al.* [91] employed impregnation–decomposition cycles (ICD) to synthesize MoO_3 nanoparticles. The crystalline structure of the prepared nanoparticles was orthorhombic α-MoO_3 phase. The average sizes of the prepared nanoparticles were 3.2, 3.6 and 4.2 nm corresponding to 3, 5 and 7 ICD, respectively. The optical band gap of the synthesized MoO_3 nanoparticles was found to be red-shifted from 3.35 to 3.29 eV with the increase in the average sizes from 3.2 to 4.2 nm. This red-shift in the band gap was attributed to the quantum confinement effect.

1.5.3 *Cadmium telluride (CdTe)*

It is well-known that wide band gap semiconductors ($E_g > 2.5$ eV) are restricted to only the absorption of short wavelength (blue/ ultraviolet) radiation in the EM spectrum, and therefore are unable to utilize the visible part. A possible solution to this problem is to combine them with narrow band gap semiconductors [32,92,93]. Recently, great attention has been devoted to employ narrow-band-gap II–VI binary semiconductors to tune the optical properties of the wide band gap semiconductors [92-97]. Among these,

CdTe is a direct narrow band gap semiconductor (1.5 eV) with a zinc blend crystal structure [29, 98]. Because of its optimum band gap for solar energy absorption, it is a promising candidate for photovoltaic applications [99].

There exist few reports in the literature on the utilization of CdTe for tuning the optical properties of wide band gap semiconductors. Here, I represent some of these reports.

Zhao-Qing *et al.* employed electrochemical deposition to grow ZnO/CdTe core/shell nanotube arrays [100]. Remarkably, the synthesized nanotube arrays exhibited enhanced photocurrent density for water splitting, compared with the ZnO nanorod arrays. This enhancement in the photoresponse was attributed to the reduction of the band gap of ZnO nanorod arrays after being loaded by CdTe nanorods.

Xuebo *et al.* succeeded in synthesizing Cu_3Se_2-CdTe nanoclusters by means of a microwave-enhanced route and chemical process [101]. In their study, they found that pure Cu_3Se_2 nanoplates demonstrated much intense absorption in the visible portion of the spectrum and weak absorption in the ultraviolet region. However, Cu_3Se_2-CdTe nanoclusters showed high absorption in both the visible and ultraviolet regions. The enhancement of absorption in the ultraviolet originates from the effect of CdTe quantum dots. These changes in the optical properties of Cu_3Se_2 nanoplates after mixing with CdTe quantum dots had strongly reflected on their photoresponse. A superioer increase in the photocurrent density generated by Cu_3Se_2-CdTe nanoclusters was recorded compared to that of Cu_3Se_2 nanoplates and CdTe quantum dots. Furthermore, the response time of

Cu$_3$Se$_2$-CdTe nanoclusters for reaching saturation photocurrent was shorter than that of Cu$_3$Se$_2$ nanoplates and CdTe quantum dots.

CdTe-decorated TiO$_2$ nanotube array photoelectrodes were prepared using successive ionic layer adsorption and reaction technique by Qingyao *et al.* [102]. Optical analysis demonstrated significant red shift in the absorption edges of TiO$_2$ nanotubes from the ultraviolet light below 387 nm (3.2 eV) towards the visible region after the deposition of CdTe quantum dots. As a reflection of their tuned band gap, CdTe-dcorated TiO$_2$ nanotubes showed rapid separation and transformation of electron/hole pairs as well as photoelectrochemical performance.

The photcatalytic activity of CdTe/TiO$_2$ nanotube arrays composites fabricated by pulse electrodeposition was reported by Hui *et al.* [103]. In their report, it was emphasized that CdTe nanoparticles electrodeposited on the TiO$_2$ nanotubes improved its photocatalytic property. This improvement was attributed to the extension of the optical absorption in the CdTe/TiO$_2$ nanotube arrays from the ultraviolet to the visible light region.

Band gap engineering of zinc selenide (ZnSe) thin films was achieved by alloying it with CdTe as reported by Al-Kuhaili *et al.* [29]. In their report, thermal evaporation was utilized to prepare ZnSe/CdTe thin films. The films demonstrated considerable red shift in the optical absorption edge with the CdTe concentration increase. The band gap of the ZnSe thin films was gradually decreased from 2.8 eV of pure ZnSe to 1.75 eV at 33 wt% CdTe concentration. The new optical features had reflected on the photoresponse of the prepared films, where the photocurrent was increased with the CdTe concentration.

21

Andrew *et al.* studied the influence of strain on the properties of different shell materials (ZnS, ZnSe, ZnTe, CdS or CdSe) grown by epitaxial deposition on a small nanocrystalline core CdTe [104]. The optical properties of the core/shell nanocrystals were tuned by increasing the epitaxial shell growth as evidenced by the shift of the optical absorption edge and fluorescence emission to lower energies.   The authors emphasized that such red shift was due to the transformation of core/shell hetrostructures from type-I alignment to type-II alignment, in which the conduction band energy of the core rises up due to the lattice strain effect by the shell while the conduction band energy of the shell decreases due to the quantum confinement reduction.

1.5.4 Scope of the work

The scope of this work is:

I.   To fabricate WO_3 thin films alloyed with CdTe using thermal evaporation

II.   To engineer band gap of WO_3 thin films by mixing it with specific concentrations of CdTe.

III.   To fabricate MoO_3 thin films alloyed with CdTe using thermal evaporation.

IV.   To engineer band gap of MoO_3 thin films by mixing it with specific mass concentrations of CdTe.

V.   To study the effect of the addition of specific mass concentrations of CdTe on the band gap of the alloyed films.

VI.   To investigate the crystalline structure of the deposited films using X-ray diffraction.

VII.   To examine the surface morphology of the films using atomic force microscopy.

VIII.   To study the optical properties of the deposited films using spectrophotometry.

IX.   To investigate the chemical composition of the films using X-ray photoelectron spectroscopy.

X.   To investigate the suitability of the alloyed films for photovoltaic applications by measuring the photo-to-current conversion in a photoelectrochemical cell.

CHAPTER 2

THEORETICAL BACKGROUND

This chapter provides the theoretical background for this study. Specifically, it will discuss doping and alloying of semiconductors as well as the derivation of Tauc's equation used for the determination of the band gap in semiconductors.

2.1 Doping of semiconductors

Semiconductors can be divided into two types, intrinsic and extrinsic. The basic properties of each type can be highlighted as follows:

2.1.1 Intrinsic semiconductors

The intrinsic semiconductors are materials without impurity atoms and only the conduction band and valence band are involved. Figure 2.1 shows the energy-band diagram of an intrinsic semiconductor, where E_c, E_v and E_g are the conduction band energy, the valence band energy, and the band gap, respectively, In an intrinsic semiconductor such as silicon, some electrons are thermally excited from the valence band to the conduction band at room temperature, and can produce a current. The excited electron leaves behind an electron vacancy or "hole" in the valence band.
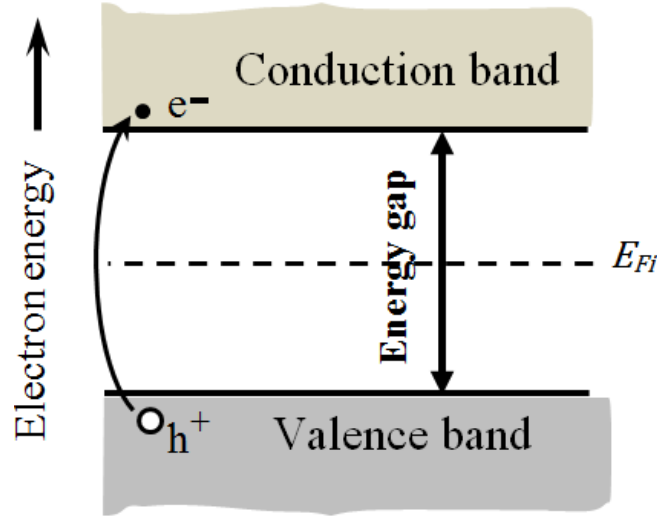
Fig. 2.1 Energy-hand diagram of an intrinsic semiconductor.

The general formulas for the concentration of electrons n_0 and holes p_0 at thermal equilibrium are given by

$$n_0 = N_c \, exp\left[-\frac{E_c - E_F}{k_B T}\right] \tag{2.1}$$

and

$$p_0 = N_v \, exp\left[-\frac{E_F - E_v}{k_B T}\right] \tag{2.2}$$

where $N_c = 2\left[-\dfrac{2\pi m_n^* k_B T}{h^2}\right]^{\frac{3}{2}}$ and $N_v = 2\left[-\dfrac{2\pi m_p^* k_B T}{h^2}\right]^{\frac{3}{2}}$

N_c and N_v are the effective density of states functions in the conduction and valence bands, respectively, m_n^* and m_p^* are the effective masses (the mass of the electron inside the crystal) of electrons and holes, respectively, E_c and E_v are the conduction and valence band energies, respectively, E_F is the Fermi energy (the energy below which all quantum

25

states are filled with electrons and above which all quantum states are empty at $T = 0$ K), k_B = is the Boltzmann constant, T is the absolute temperature and h is the Planck's constant.

For an intrinsic semiconductor, the electron concentration in the conduction band is equal to the hole concentration in the valence band. If we denote n_i and p_i as the intrinsic electron concentration and intrinsic hole concentration, respectively, we can write

$$n_i = p_i \tag{2.3}$$

Therefore, one may use the parameter n_i to refer to either the intrinsic electron or hole concentration. Also, the Fermi energy is called the intrinsic Fermi energy, $E_{Fi} \approx E_F$ [105].

Thus, by applying expressions (2.1) and (2.2) to an intrinsic semiconductor, we obtain

$$n_0 = n_i = N_c \, exp \left[- \frac{E_c - E_{Fi}}{k_\text{B} T} \right] \tag{2.4}$$

$$p_0 = p_{0i} = n_i = N_v \, exp \left[- \frac{E_{Fi} - E_v}{k_\text{B} T} \right] \tag{2.5}$$

Since $n_i = p_i$, we can set (2.4) and (2.5) equal to each other,

$$N_c \, exp \left[- \frac{E_c - E_{Fi}}{k_\text{B} T} \right] = N_v \, exp \left[- \frac{E_{Fi} - E_v}{k_\text{B} T} \right] \tag{2.6}$$

and solving for E_{Fi}, we have

$$E_{Fi} = \frac{1}{2}(E_c + E_v) + \frac{1}{2}k_B T ln\left[-\frac{N_v}{N_c}\right] \tag{2.7}$$

Since, $N_c = 2\left[-\frac{2\pi m_n^* k_B T}{h^2}\right]^{\frac{3}{2}}$, and $N_v = 2\left[-\frac{2\pi m_p^* k_B T}{h^2}\right]^{\frac{3}{2}}$

We can write expression (2.7) as

$$E_{Fi} = \frac{1}{2}(E_c + E_v) + \frac{3}{4}k_B T ln\left[\frac{m_p^*}{m_n^*}\right] \tag{2.8}$$

However,

$$\frac{1}{2}(E_c + E_v) = E_{midgap} \tag{2.9}$$

Hence, equation (2.8) may be written as

$$E_{Fi} = E_{midgap} + \frac{3}{4}k_B T ln\left[\frac{m_p^*}{m_n^*}\right] \tag{2.10}$$

Thus, at $m_p^* = m_n^*$

$$E_{Fi} = E_{midgap} \tag{2.11}$$

2.1.2 *Extrinsic (doped) semiconductors*

Incorporation of impurity atoms to an intrinsic semiconductor can modify its properties, including the band gap. The doped semiconductors are called extrinsic semiconductors and the impurities are called dopants. A donor atom has an extra valence

electron loosely bound to it. When providing a small amount of thermal energy, the donor electron can be elevated into the conduction band of the semiconductor, leaving the donor atom positively charged. As a result, the electron concentration n_0 of the semiconductor increases, and it is called *n*-type. Conversely, an acceptor impurity atom captures an electron, hence creates a mobile hole in the valence band of the semiconductor and becomes negatively charged itself. Therefore, the hole concentration p_0 of the semiconductor increases, and it is called *p*-type [105]. Figures 2.2a and 2.2b show the energy band diagram of these two types of extrinsic semiconductors, where E_d and E_a are the donor and acceptor energy levels, respectively. The expressions for the concentration of n_0 at thermal equilibrium can be derived by addition and subtraction of the intrinsic Fermi energy E_{Fi} in the exponent of the expression (2.1) as follows,

$$n_0 = N_c \, exp \left[\frac{-E_c - E_{Fi} + E_F - E_{Fi}}{k_B T} \right] \tag{2.12}$$

or,

$$n_0 = N_c \, exp \left[\frac{-E_c - E_{Fi}}{k_B T} \right] \, exp \left[\frac{E_F - E_{Fi}}{k_B T} \right] \tag{2.13}$$

Thus,

$$n_0 = n_i \, exp \left[\frac{E_F - E_{Fi}}{k_B T} \right] \tag{2.14}$$

Similarly, by addition and subtraction the intrinsic Fermi energy in the exponent of the expression (2.2), we get

$$p_0 = n_i \ exp\left[\frac{E_F - E_{Fi}}{k_B T}\right] \tag{2.15}$$

As can be seen from (2.14) and (2.15), if $E_F > E_{Fi}$, then $n_0 > n_i$ and $p_0 < n_i$, thus,

$n_0 > p_0$ (*n*-type semiconductor). However, if $E_F < E_{Fi}$, then $p_0 > n_i$ and $n_0 < n_i$, thus,

$p_0 > n_0$ (*p*-type semiconductor) [23,105].

If we take the product of the expressions (2.1) and (2.2) for n_0 and p_0, we obtain

$$n_0 \, p_0 = N_c N_v \ exp\left[-\frac{E_c - E_F}{k_B T}\right] \ exp\left[-\frac{E_F - E_v}{k_B T}\right] \tag{2.16}$$

or,

$$n_0 \, p_0 = N_c N_v \ exp\left[\frac{-E_g}{k_B T}\right] \tag{2.17}$$
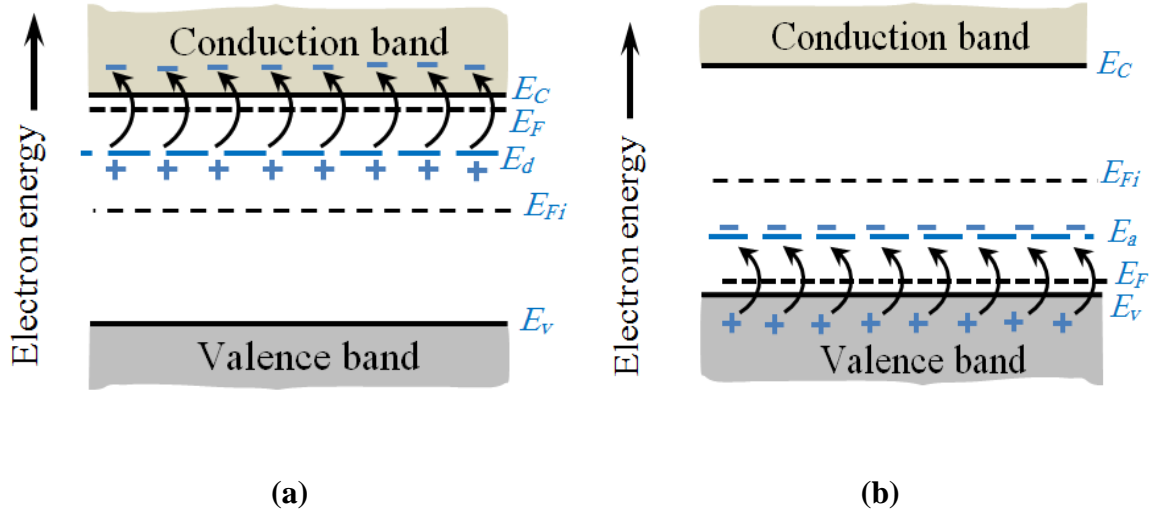
Fig. 2.2 Energy-band diagram at $T = 0$ K of (a) n-type and (b) p-type semiconductors.

2.2 Alloying of semiconductors

When two semiconductors A and B are mixed, the semiconductor alloy $A_{1-x}B_x$ is formed, where x is the concentration of component B in the alloy. The lattice constant of the obtained alloy a_{alloy} is given by Vegard's law [106]:

$$a_{alloy} = xa_B + (1 - x)a_A \qquad (2.18)$$

where a_A and a_B are the lattice constants of the semiconductors A and B, respectively. If the probability that the atom or molecule neighboring to a given atom or molecule is $(1 - x)$ for A atom\molecule and x for B atom\molecule, the alloy is termed a random

alloy. Such an alloy is desirable for electronic and optoelectronic applications. If A and B atoms\molecules have an ordered periodic structure, the alloy is called an ordered alloy. However, if the A atoms are accumulated at one region in the crystal and the B atoms are accumulated at another region, a phase separated alloy is formed. Figure 2.3 shows a schematic diagram of these three kinds of alloys [26,31]. The periodicity of the crystalline potential of a random alloy is broken because of the randomness of the atoms on the lattice sites. As a result, it is difficult to calculate the band structure of the alloy and hence the band gap. Therefore, a simple approximation called virtual crystal approximation (VCA) is used to provide a simple approach to determine the band gap of the alloy. It replaces the crystalline potential of the alloy with a weighted average of the potentials (U) of the individual constituents. This potential is given by

$$U_{alloy} = xU_B + (1-x)U_A \qquad (2.19)$$

Consequently, the VCA approximates the alloy as a single uniform semiconductor for which the band gap can be estimated. Hence, the band gap, $E_{g,alloy}$ may be linearly interpolated between the endpoint values of the parents, which is given by

$$E_{g,alloy}(x) = xE_{g,B} + (1-x)E_{g,A} \qquad (2.20)$$

where, $E_{g,A}$ and $E_{g,B}$ are the band gaps of the two parent semiconductors A and B. However, in most alloys, the obtained band gap deviates slightly from the above equation due to the increase of the disorder with alloying. Therefore, it was found that the band gap of the alloy can be described reasonably by a modification of the expression (2.20) as follows:

31

$$E_{g,alloy}(x) = xE_{g,B} + (1-x)E_{g,A} - bx(1-x) \qquad (2.21)$$

where   b is a bowing factor which describes the nonlinearity in the trend of the band gap

of the alloy [106,107].
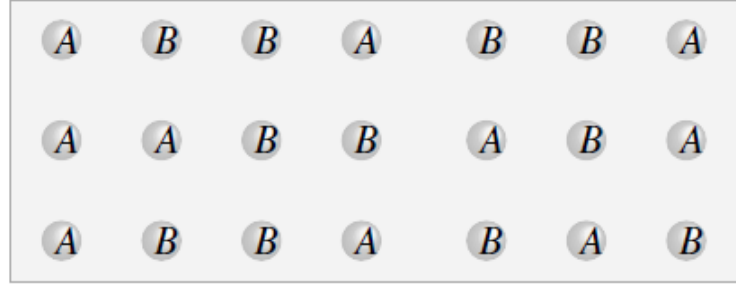
(a)
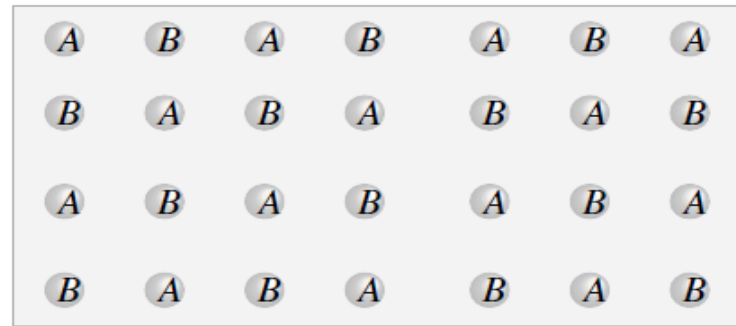
(b)
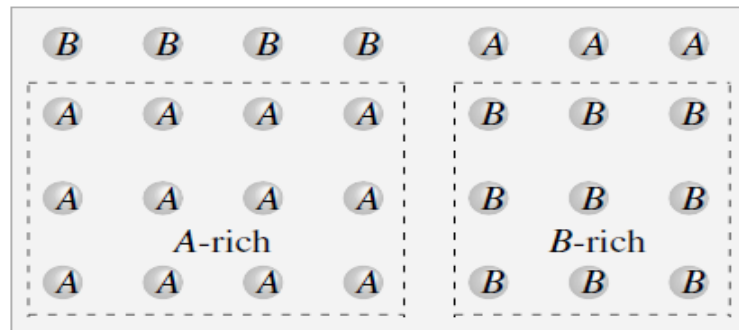
(c)

Fig. 2.3 A schematic diagram of (a) random and (b) ordered, and (c) clustered alloys.

2.3 Derivation of Tauc's equation

In this section, I will derive the Tauc's equation that will be used in Chapters 4 and 5 for the determination of the band gap of the fabricated films.

Starting with the general expression for the absorption coefficient α

$$\alpha = \frac{\hbar\omega . W_{i \to f}}{I} \tag{2.22}$$

where $\hbar = \frac{h}{2\pi}$ (h is the Planck's constant), $\omega = 2\pi\nu$ (ν is the frequency of the incident photon), $W_{i \to f}$ is the transition probability/ unit volume /unit time, and I is the total light incident intensity (energy/unit time/unit area). For solving equation (2.22), we have to look for expressions for $W_{i \to f}$ and I.

Firstly, we start with I. From the point of view of classical electrodynamics, we can define I as

$$I = \frac{c}{8\pi} Re \left\{ \vec{n} . (\vec{E} \times \vec{B}) \right\} \tag{2.23}$$

where, c is the speed of light, $\vec{E}$ and $\vec{B}$ are the electric and magnetic fields, respectively, and $\vec{n}$ is a unit normal at the surface. However, in vacuum, the electric and the magnetic field amplitudes are equal, hence, $\vec{E} = \vec{B}$. This gives,

$$I = \frac{c}{8\pi} \left| \vec{E} \right|^2 \tag{2.24}$$

Now we define $\vec{E}$,

$$\vec{E} = -\frac{1}{c}\frac{\partial \vec{A}}{\partial t} \qquad (2.25)$$

and for a vector potential of the radiation field $\vec{A}$:

$$\vec{A} = \vec{A}_0 \, \exp[i(\vec{k}.\vec{r} - \omega t)] + c.c. \qquad (2.26)$$

which represents a transverse plane wave, where $\vec{A}_0$ is the amplitude of the wave, $\vec{k}$ is the angular wave number, $\vec{r}$ represents the vector displacement of a general point from the origin and ω is the wave's angular frequency.

Hence,

$$\vec{E} = -\frac{1}{c}\frac{\partial \vec{A}}{\partial t} = \frac{i\omega}{c}\vec{A} \qquad (2.27)$$

Plugging 2.27 into 2.24 leads to:

$$I = \frac{\omega^2}{8\pi c}\left|\vec{A}\right|^2 \qquad (2.28)$$

Secondly, $W_{i \to f}$:

The Fermi's Golden Rule defines the transition rate $(W_{i \to f})$ in a quantum system from $|i\rangle$ (initial eigenstate) of a given Hameltonian H_0 to $|f\rangle$ (final eigenstate) due to a perturbing Hameltonian H and is given by

$$W_{i \to f} = \frac{2\pi}{\hbar} |\langle f|H'|i\rangle|^2 \rho(\hbar\omega) \tag{2.29}$$

where $\langle f|H'|i\rangle$ is the matrix element of the perturbation H' between the final and initial states and $\rho(\hbar\omega)$ is the density of the final states. Considering the interaction with the radiation field, the perturbing Hameltonian H' is:

$$H' = \frac{e}{m_0} \vec{A} \cdot \vec{p} \tag{2.30}$$

Where e is the free electron charge, m_0 is the free electron mass and $\vec{p}$ is defined as

$\vec{p} = i\,\hbar\vec{\nabla}$

Plugging 2.30 into 2.29 gives

$$W_{i \to f} = \frac{2\pi}{\hbar} \left(\frac{e}{m_0}\right)^2 \left|\vec{A}\right|^2 |\langle f|\vec{p}\,|i\rangle|^2 \rho(\hbar\omega) \tag{2.31}$$

where

$$|\langle f|\vec{p}\,|i\rangle|^2 = \frac{m_0^2 E_g}{2m^*}$$

represents the average of the squared matrix elements for transitions between Bloch states in the valence and conduction bands, where Therefore, equation (2.31) is rewritten as

$$W_{i \to f} = \frac{2\pi}{\hbar} \left(\frac{e}{m_0}\right)^2 \left|\vec{A}\right|^2 (\frac{m_0^2}{2m^*})\, \rho(\hbar\omega) \tag{2.32}$$

To find an expression for $\rho(\hbar\omega)$, one should calculate the joint density of states, which is defined as the number of electronic states in the conduction and valence bands that are separated by a given photon energy $\hbar\omega$. Assume that the semiconductor system has simple parabolic bands. In momentum space, the energy-k expressions $E_v(k)$ and $E_c(k)$ for the valence and the conduction bands of the semiconductor, respectively, can be written as

$$E_v(k) = -\frac{E_g}{2} - \frac{\hbar^2 k^2}{2m_p^*} \tag{2.33}$$

$$E_c(k) = \frac{E_g}{2} + \frac{\hbar^2 k^2}{2m_n^*} \tag{2.34}$$

and the conservation of energy states that, $E_v + \hbar\omega = E_c$

So,

$$E_c - E_v - \hbar\omega = 0 \tag{2.35}$$

Plugging (2.33) and (2.34) into (2.35) leads to,

$$E_g + \frac{\hbar^2 k^2}{2}\left[\frac{1}{m_n^*} + \frac{1}{m_p^*}\right] - \hbar\omega = 0 \tag{2.36}$$

If we let m^* be the reduced mass, where,

$$\frac{1}{m^*} = \frac{1}{m_n^*} + \frac{1}{m_p^*}$$

Then, (2.36) takes the form

36

$$E_g + \frac{\hbar^2 k^2}{2m^*} = \hbar\omega \qquad (2.37)$$

For an ideal parabolic band direct gap semiconductor, the electronic transitions only occur at $\hbar\omega \geq E_g$. The density of states in momentum space is given by

$$\rho(k) = \frac{k^2}{2\pi^2} \qquad (2.38)$$

and the density of states per unit energy range is given by

$$\rho(E) = \frac{2\rho(k)}{\frac{dE}{dk}} \qquad (2.39)$$

Since $E \equiv \hbar\omega$, we can have from equation (2.37):

$$\frac{dE}{dk} = \frac{\hbar^2 k}{m^*} \qquad (2.40)$$

Substituting (2.40) into (2.39) gives

$$\rho(E) = \frac{2\rho(k)}{\hbar^2 k / m^*} \qquad (2.41)$$

Plugging (2.38) into (2.41) leads to,

$$\rho(E) = 2\left(\frac{k^2}{2\pi^2}\right)\left(\frac{m^*}{\hbar^2 k}\right) = \frac{km^*}{\pi^2 \hbar^2} \qquad (2.42)$$

where k is given from (2.37) by

$$k = \left[\frac{2m^*}{\hbar^2}\left(\hbar\omega - E_g\right)\right]^{1/2} \tag{2.43}$$

So, (2.42) becomes

$$\rho(E) = \frac{m^*}{\pi^2\hbar^2}\left(\frac{2m^*}{\hbar^2}\right)^{1/2}\left(\hbar\omega - E_g\right)^{1/2} \tag{2.44}$$

Hence, the joint density of states is,

$$\rho(E) = \rho(\hbar\omega) = \frac{1}{2\pi^2}\left(\frac{2m^*}{\hbar^2}\right)^{3/2}\left(\hbar\omega - E_g\right)^{1/2} \tag{2.45}$$

Then, plugging (2.45) into (2.32) gives

$$W_{i\to f} = \frac{2\pi}{\hbar}\left(\frac{e}{m_0}\right)^2|\vec{A}|^2\left(\frac{m_0^2}{2m^*}\right)\frac{1}{2\pi^2}\left(\frac{2m^*}{\hbar^2}\right)^{3/2}\left(\hbar\omega - E_g\right)^{1/2} \tag{2.46}$$

Finally, we substitute (2.28) and (2.46) into (2.22)

$$\alpha = \frac{(\hbar\omega)\frac{2\pi}{\hbar}\left(\frac{e}{m_0}\right)^2|\vec{A}|^2\left(\frac{m_0^2}{2m^*}\right)\frac{1}{2\pi^2}\left(\frac{2m^*}{\hbar^2}\right)^{3/2}\left(\hbar\omega - E_g\right)^{1/2}}{\frac{\omega^2}{8\pi c}|\vec{A}|^2} \tag{2.47}$$

Simplifying

$$\alpha = \frac{8ce^2E_g}{\hbar}\left(\frac{2m^*}{\hbar^2}\right)^{1/2}\frac{\left(\hbar\omega - E_g\right)^{1/2}}{\hbar\omega} \tag{2.48}$$

Let

$$C = \frac{8ce^2 E_g}{\hbar} \left(\frac{2m^*}{\hbar^2}\right)^{\frac{1}{2}} \qquad (2.49)$$

Then,

$$\alpha = C \frac{\left(\hbar\omega - E_g\right)^{1/2}}{\hbar\omega} \qquad (2.50)$$

or

$$(\alpha\hbar\omega)^2 = C^2 \left(\hbar\omega - E_g\right) \qquad (2.51)$$

where C is just a scaling factor.

Therefore,

$$(\alpha\hbar\omega)^2 = \left(\hbar\omega - E_g\right) \qquad (2.52)$$

which is the Tauc's equation for direct band gap semiconductor [108,109]. A similar analysis for an indirect band gap semiconductor leads to

$$(\alpha\hbar\omega)^{1/2} = \left(\hbar\omega - E_g\right) \qquad (2.53)$$

CHAPTER 3

EXPERIMENTAL WORK and CHARACTERIZATION TECHNIQUES

The films were fabricated by thermal evaporation and characterized by various analytical techniques. This chapter sheds light on the main idea of thermal evaporation and discusses the experimental procedure and characterization techniques associated with this work.

3.1 Methodology: Thermal evaporation

Thermal evaporation is considered as one of the simplest techniques for the deposition of thin films. The main idea of thermal evaporation is to evaporate the material of interest inside a vacuum chamber. Figure 3.1 depicts the schematic of thermal evaporation. In this technique, a powder is supplied with adequate thermal energy to be transformed into the vapor phase. The powder is evaporated by heating it in a crucible (tungsten or molybdenum boat) of high melting point. Subsequently, the vapor condenses as a solid material on a substrate that is at a lower temperature than the heating source [110]. Thermal evaporation exhibits various desirable characteristics, such as minimum impurity contamination in the film, lower temperature required for materials sublimation under vacuum, and a variety of substrate selection including metals, alloys, ceramics and glass. Furthermore, other attractive features include the simplicity of the

technique, wide choice of coating materials, excellent coating adhesion, and the ability of

tuning the microstructure by controlling the coating parameters.
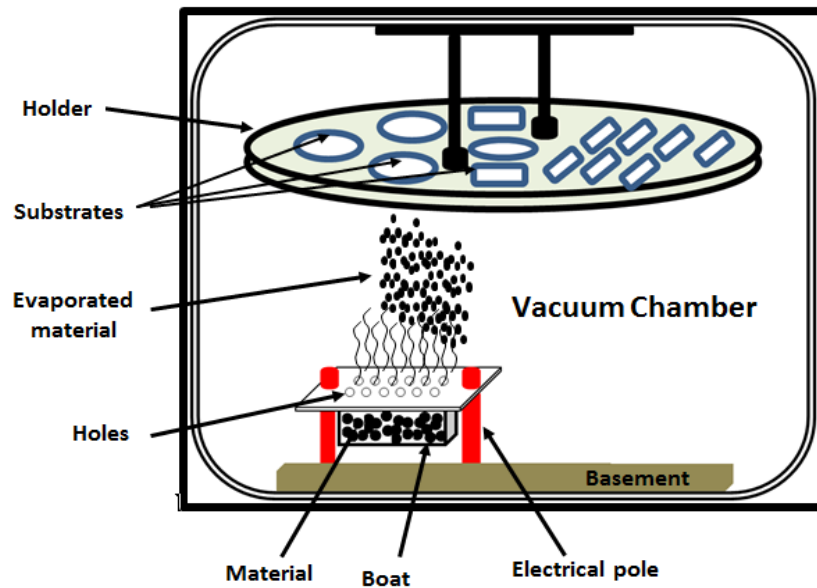
Fig. 3.1 A schematic of the thermal evaporation process.

3.2 X-ray diffraction (XRD)

XRD is an important experimental technique used for investigating the crystalline structure of solids, such as determination of crystalline size (grain size), and orientation of crystals. It is also commonly used for the identification of unknown materials and determination of the lattice constants of the crystal. The basic principle of XRD depends on the diffraction of x-rays by the atoms of the material being analyzed to give information about the structure of the material. X-rays can be scattered by electrons contained of atoms in the crystal lattice as shown in Fig. 3.2. If the scattered x-rays are in phase (coherent), they interfere in a constructive way producing diffracted beams in specific directions governed by Bragg's law:

$$2L \, sin\theta = \ j\lambda \tag{3.1}$$

where L is the spacing between diffracting planes (atomic planes), θ is Bragg angle, j is the order of diffracted beam, and λ is the wavelength of the x-ray beam. Therefore, Bragg's law plays an important role in indexing x-ray diffraction patterns and for determining the crystal structure of materials.
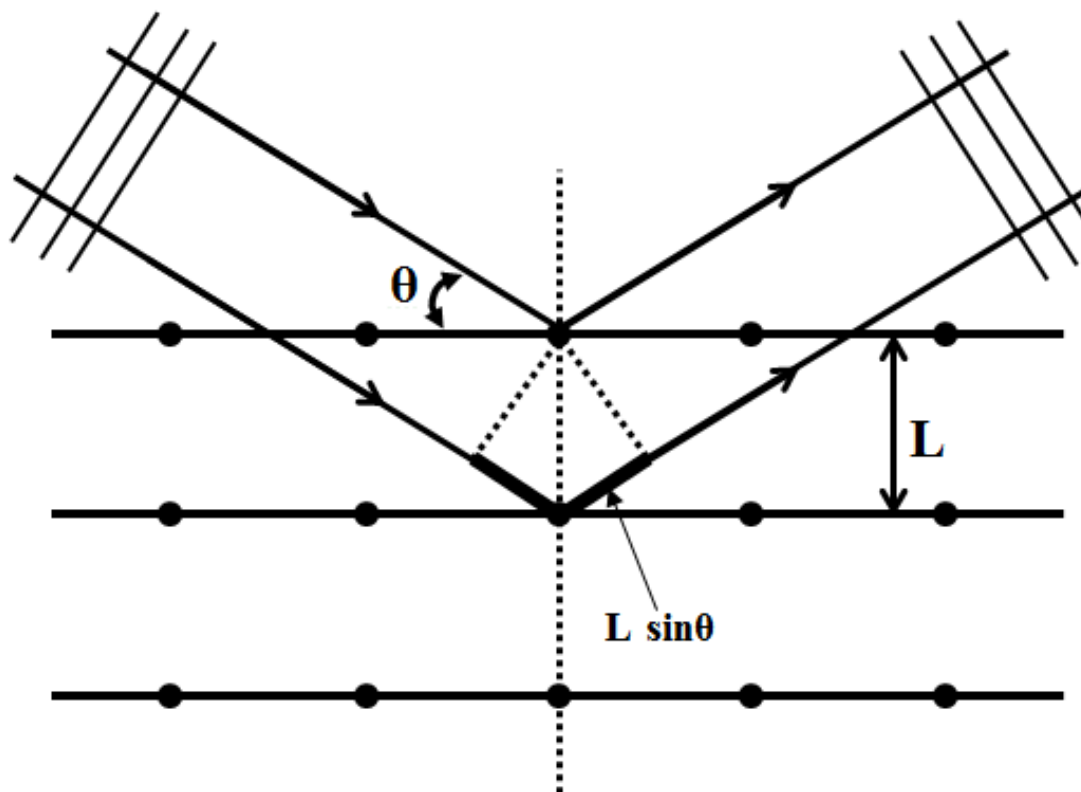
Fig. 3.2 A schematic of diffraction of x-rays by a crystal.

The three basic components of an XRD diffractometer are: x-ray source, specimen, and x-ray detector are shown in Fig. 3.3. In a typical XRD diffractometer, x-rays are generated by heating a metal filament cathode (with a current) to emit electrons that are accelerated toward the anode (target) by applying a high voltage. As the emitted electrons strike and eject an inner shell electron of the atom of the target, x-rays are produced. The beam of produced x-rays, in turn, is applied on the sample being analyzed to be diffracted. The diffraction pattern is like a fingerprint of the substance and consists of a series of peaks that corresponds to the x-ray diffracted from a specific set of planes in the material being analyzed. On modern devices, peak searches are performed on a computer.

The computer plots the peak intensity versus the diffraction angle 2θ, and therefore, one can compare standard patterns from the Joint Committee on Powder Diffraction Standards (JCPDS) database with the experimentally observed patterns, allowing rapid matching of patterns and material identification [111].
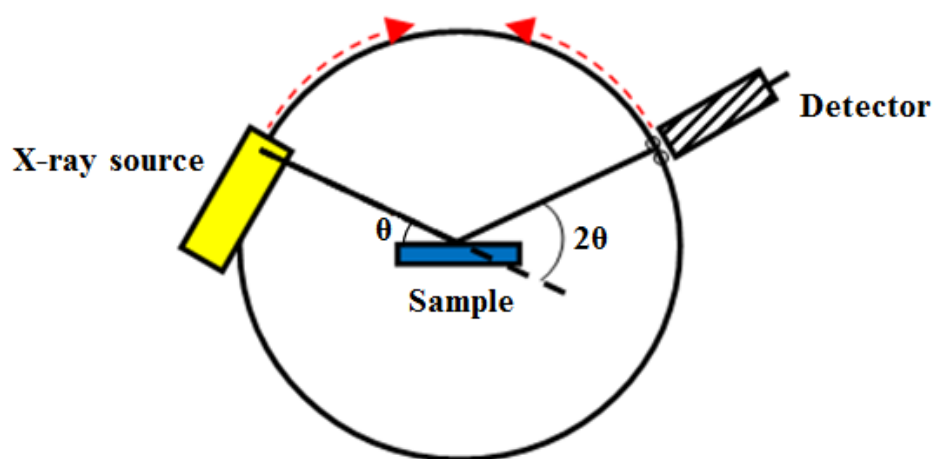
Fig. 3.3 A schematic of the basic components of the XRD diffractometer.

The XRD machine used in this work is a Rigaku Ultima IV diffractometer, with the following operation conditions:

- X-ray wavelength ($\lambda = 1.5406$ Å) that corresponds to C_uK_α.

- The current and voltage used were 30 mA and 40 kV, respectively.

- Scanning speed for data collection was 2^0 /min.

- The angle scanned (2θ) was in the range 20-80^0.

3.3 Atomic force microscopy (AFM)

Among scanning probe microscopies, AFM is a powerful technique for investigating the local surface structure of a sample with high resolution down to the nanometer scale. Figure 3.4 illustrates the main components of AFM. These include a sharp tip mounted on a cantilever, a laser beam and photo-detector. The working principle of AFM is that the sharp tip scans the surface of the sample at short distances in the range 0.2-10 nm. As the sharp tip gets sufficiently close to the surface of the sample, Van der Waals interaction occurs. The interaction force causes the cantilever to deflect and the cantilever in turn reflects the laser beam that strikes it at the back side. Then, the cantilever deflections are measured as the reflected laser beam falls on the photodetector leading to generation of a topographic image of the sample surface. The application of AFM determines its operation mode. Generally, there are three operation modes; contact mode, tapping mode and non-contact mode. In the contact mode, the sharp tip is kept in touch with the sample surface so the interaction force between them is repulsive. During the

45

scanning of the sample surface, the contact force deflects the cantilever due to the changes in the surface topography. The contact mode is often employed for imaging hard specimen and flat surfaces with high resolution and fast scanning. One of the drawbacks of this mode is that the cantilever tip may spoil the sample or vice versa due to the direct contact between them. In the noncontact mode, the tip doesn't contact the sample surface. However, the cantilever tip oscillates vertically at the resonant frequency of the cantilever, forming a weak attractive Van der Walls force that acts between the probe and the sample surface. This attractive force decreases and causes changes in the amplitude of the cantilever tip oscillation, which reflects the changes in the sample topographic image. This mode is advantageous for mapping the surface of soft samples because it doesn't cause damage to the sample. However, a feedback loop system is recommended for such a mode to keep the amplitude of the tip oscillation constant and an ultra-high vacuum environment is also recommended because adsorbed water layer on the sample surface can hinder the measurements. Finally, in the tapping mode, the cantilever tip is not kept in constant touch with the sample; rather, the cantilever oscillates and taps the sample surface. These oscillations are reduced due to the energy loss caused by the sample surface-tip interaction as the cantilever reaches and touches the sample surface. Then, the reduction of the amplitude of the oscillation can manifest the surface structures of the sample. Since the force is greatly reduced during scanning, this mode is preferable in scanning soft samples such as biological species. However, the scanning takes more time compared with the contact mode [112-114]. In this study, the surface morphology of the fabricated thin films was investigated by contact mode AFM (Veeco Innova diSPM). The

surface of the film was probed with a silicon tip of 10 nm radius oscillating at its resonant frequency of 300 kHz. The scan area was 2×2 μm^2, and the scan rate was 2 Hz.
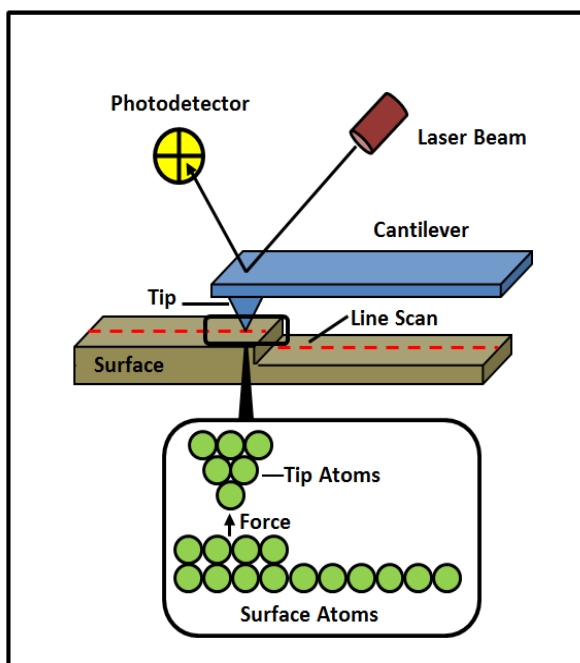
Fig. 3.4 A schematic of the basic principle of the AFM technique.

3.4 UV-visible spectroscopy

Ultra violet (UV)-visible spectrophotometry is used to measure the light transmitted, absorbed and reflected by semiconducting thin films. Since the solid films show low scattering of light, such a technique is efficiently used for evaluating the band gap values of these films from their transmittance or absorbance spectra. The main principle of the spectrophotometer is based on measuring the transmitted, absorbed or reflected light from the surface of the film as a function of wavelength. A UV-Visible spectrophotometer consists of a light source (a tungsten/halogen lamp for the visible spectrum or a deuterium lamp for the UV), a diffraction grating monochromator that splits and diffracts

light into several beams of different wavelengths, sample cell, reference cell, two rotating disks (each consists of transparent part, mirror part and black part), two mirrors and photodetectors. A general schematic diagram showing a double-beam UV-Visible spectrophotometer is represented by Fig. 3.5.
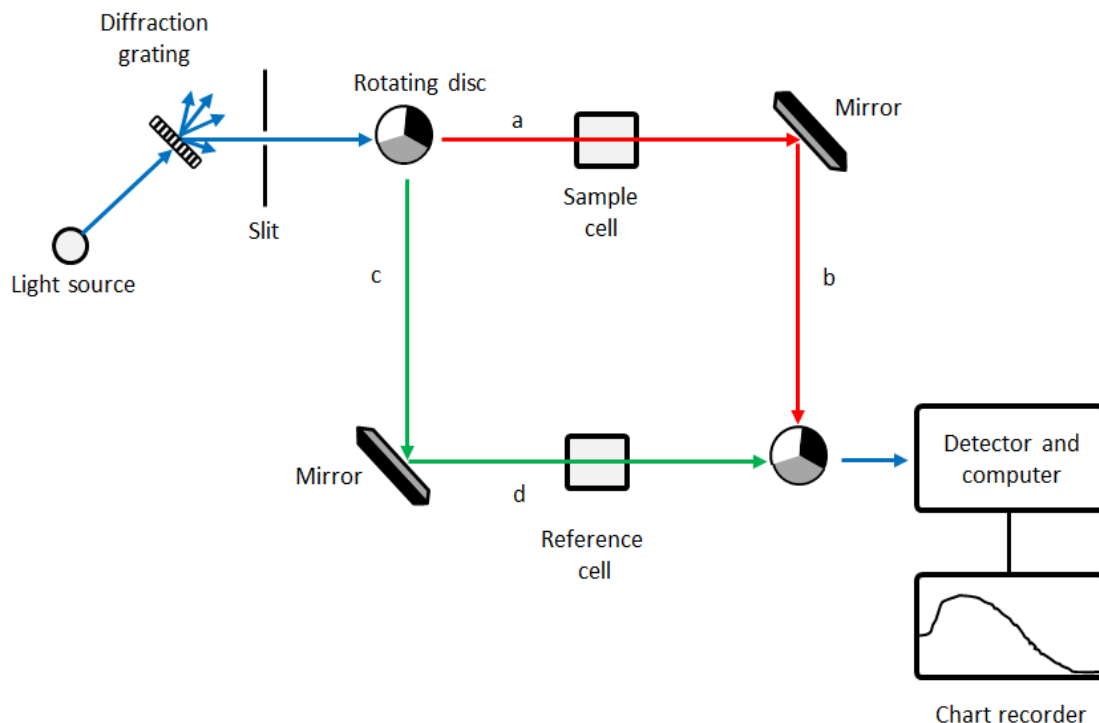
Fig. 3.5 A schematic diagram of a double beam spectrophotometer.

As the light from the lamp is passed through the diffraction grating and falls on the first rotating disk, the following three processes may happen:

1- If it falls on the transparent part, it will pass through the sample cell to be reflected onto the detector and computer (path a and path b).

2- If it falls on the mirror part of the first rotating disk, it will be reflected by the mirror (paths c and path d) and then pass through the reference cell to meet the transparent part. Then, it goes to the detector and computer.

3- If the light comes to the black part of the first rotating disk, it will be totally blocked and no longer passes through the spectrophotometer within short time. This helps computer to make allowance for current generated by the detector in the absence of the light. After rotating disc, the beam is allowed to pass through the two cells, reference cell and sample cell.

The reference cell is quartz cuvette which contains bare solvent in case of the solution sample or bare substrate in case of film sample. The detector converts the incident light into current signal that is then processed and converted into transmittance, absorbance or reflectance spectrum displayed on the computer. In the transmittance measurements, the spectrophotometer compares quantitatively both the amount of light passing through the sample and the reference [115,116]. These optical measurements enable one to calculate the absorption coefficient, band gap and the thickness of the fabricated thin films as will be discussed in details in chapters 4 and chapter 5. In this study, a Jasco V570 double-beam spectrophotometer was employed to execute the normal-incidence transmittance of the pure WO_3 and MoO_3 as well as the alloyed films over the wavelength range $300-800$ nm. However, the normal-incidence transmittance of the CdTe films was measured over the wavelength range $200-2000$ nm.

3.5 X-ray photoelectron spectroscopy (XPS)

XPS is considered as one of the most powerful analytical techniques that provide the following: identification of all elements, except H and He, present at concentrations greater than 0.1 atomic %, elemental surface composition, and information about the molecular environment such as oxidation state and covalently bonded atoms. The main components of XPS, as shown in Fig. 3.6, are an x-ray gun, transfer lenses, hemispherical electron energy analyzer (HSA) which disperses the emitted photoelectrons due to their speeds and a detector for recording their intensity.
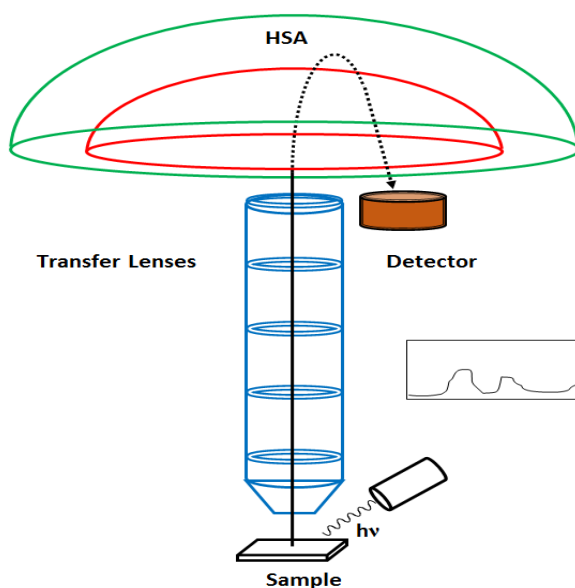
Fig. 3.6 A schematic of an XPS instrument.

In XPS, an incident beam of monochromatic x-rays irradiates the sample under study, resulting in photoelectron emission from the core level of atoms on the specimen's surface with a certain kinetic energy. The kinetic energy of the emitted photoelectrons is

linearly proportional to the energy of the incident x-rays. The binding energy of each core-level electron is a characteristic of the atom and the specific orbital to which it belongs. Thus, determination of the binding energy, E_i, of the emitted photoelectron is useful for identification of the atom involved. It is given by the Einstein equation [117,118]:

$$E_i \;=\; h\nu - E_k - \Phi \qquad\qquad\qquad (3.4)$$

where $h\nu$ is the energy of the incident X-ray, E_k is the kinetic energy of the emitted photoelectron and Φ is the work function of the spectrophotometer (energy needed to move an electron from the Fermi level of the solid into vacuum). The binding energies of the various elements have been measured and tabulated in reference tables. These tables are used as a reference when studying the surface atomic composition of any sample [119].

In this work, a Thermos Scientific Esca lab 250Xi spectrometer equipped with a monochromatic Al K_α (1486.6 eV) X-ray source was employed to perform the chemical analysis. To calibrate the spectrometer energy, Ag $3d_{5/2}$, Au $4f_{7/2}$ and Cu $2p_{3/2}$ were fixed at binding energies of 368.2, 83.9 and 932.6 eV, respectively [120]. The energy resolution of the instrument was 0.5 eV. The pressure inside the spectrometer during the XPS analysis was 7×10^{-10} mbar. The binding energies of the spectra were calibrated with adventitious C 1s peak positioned at 284.5 eV. Elemental depth profiles of the WO_3/CdTe and MoO_3/CdTe thin film samples were accomplished by a sequence of 60s Ar^+ ion etching followed by XPS analysis. Etching was achieved with a 3keV Ar^+ ion

beam with a medium ion current over a 1×1 mm^2 area of the sample surface. The incidence angle of the Ar$^+$ ion beam with respect to the surface of the sample was 30°. During depth profile process, the pressure inside XPS chamber was 5×10^{-8} mbar. Films were completely etched by applying fourteen etching cycles, except one film of lower thickness that was etched by only ten etching cycles. To eliminate charging of film surface during XPS analysis, all films were deposited on tantalum substrates.

3.6 Potentiostat/Galvanostat (PGSTAT) – Electrochemical cell setup

Figure 3.7shows a simplified energy diagram of a photoelectrochemical (PEC) cell based on a three-electrode potentiostat and an electrolyte. The three-electrode are a working electrode (WE), such as *n*-type semiconductor thin film deposited on a conducting substrate, a metal counter electrode (CE), and a reference electrode (RE). The main component of the PEC cell is the semiconductor, which absorbs light and converts it to electron–hole pairs. These electrons and holes are spatially separated from each other due to the presence of an electric field inside the semiconductor. The photogenerated electrons are swept toward the conducting substrate (back contact), and are transported to the metal counter-electrode via an external wire. At the counter electrode, the electrons reduce water to form hydrogen gas. The photogenerated holes are swept toward the semiconductor/electrolyte interface, where they oxidize water to form oxygen gas. The potentiostat is operated in two modes; potentiostatic mode and galvanostatic mode. In potentiostat mode, the PGSTAT controls the potential of the CE versus WE, so that the potential difference between the WE and the RE is well defined, which corresponds to

the value assigned by the user. In galvanostatic mode, the current flowing between the WE and the CE is controlled. The potential difference between the RE and WE and the current flowing between the CE and WE are continuously monitored. In this work, the photocurrent was measured in a standard three electrode configuration with $WO_3/CdTe$ thin films on indium-tin oxide as a WE, Ag/AgCl as RE, and a Pt foil as a CE, respectively. Photoelectrochemical measurements were conducted in 0.5M Na_2SO_4 (Sigma Aldrich) electrolyte. The samples were illuminated by an artificial sunlight simulator (300 mW/cm^2) using a Xenon lamp. The bias voltage was kept at 0.23 V for chronoamparometric study.

Kol;l;
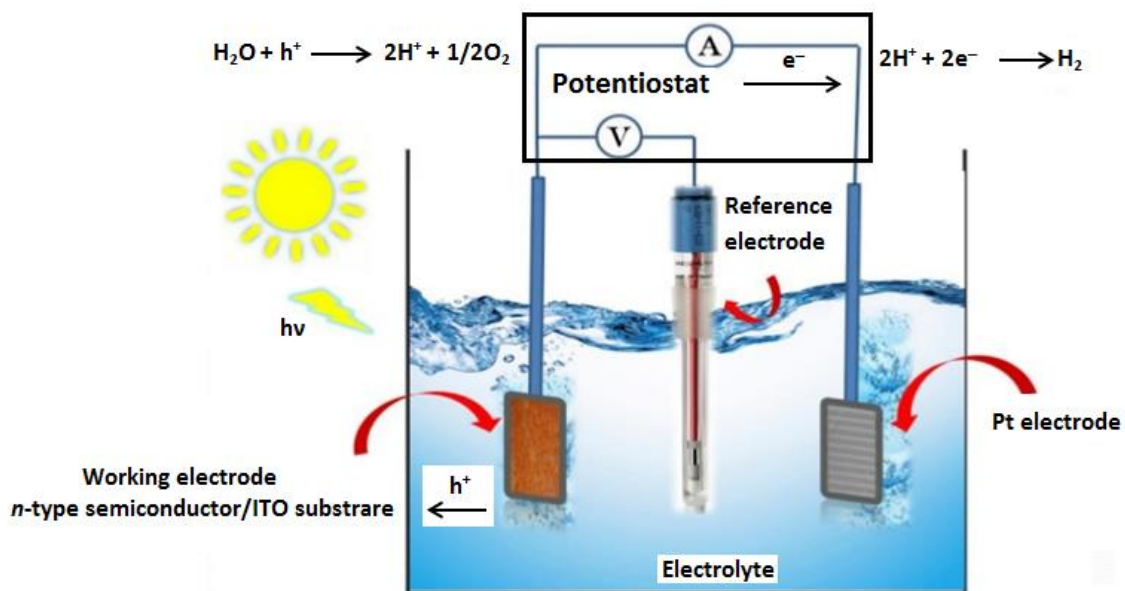
Fig. 3.7 A schematic of a three-electrode PGSTAT-photoelectrochemical cell setup.

3.7 Experimental Procedure

In my work, the starting materials were powders of WO_3, MoO_3 and CdTe, and the mass of the WO_3 or MoO_3 powder was 2g in all depositions. Various concentrations of CdTe specifically; 5%, 10%, 15%, 20% and 25% were added to WO_3 powder, however, 2%, 4%, 6%, 8% and 10% were added to MoO_3 powder. These concentrations were the ratio of the CdTe mass to the mass of the concerned metal oxide. I reduced the CdTe mass concentration added to MoO_3 to avoid the deterioration of the optical properties of the alloyed films at higher CdTe concentrations. A detailed discussion will be reported in Chapter 5. The films were fabricated in a Leybold L560 box coater. Compared to the other sophisticated deposition techniques, the novelty of this technique is that the band gap tuning of the oxides of interest just requires evaporation of a powder mixture of each oxide with small additives of CdTe.

In a typical deposition experiment, WO_3 powder (Alfa, 99.999% purity) was homogeneously mixed with specific concentrations of CdTe powder (Balzers, 99.999% purity). The mixture was then thermally evaporated in a molybdenum boat (heater) leading to the deposition of thin films on the substrate. Different substrates namely; fused silica, tantalum and indium tin oxide (ITO) were used. The variation of the substrates aims to make a comprehensive characterization of the structural, optical and elemental properties as well as testing the photocurrent response of alloyed films. The film thickness and the evaporation rate were monitored by a quartz crystal and a rate controller, respectively. The thickness of the films was fixed to be 300 nm. However, the real thickness of all films was estimated optically and verified by a stylus profilometer

and was found to be 270 ± 20 nm. The evaporation rate was 0.2 nm/s. Prior to evaporation, the thermal evaporation system was pumped down to a base pressure of 2×10^{-5} mbar and the raw material (the mixture of powders) was slowly out gassed. During deposition, the substrate holder was rotating to obtain uniform films and the substrate-sample distance was 40 cm. The band gap of WO_3 thin film was engineered by varying the concentration of CdTe in the mixture. A similar procedure was followed for engineering the band gap of MoO_3. The effect of CdTe concentration on the band gap of WO_3 and MoO_3 thin films deposited on unheated substrates was investigated. However, the effect of substrate heating on the band gap of the concerned metal oxides was excluded from this study because one deposition was conducted on CdTe and it was found that no film was deposited. This indicates that the band gap of the concerned metal oxides cannot be engineered on heated substrates since CdTe cannot stick to heated substrates.

CHAPTER 4

RESULTS and DISCUSSION

BAND GAP TUNING of WO$_3$ THIN FILMS THROUGH ALLOYING with CdTe

In this chapter, results of the band gap engineering of WO$_3$ thin films will be presented. The effect of CdTe concentration on the tuning of the band gap of the fabricated WO$_3$ thin films will be discussed as well as its effect on the morphological, optical properties and the chemical composition of the films. Further, the suitability of the fabricated WO$_3$/CdTe thin films for photovoltaic solar energy conversion will be also presented.

4.1 Structural analysis

XRD analysis revealed the amorphous and polycrystalline nature of the thermally-evaporated WO$_3$ and CdTe thin films, as seen in Figs. 4.1a and 4.1b, respectively. Peak assignments were based on the International Center for Diffraction Data (ICDD) files [121]. The amorphous nature of the WO$_3$ thin films indicates that the kinetic energy of the evaporated species was less than the height of crystallization barrier. However, the polycrystalline CdTe films indicate that the crystallization barrier was overcome in these films. The broad hump centered at $2\theta = 22^0$ in all films is attributed to the fused silica substrate. The films alloyed with 5%, 10% and 15% of CdTe still had an amorphous

nature, as presented in Figs. 4.2(a-c). However, a CdTe concentration of 20% resulted in the appearance of multiple peaks characteristic of CdTe centered at $2\theta = 23^{\circ}$, 39° and 46°, corresponding to the (111), (220) and (311) orientations of CdTe, respectively, as shown in Fig. 4.3a. The intensities of these peaks increased with further increase in the CdTe concentration up to 25%, as seen in Fig. 4.3b.
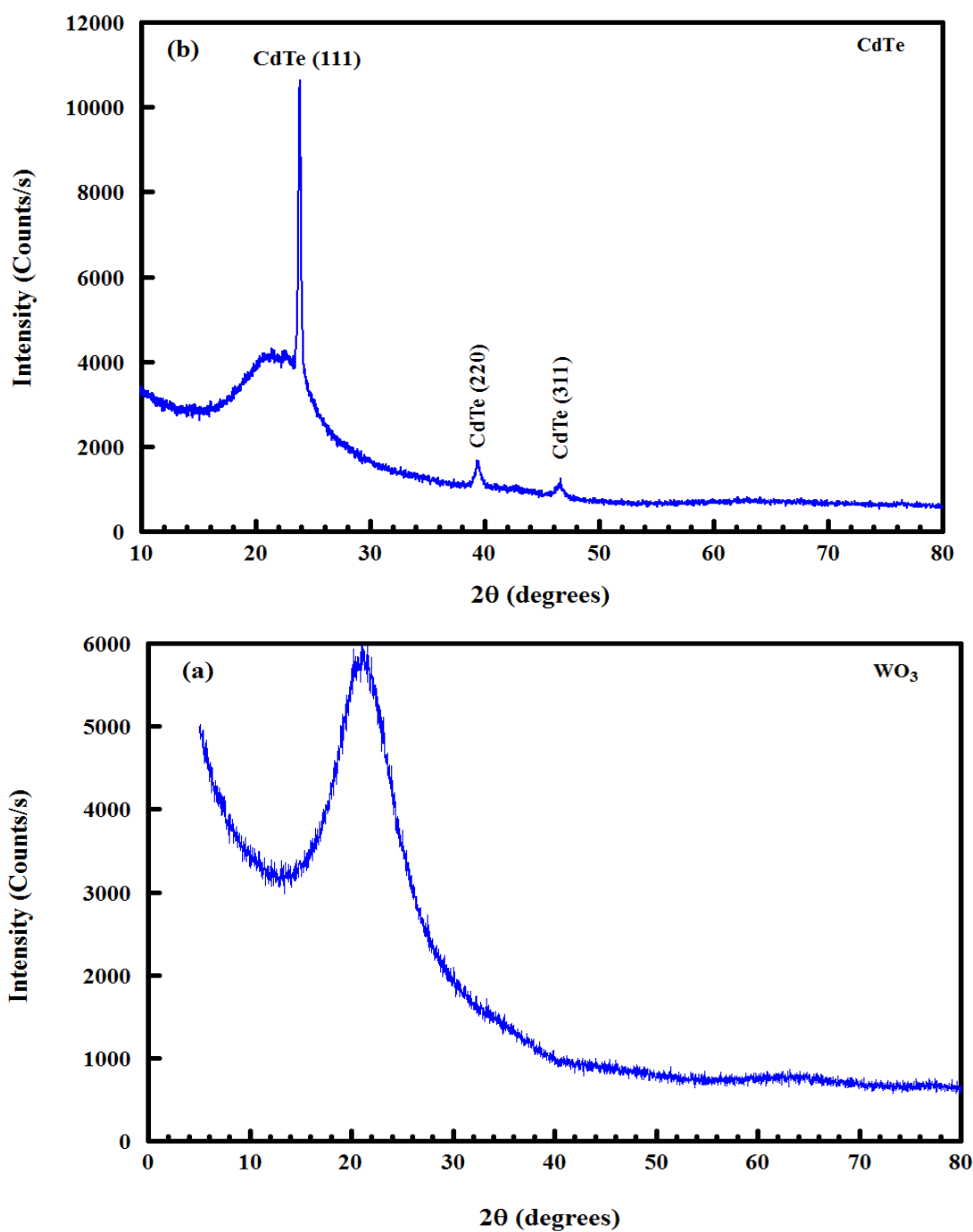
Fig. 4.1 XRD patterns of thermally-evaporated WO₃ (a), and CdTe (b) thin films
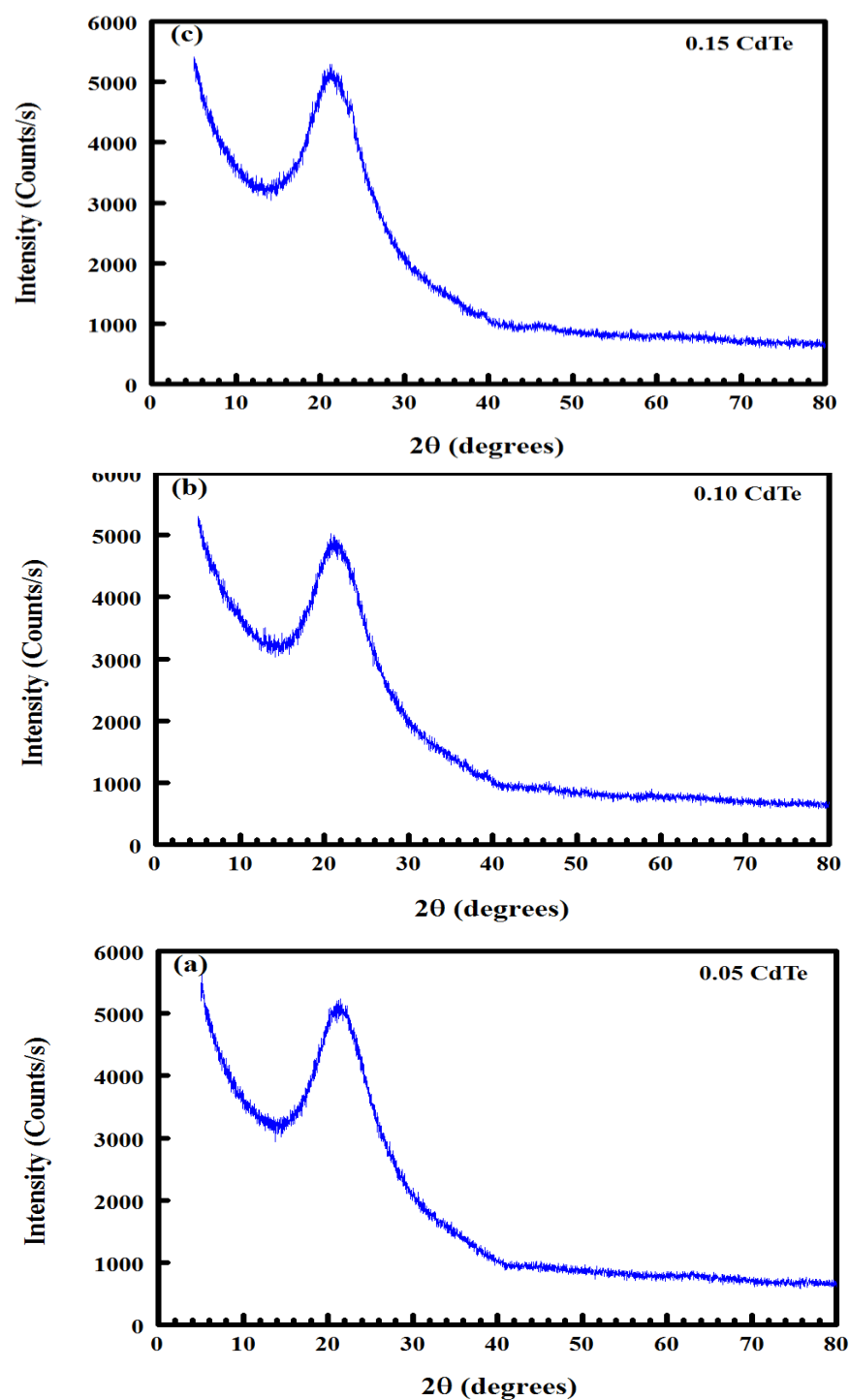
Fig. 4.2 XRD patterns of thermally-evaporated WO$_3$ thin films alloyed with CdTe mass concentrations of 5% (a), 10% (b) and 15% (c).
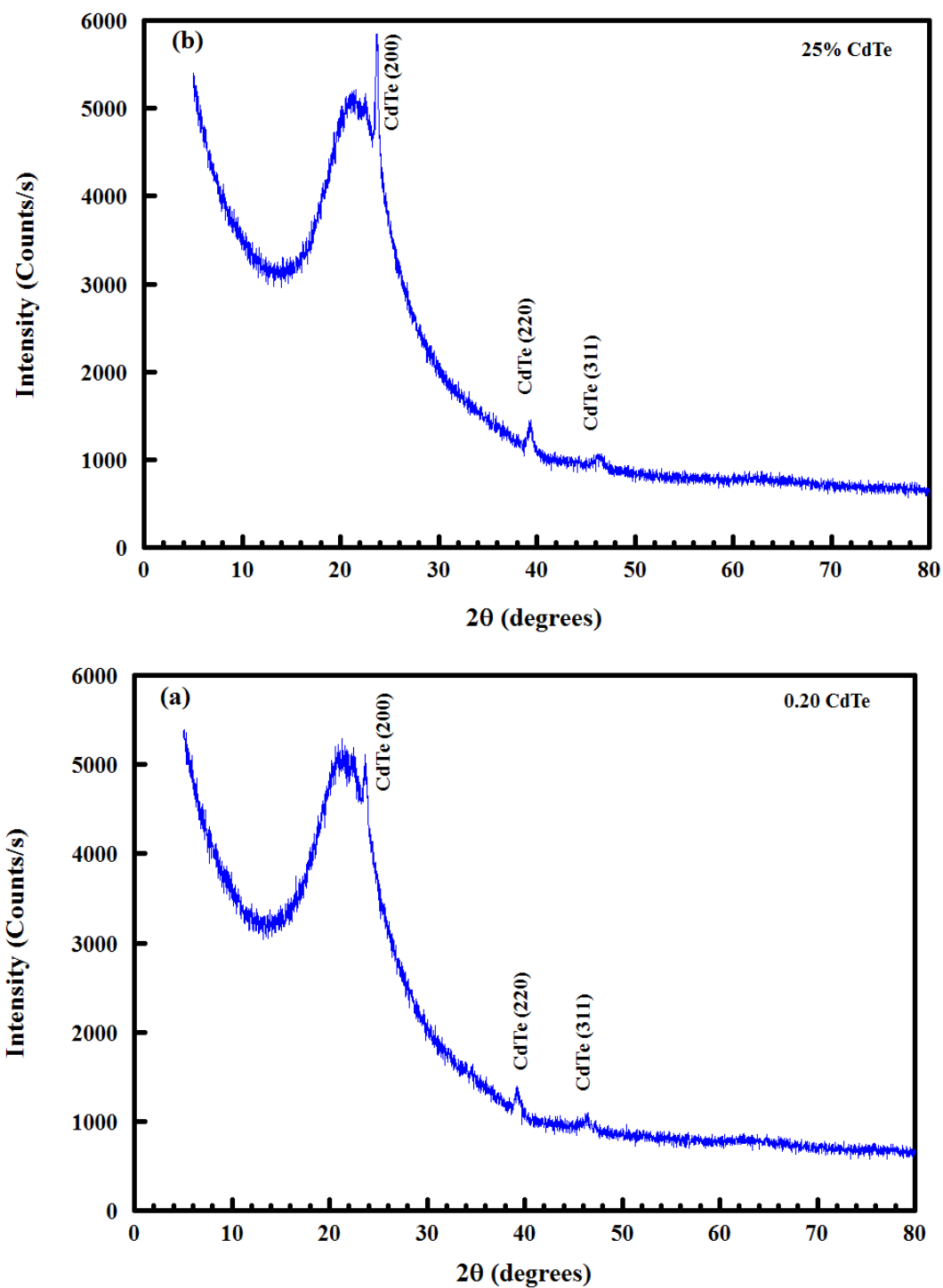
Fig. 4.3 XRD patterns of thermally-evaporated WO₃ thin films alloyed with CdTe mass concentrations of 20% (a) and 25% (b).

4.2 Morphological study

The morphological structure of the fabricated films was investigated using the AFM technique. The surface roughness of the investigated films was characterized by the root-mean-square (R_{rms}) roughness. Three dimensional AFM images of pure WO_3 and pure CdTe thin films are shown in Fig.4.4a and Fig. 4.4b, respectively. The surface morphology of pure WO_3 films displayed a columnar structure, while a granular structure was observed in the pure CdTe thin films. CdTe dopant concentrations of 5 and 10 % resulted in the formation of a dense columnar structure, as shown in Fig. 4.4c and Fig. 4.4d, respectively. However, Fig. 4.4e reveals that this columnar structure started to transform into a granular structure at a CdTe concentration of 15%. A dense granular structure was formed in the film containing 20% CdTe, as shown in Fig. 4.4f. Further increase in the CdTe dopant to 25% led to the formation of a columnar structure mixed with small grains as can be seen in Fig. 4.4g. The variation of R_{rms} with CdTe concentration is presented in Fig. 4.5. It can be noted that the roughness increased linearly as the CdTe dopant increased from 5 to 25%.
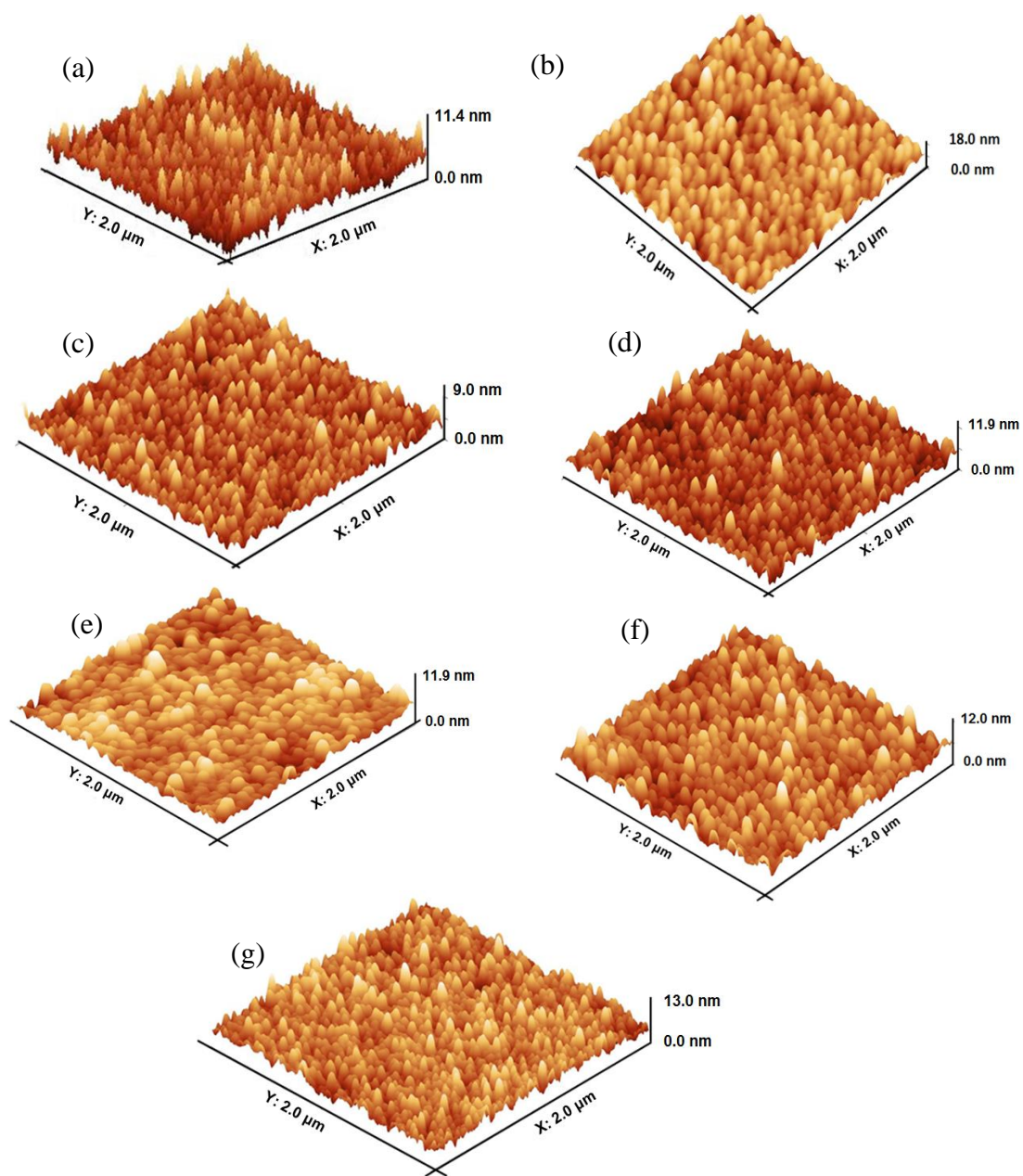
Fig. 4.4 Three dimensional AFM images of thermally evaporated WO₃ films (a), CdTe films (b) and WO₃ films alloyed with mass concentrations of 5% (c), 10% (d), 15% (e) 20%, (f) and 25% (g).
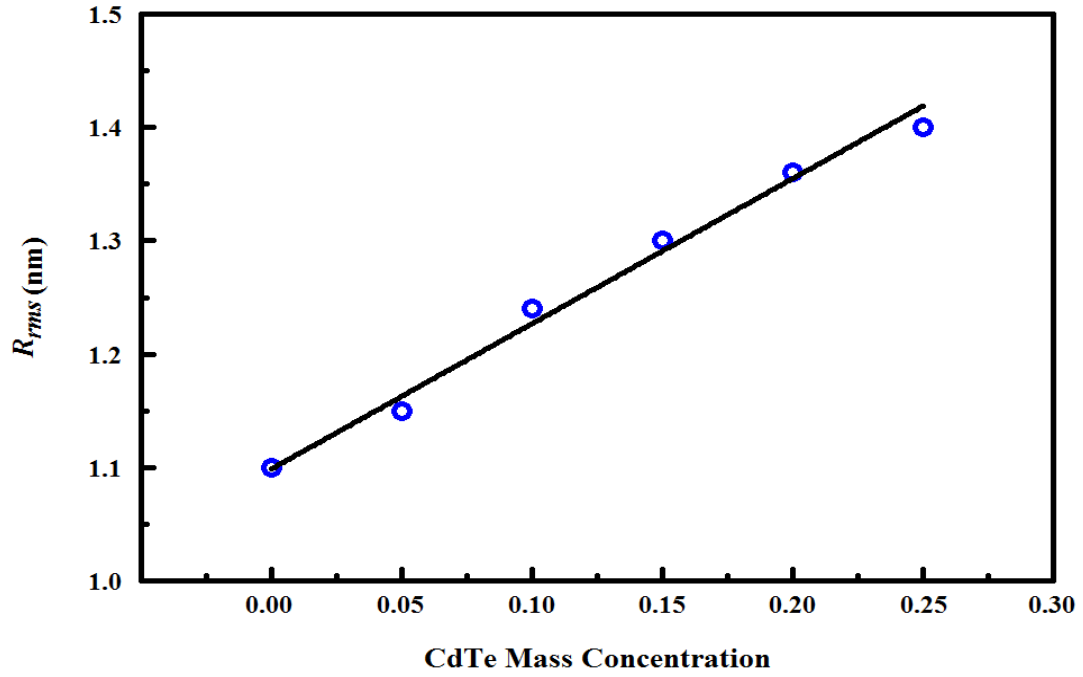
Fig. 4.5 Variation of R_{rms} with CdTe mass concentration.

4.3 Optical properties

4.3.1 Transmittance measurements

Figure 4.6a shows the transmittance spectrum of a pure WO_3 thin film. The film shows maximum transparency in the visible region down to a wavelength of 400 nm. A pronounced absorption edge can be observed below a wavelength of 400 nm. This absorption edge will be red-shifted due to alloying of WO_3 with different concentrations of CdTe, as will be seen in the following discussion. However, before proceeding in this discussion, it makes sense to determine the absorption edge of the CdTe film so that we make a reasonable comparison between the absorption edges of the films before and after

63

alloying. The transmittance of a pure CdTe thin film is shown in Fig.4.6b. The film is transparent in the infrared region of the EM spectrum, showing a sharp absorption edge below a wavelength of 850 nm.

The absorption edge of WO_3 thin films was red-shifted by alloying with CdTe, as shown in Fig. 4.7 Moreover, it can be noted that the optical transparency of the films decreased with the addition of CdTe. The lower optical transparency in the alloyed films may be accounted for by the increase in the optical absorption due to mixing with CdTe, which has a higher absorption coefficient.
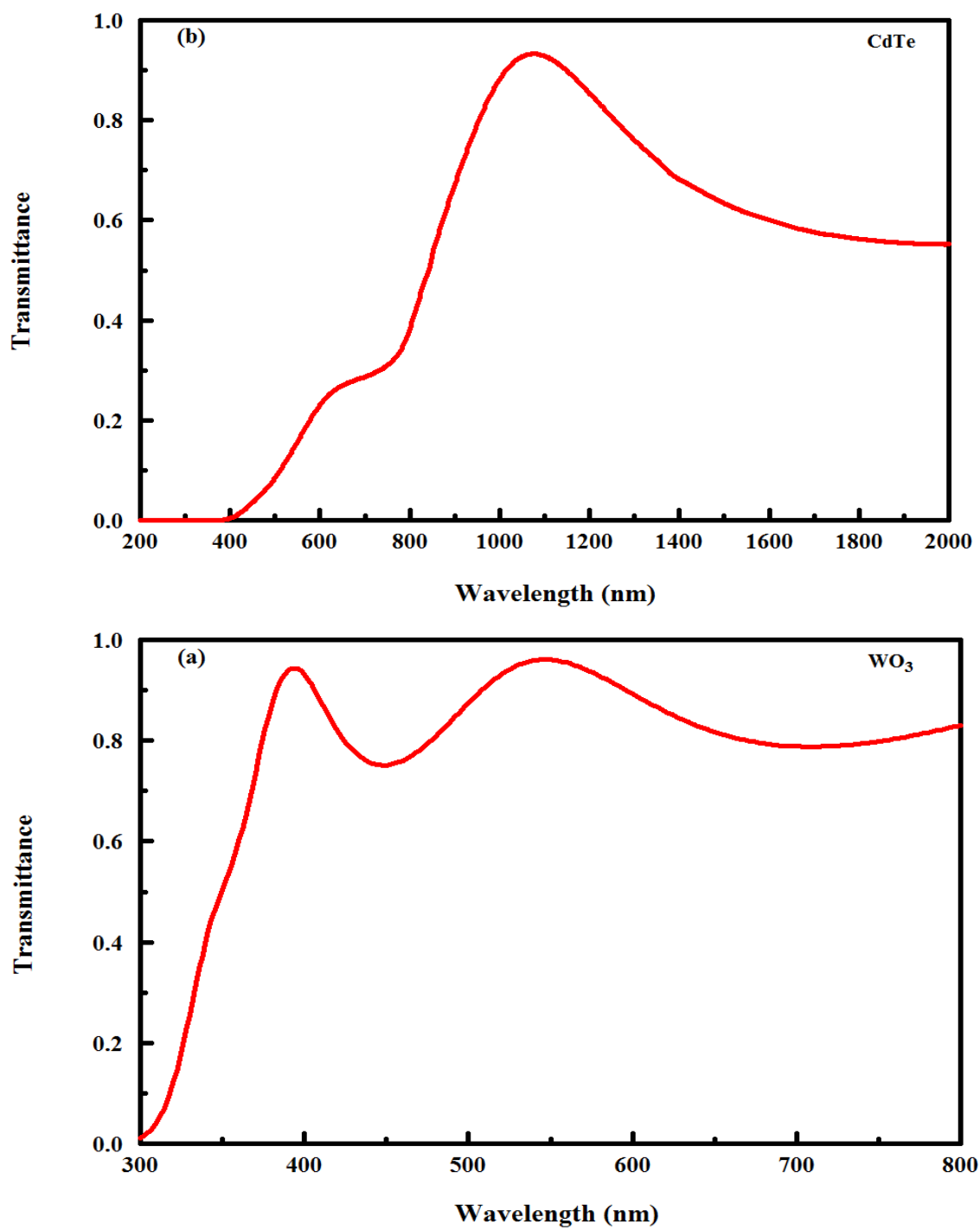
Fig. 4.6 Transmittance spectra of thermally-evaporated WO$_3$ (a), and CdTe (b) thin films.
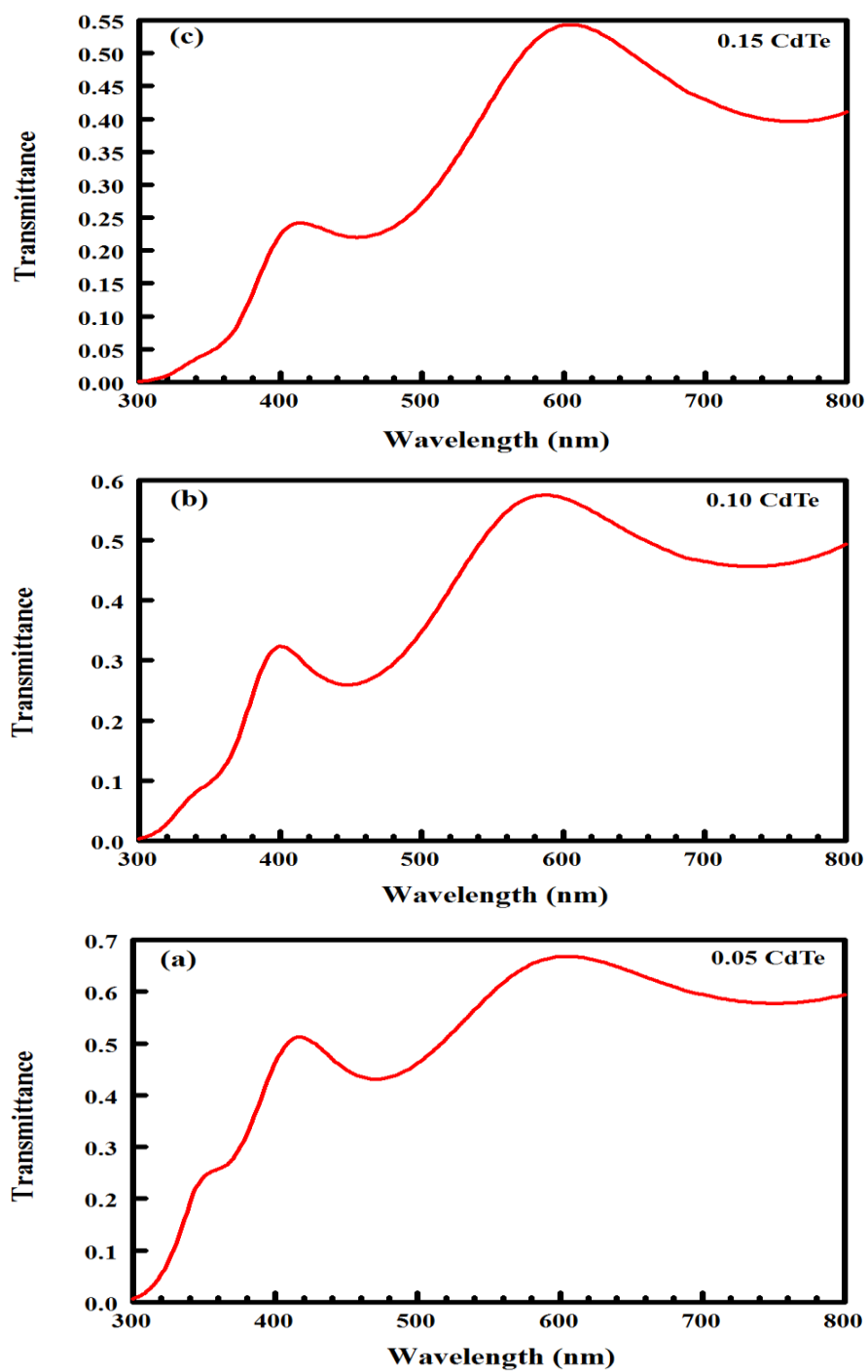
Fig. 4.7 Transmittance spectra of thermally-evaporated WO$_3$ thin films alloyed with CdTe mass concentrations of 5% (a), 10% (b), 15% (c), 20% (d) and 25% (e).
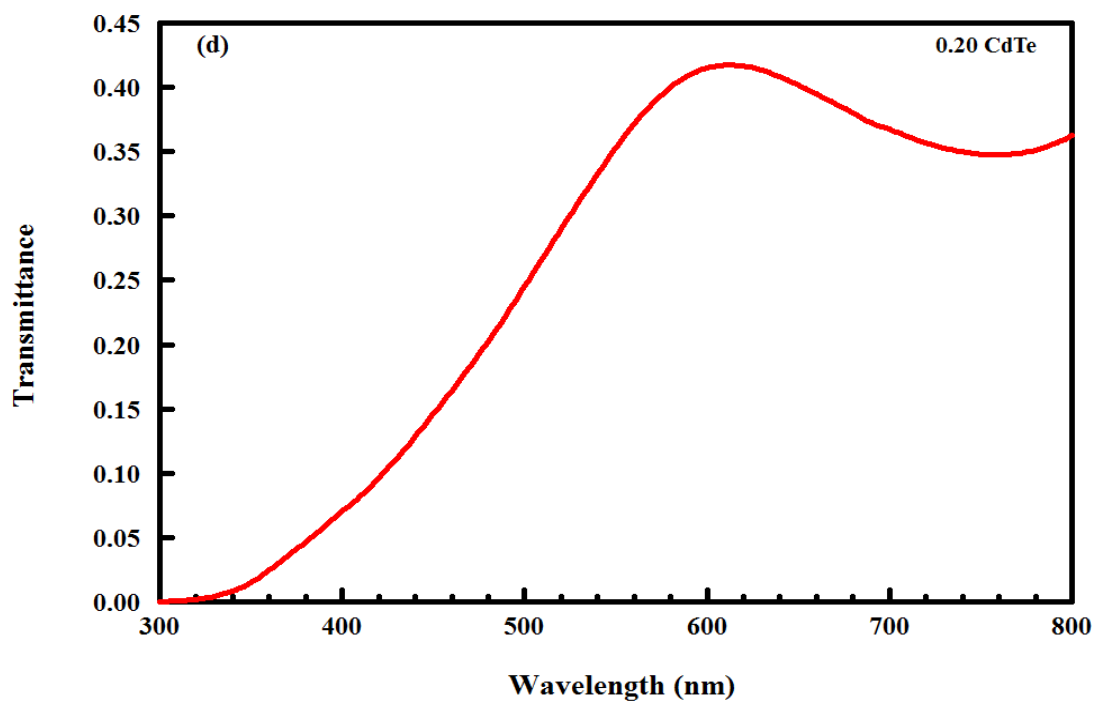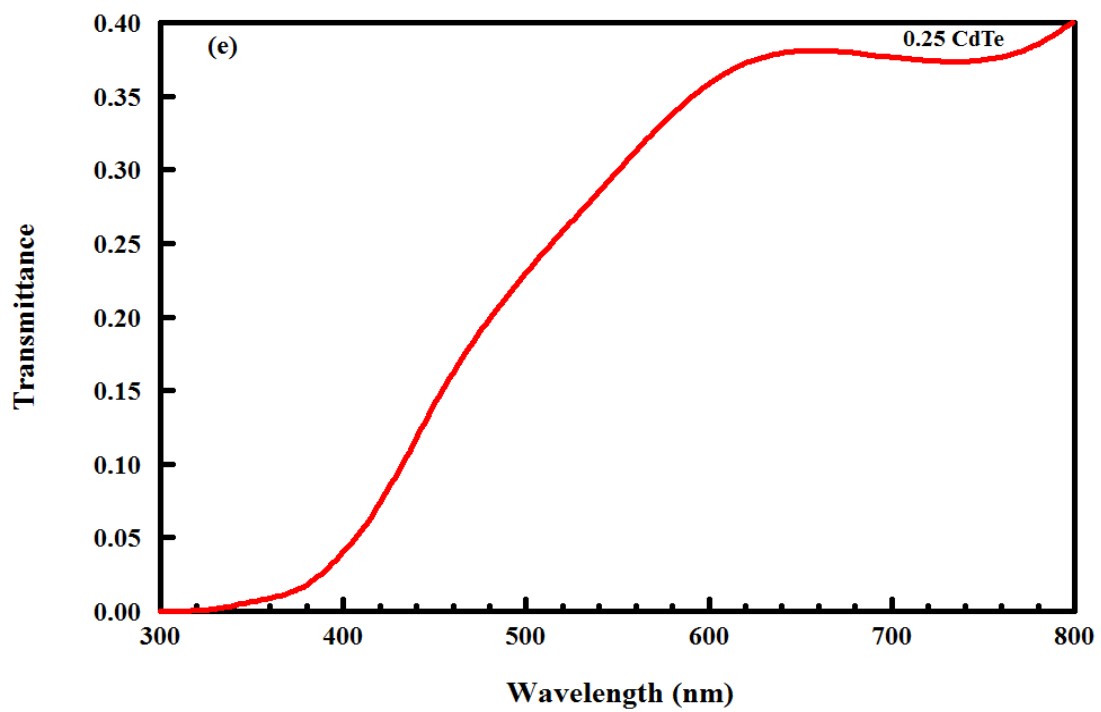
Fig. 4.7 continued.

4.3.2 Thickness measurements

The thickness of the films was measured optically based on the maxima and minima in the transmittance spectra of the films. The maxima and minima appear in the transmittance spectrum due to constructive and destructive interference of light reflected from air/film and film/substrate interfaces, respectively. When a wave of light reflects from the air/film interface and interferes constructively with another wave reflected from the film/substrate interface, a transmittance maximum appears. A transmittance minimum appears if the two reflected waves interfere destructively. Representative maxima and minima are depicted in the transmittance spectrum of a pure WO_3 thin film recorded over the wavelength range 200-2000 nm, as shown in Fig. 4.8. The real thickness (d) of the film was estimated optically using the following relation [122, 123],

$$d = \frac{\lambda_1 \lambda_2}{4n \, |\lambda_1 - \lambda_2|} \tag{4.1}$$

where n is the refractive index of the film, λ_1 is the wavelength corresponding to a maximum (or minimum) transmittance and λ_2 is the wavelength corresponding to an adjacent minimum (or maximum) transmittance. The refractive index was estimated based on the equation of the measured minimum transmittance (t_{min}) given by [123]

$$n = 4.237 - (2.9615 \, t_{min}) \tag{4.2}$$

The thickness of all films was found to be 270 ± 20 nm.
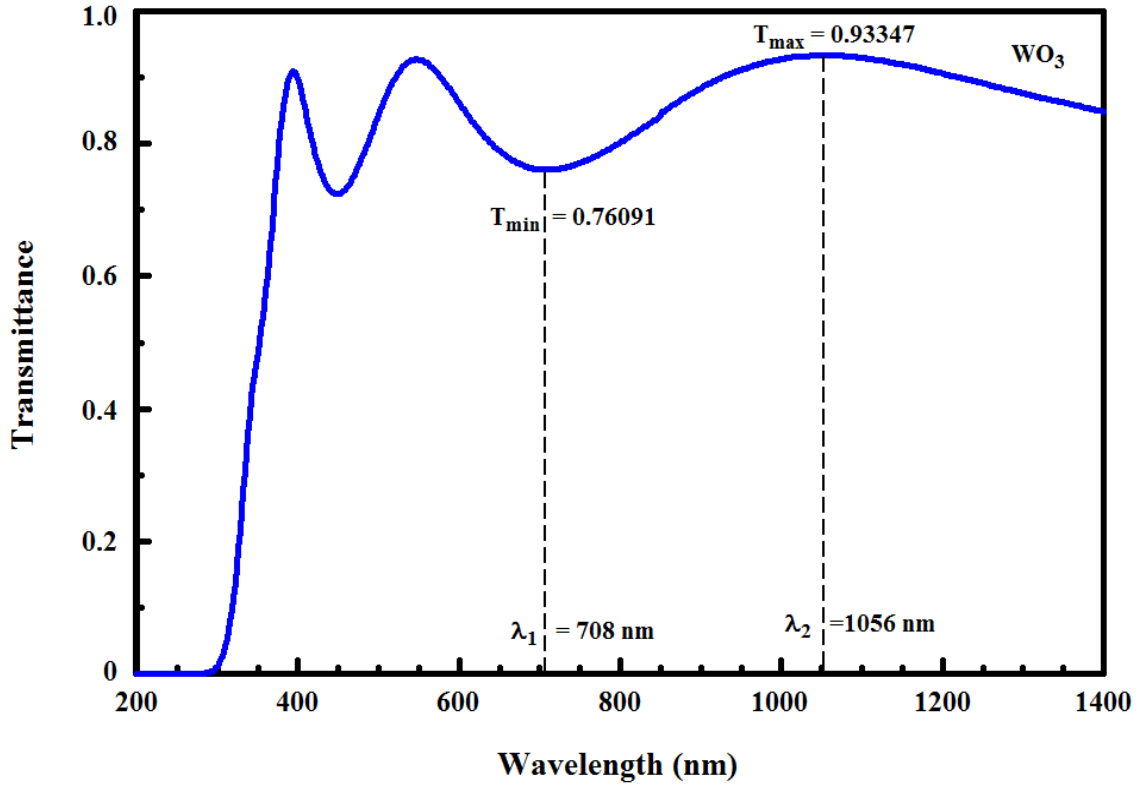
Fig. 4.8 Transmittance spectrum of a WO$_3$ thin film in the wavelength range 200-1400 nm A maximum and an adjacent minimum and their corresponding wavelengths are depicted.

4.3.3 Absorption coefficient

In the fundamental absorption region, the absorption coefficient α is related to the transmittance (*t*) through the following approximate relation [124]:

$$\alpha = \frac{1}{d} \ln \frac{1}{t} \tag{4.3}$$

The absorption coefficients of all films were calculated using eq. (4.3) and are plotted as a function of the wavelength as shown in Fig. 4.9. The absorption edge of pure WO$_3$ thin

film can be observed to shift up towards longer wavelength (red-shift) with the increase

of CdTe content, which supports the previous discussion in the transmittance section.

Moreover, the absorption coefficient also increased gradually with the CdTe content to

reach twice that of pure WO_3 thin film at a CdTe content of 25%. The enhancement of

absorption is attributed to the increase of the CdTe content, which has a high light

absorptivity level [125]. As previously reported [125,126], a film of absorption

coefficient $>10^5$ cm^{-1} over the visible region is able to absorb over 90% of the day light.

This suggests that our new fabricated films can be utilized for absorption of a wide

portion of the visible range of the solar spectrum for energy harvesting applications.
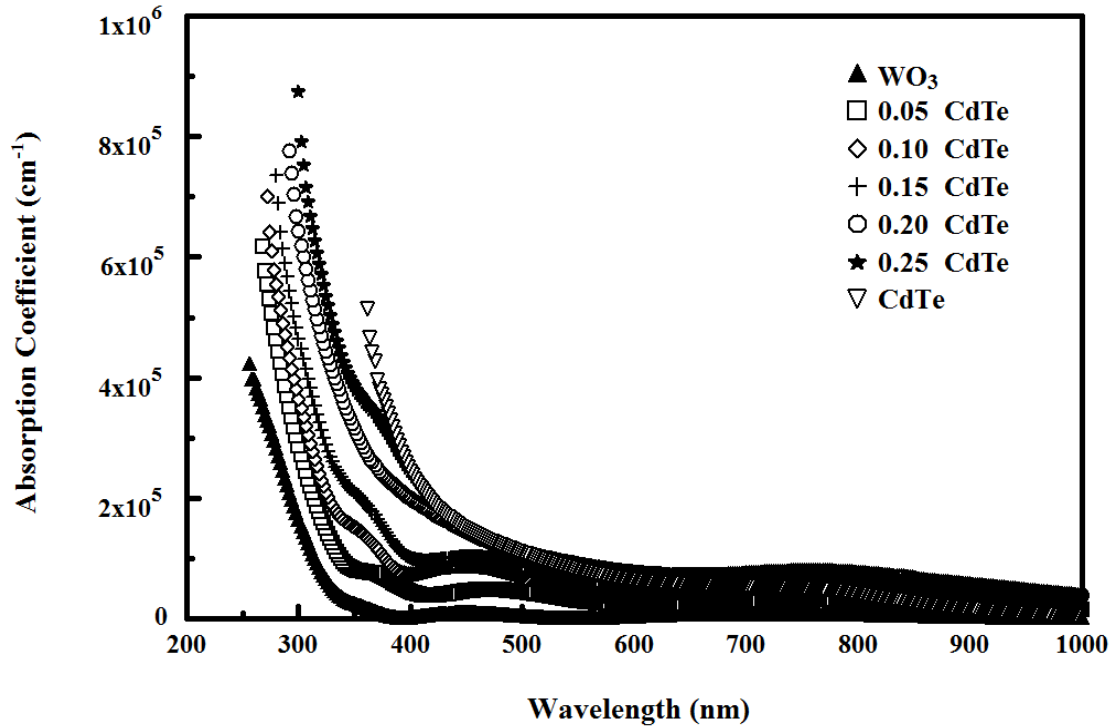
Fig. 4.9 The absorption coefficients of pure WO_3, CdTe and CdTe-alloyed WO_3 thin films as a function of the wavelength.

70

4.3.4 Determination of the optical band gap

The band gap of a semiconductor $\left(E_g\right)$ can be obtained based on the dependence of the absorption coefficient on the incident photon energy (E) in the strong absorption region using the well-known Tauc relation [4,127]:

$$(\alpha E) = \beta\left(h\nu - E_g\right)^{\eta} \tag{4.4}$$

where β is a constant, and the power η describes the optical absorption process. Theoretically, η takes the values 1/2 and 2 for direct and indirect allowed transitions, respectively. Thus, the direct band gap of the CdTe and the indirect band gap of WO_3 and CdTe-alloyed WO_3 thin films can be evaluated by plotting $(\alpha E)^2$ and $(\alpha E)^{1/2}$ versus E, respectively, and extrapolating the linear portions of the plots to intercept the E axis at α = 0. The band gaps were found to be 3.30 eV for WO_3 and 1.42 eV for CdTe, as shown in Fig. 4.10a and 4.10b, respectively. These values are in good agreement with the previously reported values for thermally-evaporated WO_3 and CdTe [128,129]. Figure 4.11 shows the plots of $(\alpha E)^{1/2}$ versus photon energy for the CdTe-alloyed WO_3 films. The band gap values were 3.05, 2.87, 2.75, 2.58 and 2.47 eV at CdTe content of 5%, 10%, 15%, 20% and 25%, respectively. The band gap of the CdTe-alloyed WO_3 films decreased significantly with the increase of CdTe content. As previously reported, an alloyed semiconductor material has often a band gap intermediate between those of its binary compounds [130].

The dependence of the band gap of the alloyed films on the CdTe content (x) was fitted using the quadratic form of the bowing equation (2.21) [131,132]:

$$E_{g,alloy}(\text{x}) = bx^2 + ax + E_g(0) \qquad (4.5)$$

where b is the bowing factor corresponding to nonlinearity in the trend of the band gap values of the alloyed films, $a = E_T - E_W - b$, where E_T is the band gap of pure CdTe, E_W is the is the band gap of pure WO$_3$, and $E_g(0) = E_W$. Figure 4.12 displays the least-squares fitting of equation 4.5 to the experimental data presented in Figs. 4.10 and 4.11, where the best fit values of the parameters a and b were -3.75 and 1.90 eV, respectively. Such a fit confirms that the standard bowing equation described accurately the CdTe content dependence of the band gap of the alloyed films over the whole range of CdTe concentrations. The obtained results reveal the systematic red shift of the band gap of the (WO$_3$) film from 3.30 eV (376 nm) at 0% content of CdTe to 2.47 eV (502 nm) at 25% CdTe of content, indicating that a large portion of the visible spectrum was covered. This means that a wider portion of the visible spectrum region can be harvested rather than only a single wavelength corresponding to the band gap of pure WO$_3$ thin film.
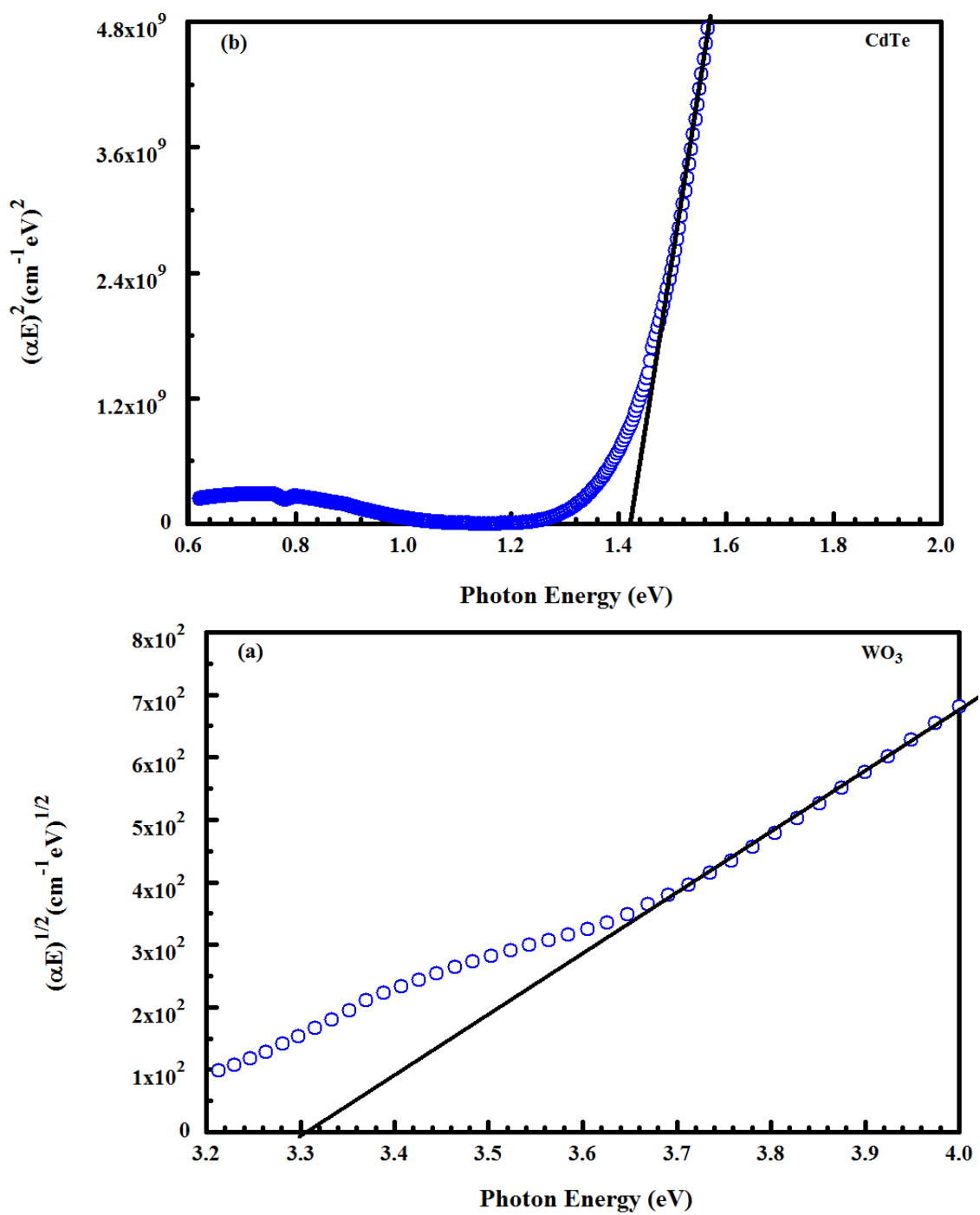
Fig. 4.10 Tauc plot of $(\alpha E)^{1/2}$ and $(\alpha E)^2$ against photon energy for determining the band gap of WO_3 (a) and CdTe (b) thin films, respectively.
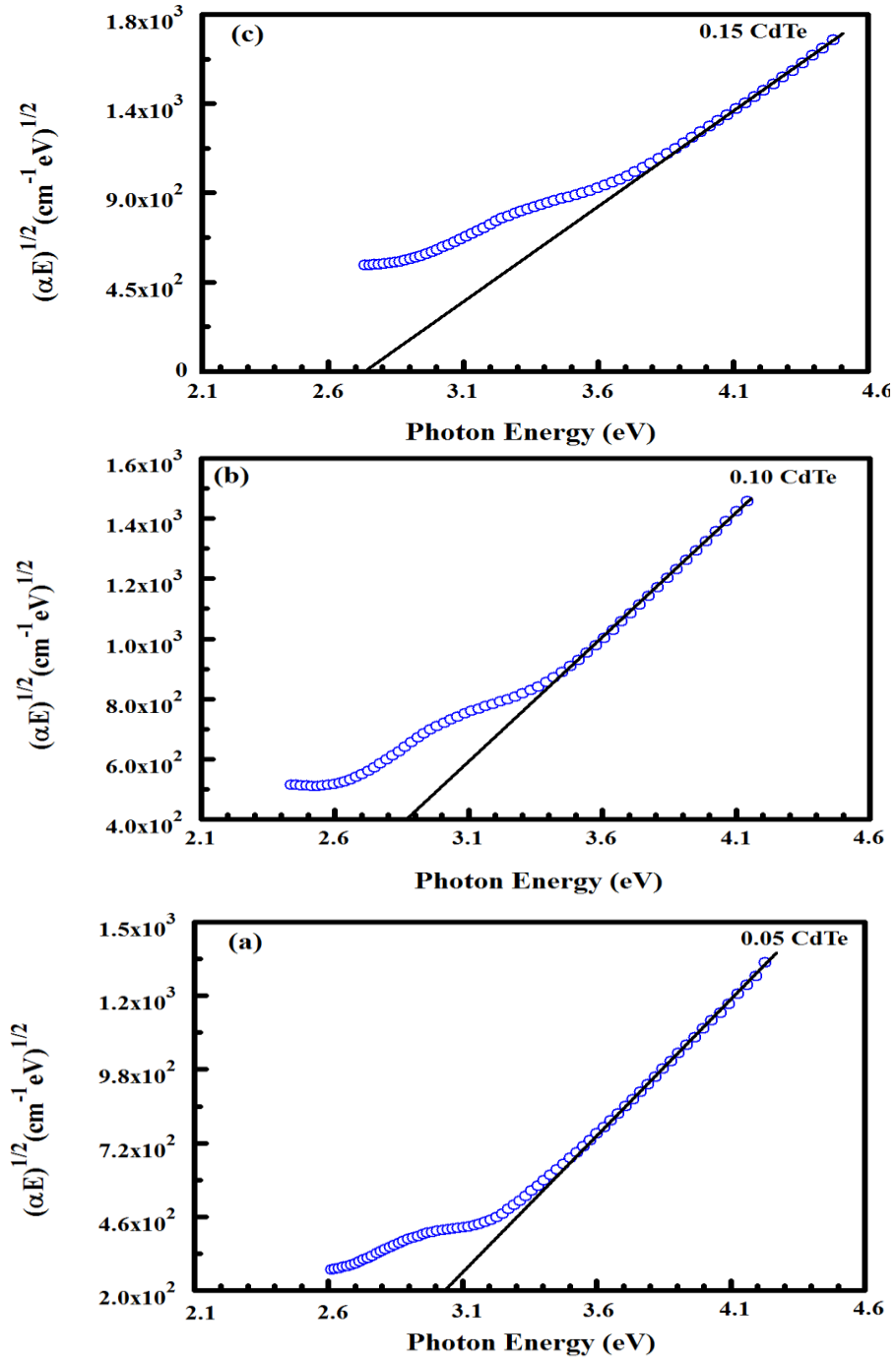
Fig. 4.11 Tauc plot of $(\alpha E)^{1/2}$ against photon energy for determining the band gap of WO_3 thin films alloyed with CdTe mass concentrations of 5% (a), 10% (b), 15% (c), 20% (d) and 25% (e).
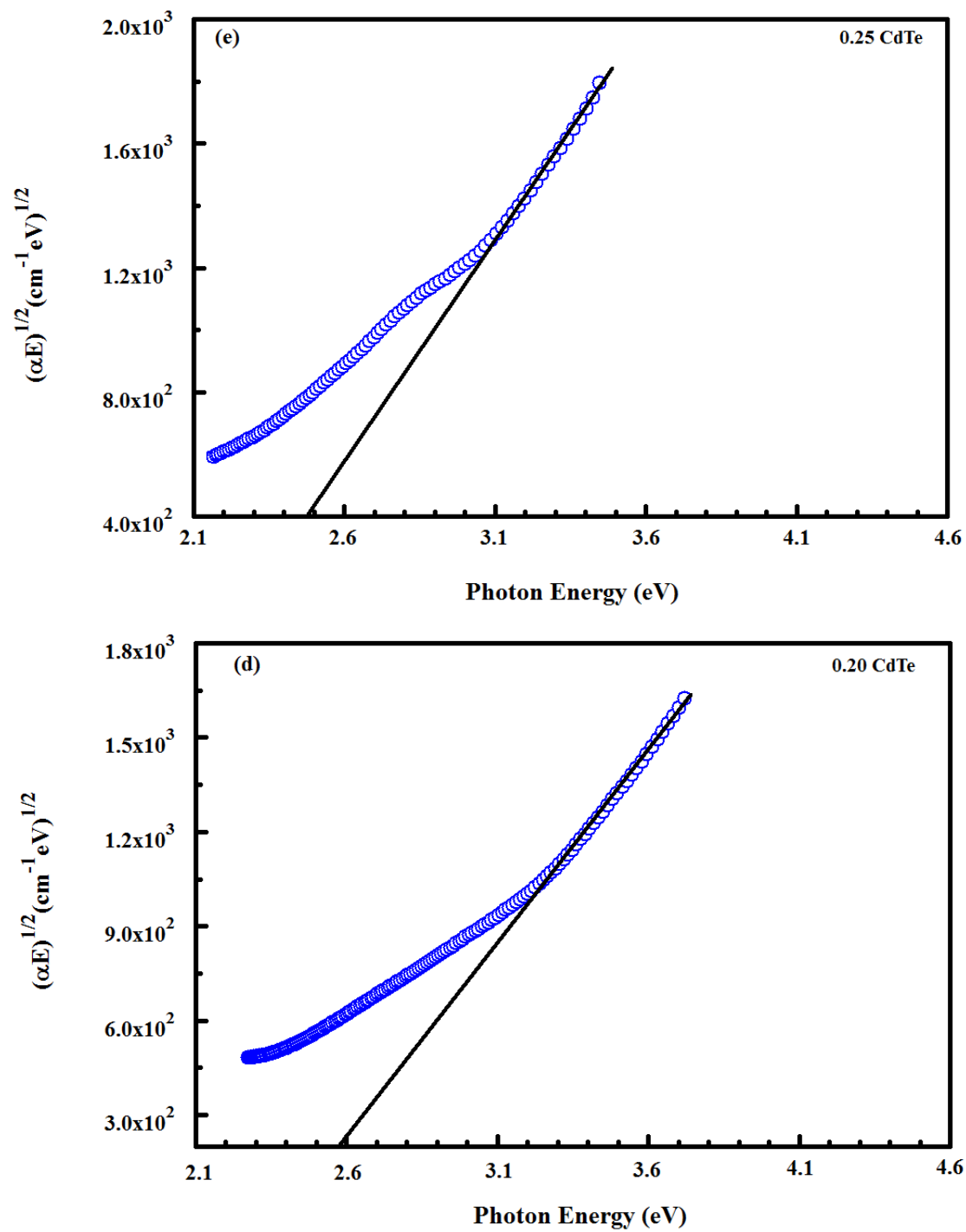
Fig. 4.11 Continued.
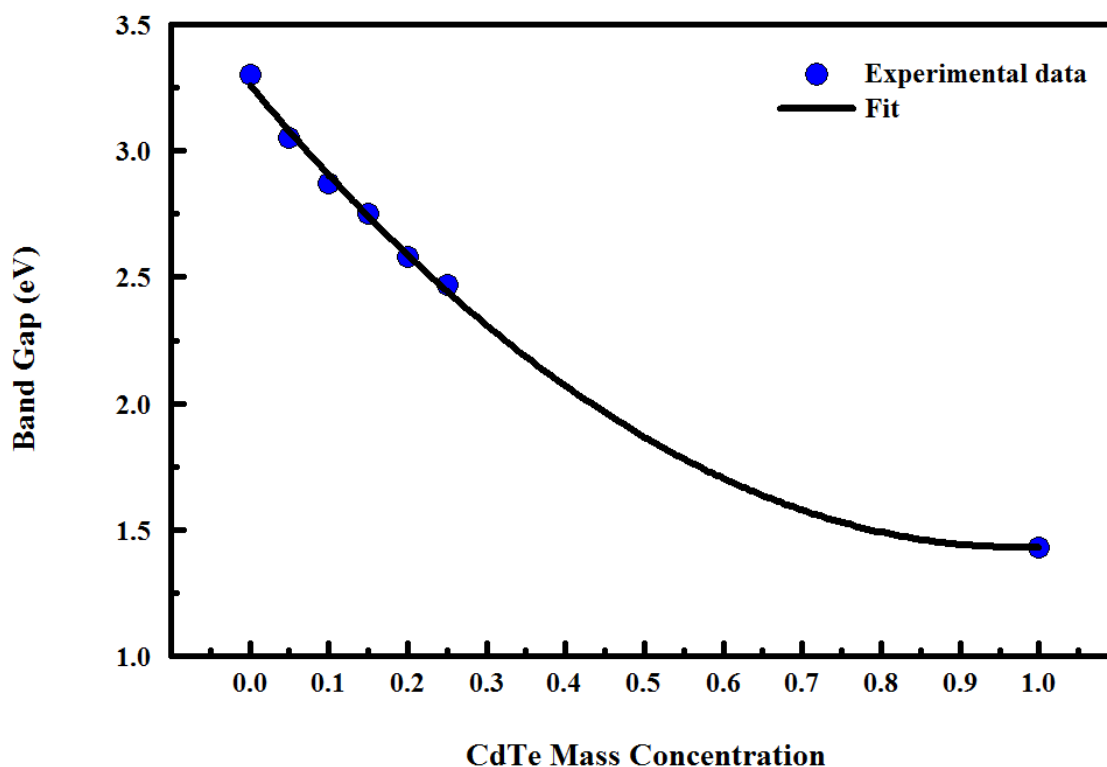
Fig. 4.12 Variation of the band gap of CdTe-alloyed WO$_3$ thin films with CdTe concentration.

4.4 Chemical analysis

4.4.1 XPS analysis of WO$_3$ thin film

The tungsten 4f level consists of two sublevels (W 4f$_{5/2}$ and W 4f$_{7/2}$) which are due to spin-orbit splitting. The spin-orbit splitting is 2.11 eV, and the intensity ratio between W 4f$_{7/2}$ and W 4f$_{5/2}$ peaks in tungsten oxide (WO$_3$) is in the range 0.76 [133-135]. Tungsten has different oxidation states, including WO$_3$ (W^{6+}), WO$_{2.5}$ (W^{5+}), and WO$_2$ (W^{4+}). WO$_3$, having the highest oxidation state, is the stoichiometric oxide. WO$_{2.5}$ and WO$_2$ are sub-stoichiometric compounds [136-149]. The binding energies of W 4f$_{5/2}$ assigned to W^{6+},

W^{5+} and W^{4+} have values in the range 36.5–39.0, 35.7–38.5, and 33.7–38.0 eV, respectively. The corresponding binding energies of W $4f_{7/2}$ have values in the range 35.4–37.0, 33.7–36.4, and 31.2–35.7 eV, respectively [133, 136-145]. A typical XPS survey for the surface of a pure WO_3 thin film is shown in Fig. 4.13, which indicates that the film contains only the constituent elements (W and O). More detailed information about the prepared WO_3 films can be obtained from the high-resolution spectra of W 4f and O 1s. Figure 4.14a shows a high-resolution XPS spectrum in the W 4f core level region, that is splitted into two spin-orbit doublet peaks positioned at binding energies of 35.4 eV and 37.5 eV ascribed to W $4f_{7/2}$ and W $4f_{5/2}$, respectively. The intensity ratio between W $4f_{7/2}$ and W $4f_{5/2}$ peaks is 0.77 and the spin-orbit splitting was 2.10 eV, which are in good agreement with the reported values for W^{6+} oxidation state [133-135]. The presence of other oxidation states in the fabricated thin film can be investigated by deconvolution of the W 4f spectrum using mixed Gaussain/Lorenzain function with iterated Shirley background subtraction, as shown in Fig. 4.14b. It can be observed the presence of two additional small components (statistical weight of 8%) located at binding energies of 34.2 and 36.1 eV, corresponding to W $4f_{7/2}$ and W $4f_{5/2}$ respectively that may be attributed to the W^{5+} oxidation state. The statistical weight of each component is listed in Table 4.1. Similarly, the O 1s core level spectrum was decomposed into two peaks, as shown in Fig. 4.15. The first peak is positioned at a lower binding energy of 530.5 eV and is assigned to oxygen bonded to tungsten (W-O), and the second peak is centered at a higher binding energy of 532.8 eV and is attributed to adsorbed oxygen (O-H) on the surface of the film [135,140,141,146,157]. The ratio of the O-H to the total O 1s peak

was 12%. Finally, the O/W ratio in the fabricated thin film was calculated using the statistical weight of each component due to the following formula [148]:

$$R_{O/W} = \frac{\left(\frac{6}{2}\right) \times \xi^6 + \left(\frac{5}{2}\right) \times \xi^5}{\xi^6 + \xi^5} \tag{4.6}$$

where ξ^6 and ξ^5, are the ratio of W^{6+} and W^{5+} to the total W in the film, and (6/2) and (5/2) are the ratio (oxygen atoms)/(tungsten atoms) in W^{6+} and W^{5+}, respectively.
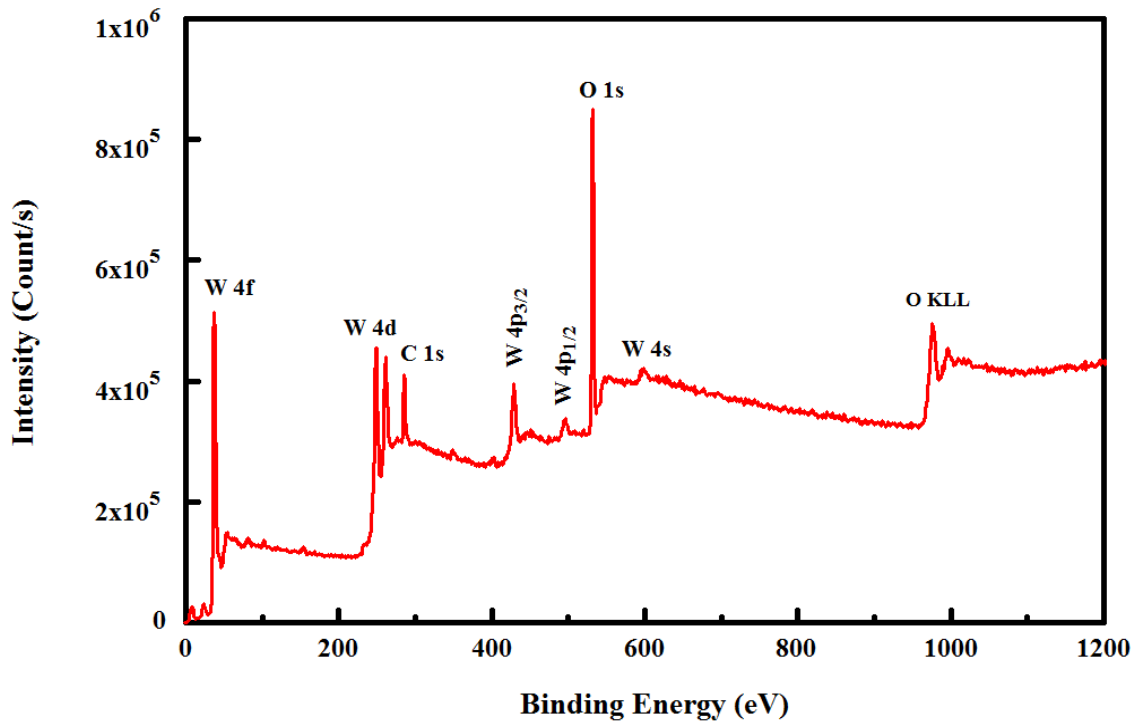
Fig. 4.13 XPS survey spectrum of a WO₃ thin film.
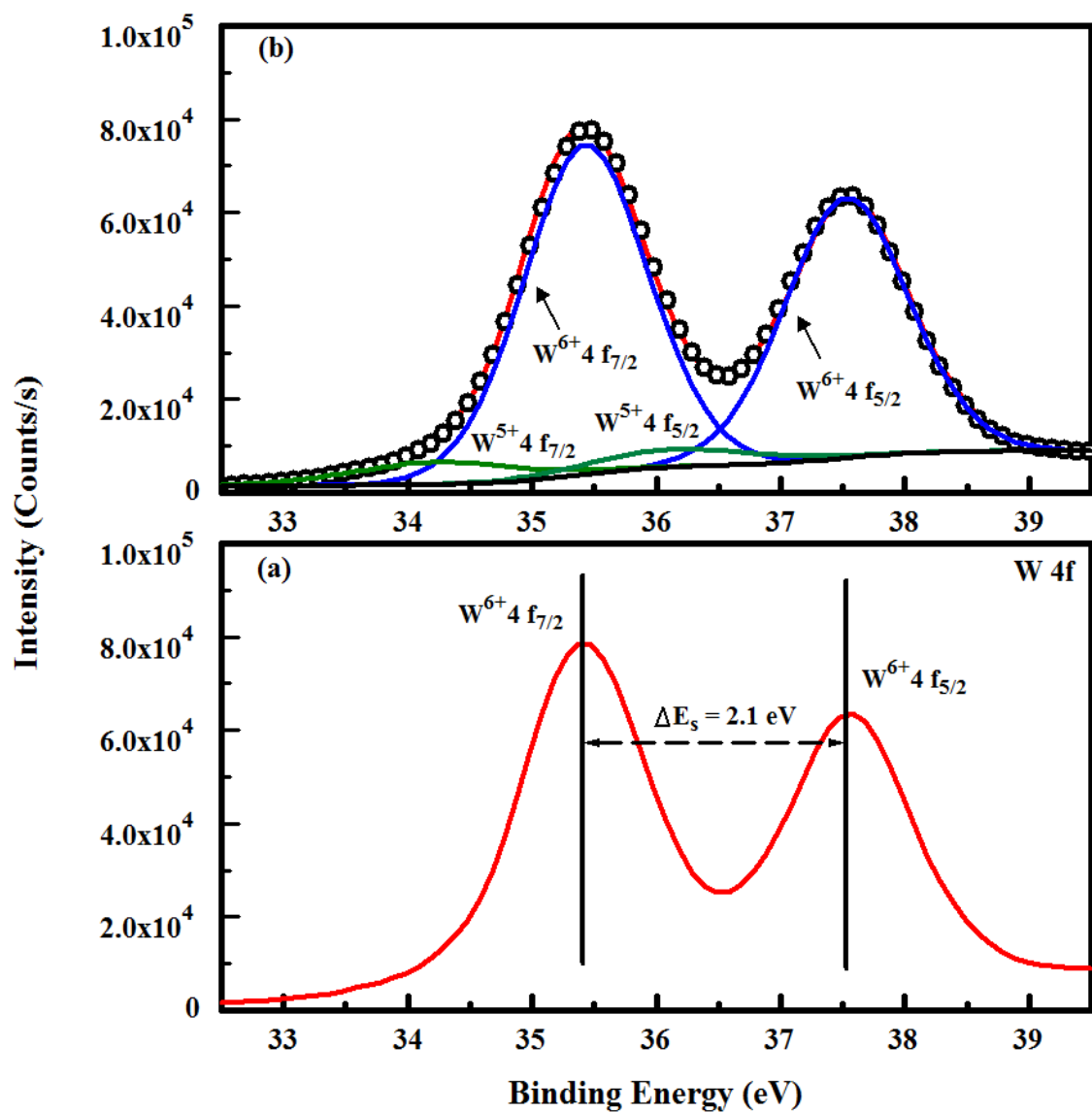
Fig. 4.14 (a) XPS core level spectrum in the W4f region, splitted into two doublet-peaks assigned to W $4f_{7/2}$ and W $4f_{5/2}$ of stoichiometric WO_3 (b) Deconvolution of W 4f spectrum of WO_3 thin film into four components, as indicated on the curves.
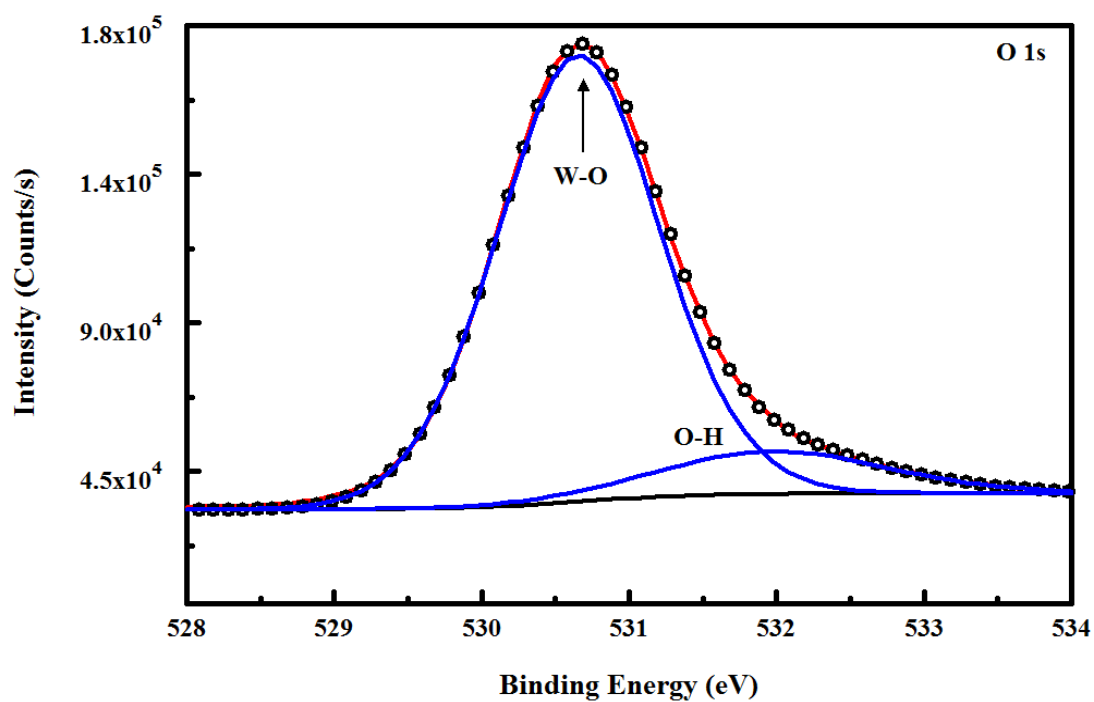
Fig. 4.15 Deconvolution of O 1s core level spectrum into two components in WO$_3$ thin film.

Table 4.1: Deconvolution results of W 4f spectrum of WO_3 thin film with corresponding binding energies (BE), statistical weight and full-width at half maximum (FWHM) of each component Ratio of sub-stoichiometric oxide (W^{5+}) to the total W and ratio of oxygen to tungsten in the film are also listed.

Component	Peak BE (eV)	FWHM (eV)	Area (CPS)	Statistical weight	W^{5+}/W	$R_{O/W}$
$W^{6+}4f_{7/2}$	35.4	1.18	90112.27	91.58		
$W^{5+}4f_{7/2}$	34.2	1.57	8288.03	8.42	0.08	2.96
$W^{6+}4f_{5/2}$	37.5	1.18	71037.41	-		
$W^{5+}4f_{5/2}$	36.1	1.57	6533.63	-		

4.4.2 XPS analysis of CdTe thin film

The surface chemistry of pure CdTe thin films was also investigated using XPS. The XPS survey spectrum for a CdTe film is shown in Fig. 4.16, which confirms the presence of Cd and Te only, without the presence of further elements, except oxygen and carbon originating from the environment. Figure 4.17a displays the characteristic XPS spectrum in the Te 3d region, that shows two doublet peaks (Te $3d_{5/2}$ and Te $3d_{3/2}$) centered at binding energies of 572.9 and 583.3 eV, respectively, and assigned to Cd-Te bonds [149-153]. Besides, two corresponding satellite peaks were positioned at binding energies of 576.2 and 586.7 eV, and are attributed to Te-O bond found in TeO_2 [154-157]. The binding energy difference between Te $3d_{5/2}$ and Te $3d_{3/2}$ is almost 10.4 eV, which agrees with the reported values [155,157,158]. In order to investigate the existence of additional oxidation states, the main and satellite Te $3d_{5/2}$ peaks were fitted as shown in Fig. 4.17b. The resulted fitting showed that no further components were present, indicating that the main component of the film is Cd-Te bond with a small amount of Te-O bond (only 3% of the total Te 3d peak) due to exposure to oxygen emerging from WO_3 during deposition. In addition, the energy difference between the two Te $3d_{5/2}$ signals assigned to Te-Cd and Te-O bonds is 3.3 eV, which is also in good agreement with the previous reports [162]. The statistical weight of each component is presented in Table 4.2. Similarly, the Cd 3d core level region shows two doublet peaks (Fig. 4.18a) positioned at binding energies of 405.5 and 412.2 eV, and ascribed to Cd $3d_{5/2}$ and Cd $3d_{3/2}$ doublet peaks found in Cd-Te bonds, respectively [149-151,160,161]. The energy difference between these two doublets is 6.7 eV, which is in good agreement with the literature

[155, 161]. To investigate the possibility of the formation of Cd-O bond, the Cd $3d_{5/2}$ peak was fitted as can be observed in Fig. 4.18b. The fitted curve does not show any further peaks, indicating that the only formed bonds are Cd-Te bond. The statistical weight of Cd component is given in Table 4.2.
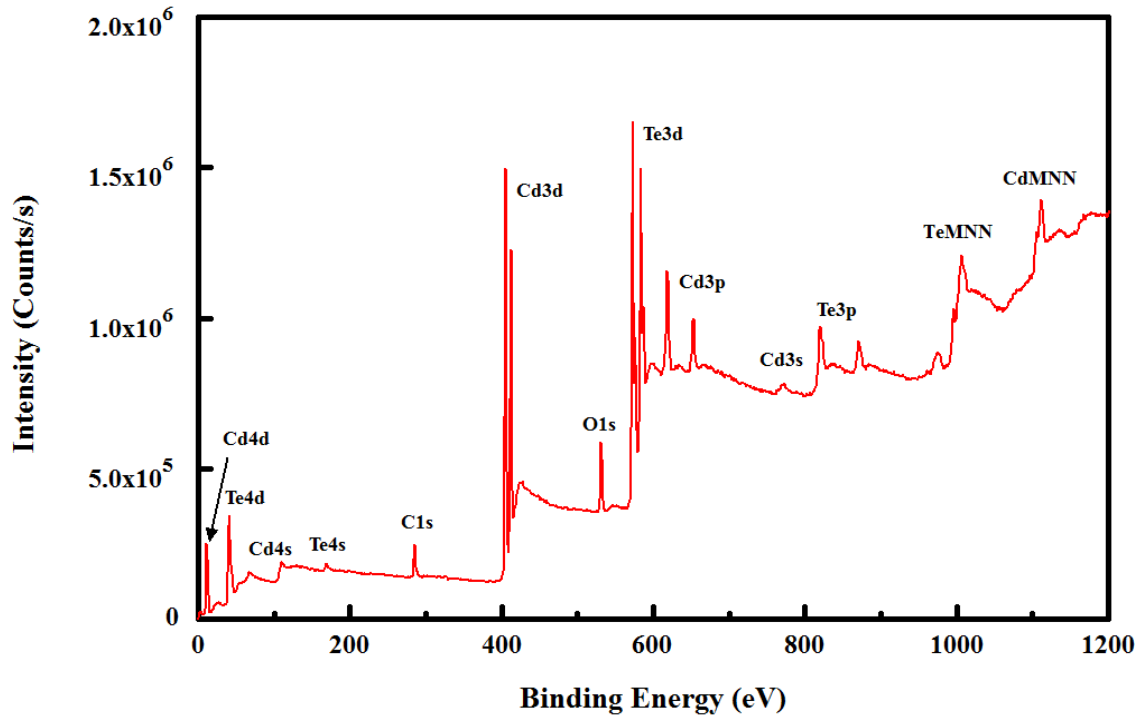
Fig. 4.16 XPS survey spectrum for CdTe thin film.
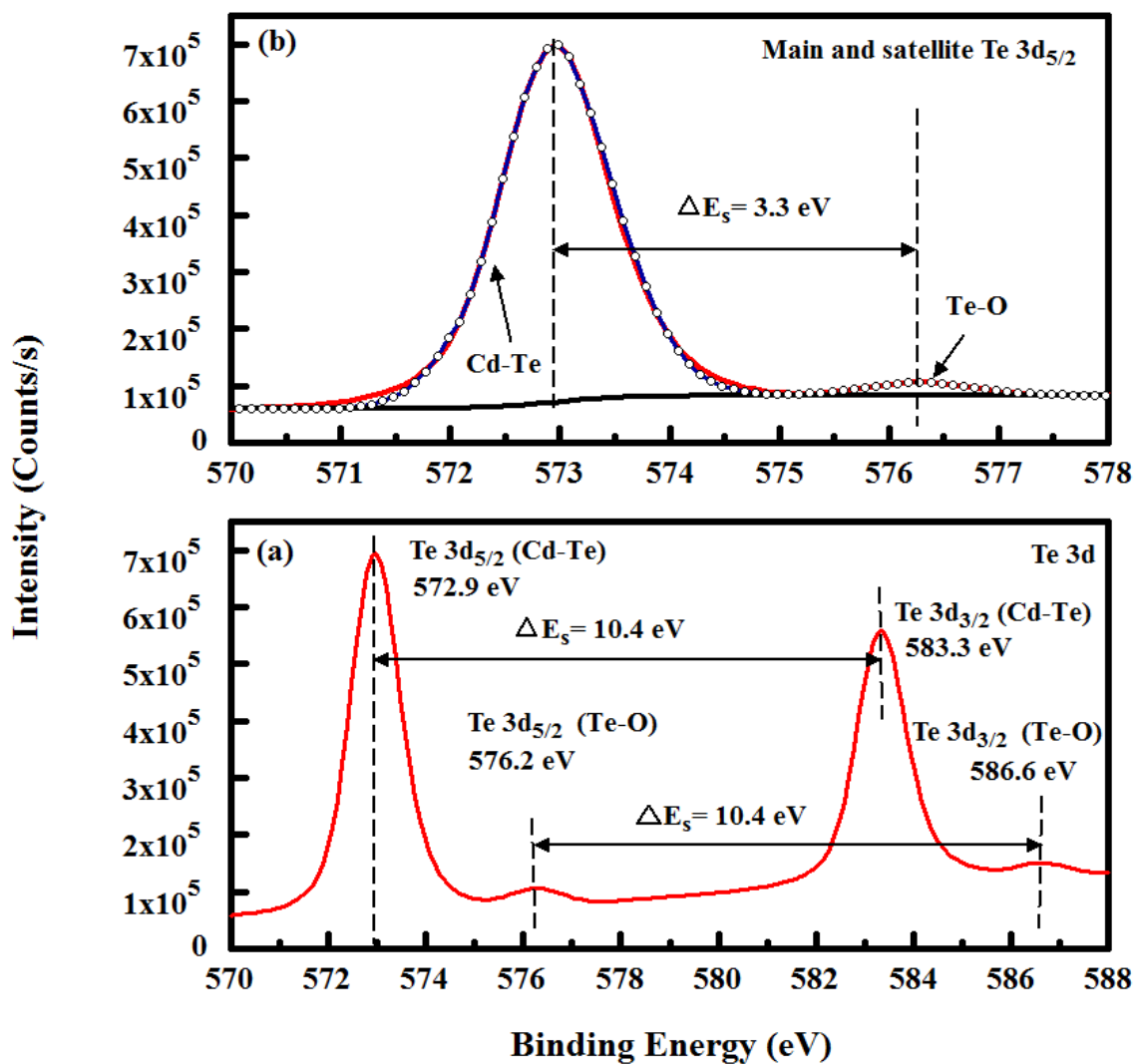
Fig. 4.17 (a) XPS spectrum of the core level of Te 3d region (b) Fitting of main and satellite Te 3d$_{5/2}$ peaks of CdTe thin film showing that no further oxidation states were present
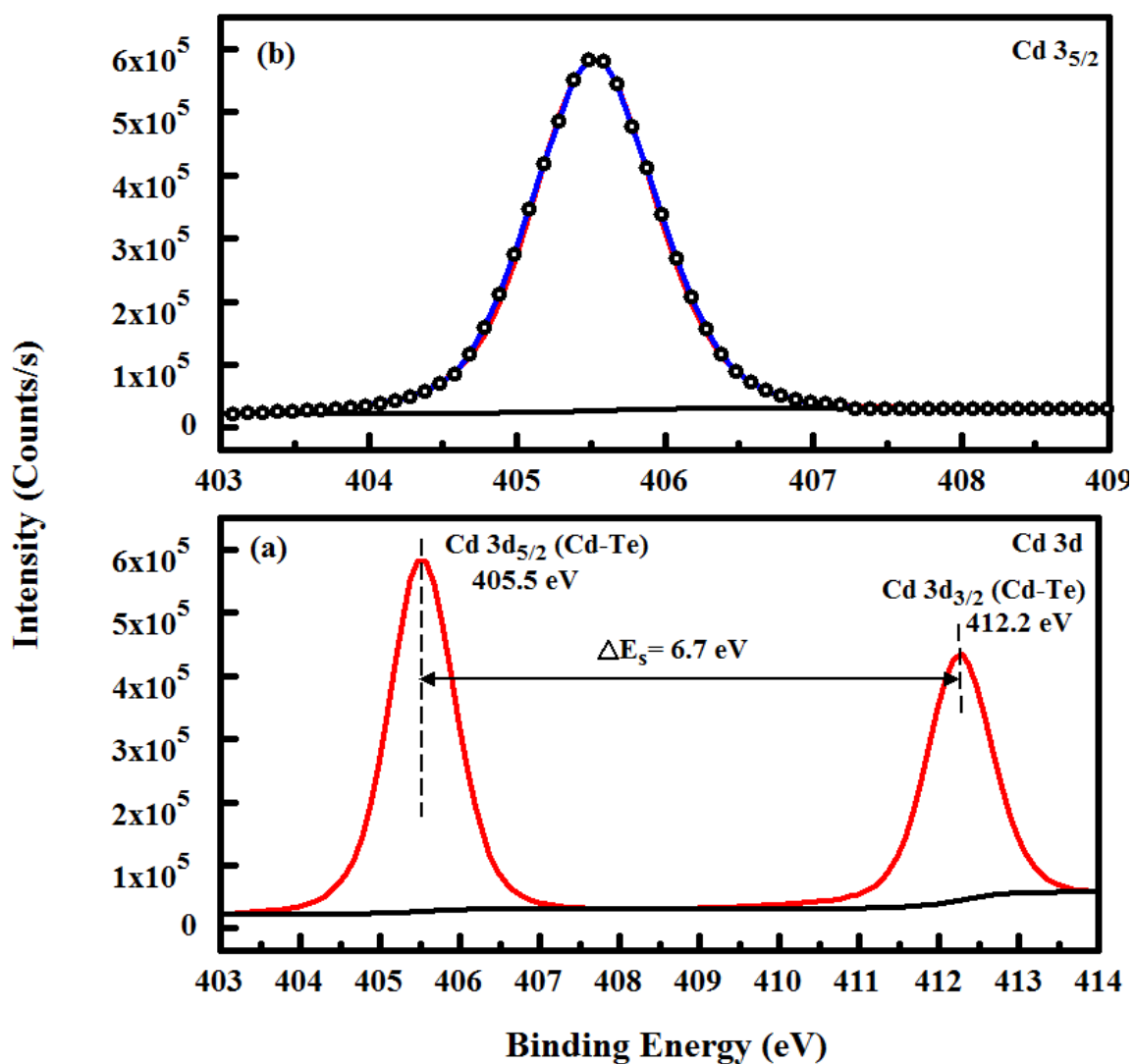
Fig. 4.18 (a) XPS spectrum of the core level of Cd 3d region (b) Fitting of Cd 3d$_{5/2}$ peak of CdTe thin film showing that no further oxidation states were present.

Table 4.2: Deconvolution results of Te3 $d_{5/2}$ and Cd3 $d_{5/2}$ peaks of CdTe thin film with corresponding binding energies (BE), statistical weight and full-width at half maximum (FWHM) of each component Ratio of Te to Cd and ratio of oxidized tellurium (Te-O) to the total Te in the film are also listed.

Component	Peak BE (eV)	FWHM (eV)	Statistical Weight	Te/Cd	Te-O/Te
Cd (Cd-Te bond)	405.5	1.03	50.09		
Te (Cd-Te bond)	572.9	1.27	48.24	0.97	0.03
Te-O	576.2	1.17	1.66		

4.4.3 XPS depth profiling of WO₃/CdTe thin films

XPS depth profiling of a thin film involves etching the surface of the film with an Ar^+ ion source, recording XPS intensity-etching time spectra, and repeating the process down through the thickness of the film to produce a profile of the distribution of the constituent elements within the film. In order to characterize the depth distributions of the components in each film, XPS depth profiling was obtained by plotting the intensities (corrected by the sensitivity factor of each element) of each component as a function of etching time. The etching time was not converted into depth because of the variation of the etching rate between the different components in the film. Figs. 4.19-4.23 show XPS depth profiling of WO₃/CdTe films prepared at CdTe concentrations of 5%, 10%, 15%,

20% and 25%, respectively. For the two films prepared at 5% (Fig. 4.19a) and 25% (Fig. 4.23a) CdTe, it can be seen that both Cd and Te components evolved gradually starting from the bottom side of the film towards the top side of the film. However, at etching times of 540 s and 360 s, a sharp increase in Cd and Te intensities can be observed, followed by a gradual decrease in the film alloyed with 5% CdTe until the etching time of 420 s, and abrupt decrease in the film alloyed with 25% CdTe until the etching time of 300 s. Eventually, their intensities leveled off as the sputtering time decreased until the top side of the film. Such a sharp evolution indicates that most of the CdTe material was exhausted, and may be explained in terms of the melting point of the material and the minimum energy necessary for evaporation. The abundance of CdTe material in the films at etching time of 540 s and 360 s suggests that the energy of evaporation increased to a value greater than that needed to melt CdTe (melting point of 1098 ^{o}C), which led to a high evaporation rate and hence consuming the material at this layer. Besides, W and O components evolved gradually from the bottom side of each film until etching times of 500 s and 300 s, and then their intensities increased smoothly until reaching the top side of each film as can be seen in (Fig. 4.19b) and (Fig. 4.23b), respectively. This continuous increase in the amount of W and O with the decrease in the etching time is due to the great amount of raw WO_3 material as well as longer period of evaporation is needed because of the higher melting point of WO_3 (1473 ^{o}C) compared to that of CdTe. A representative XPS depth profile spectra of all components in the $(WO_3)_{0.95}$ $(CdTe)_{0.05}$ thin films are depicted in Fig. 4.24.

No attempt was made to investigate the oxidation states in each fabricated $(WO_3)_{1-x}$ $(CdTe)_x$ thin film for two reasons; first one is the removal of the C1s peak reference at the first etched layer as can be viewed in Fig. 4.24e and the second reason is the shifted photoelectron peak positions due to the Ar^+ ion sputtering as can be seen in Figs. 4.24a-c. However, it was reported that ion bombardment of metal oxides leads to preferential sputtering of oxygen leaving metal-enriched surface and formation of sub-stoichiometric oxides [162-164].The phenomenon was observed in most sputtering runs but the increase in the metal signal means the increase of the metal atoms which was not believed and explained by the increase in the amorphicity of the film due to the sputtering. In our study, such phenomenon was observed in some samples where the intensity of W was greater than that of O at the late stages of etching. A similar trend was reported in thermally evaporated WO_3 films by Driscoll *et al.* [162] with the formation of other sub-stoichiometric oxides such as WO_2 and $WO_{2.6}$ due to Ar^+ ion sputtering. Based on this consideration, the presence of the original stoichiometric WO_3 is reasonably assumed.

At CdTe concentrations of 10% (Fig. 4.20a) and 20% (Fig. 4.22a), the Cd and Te components showed steady level of growth starting from the substrate surface toward the uppermost side of the film but significant increase in their intensities at etching time of 240 s can be observed due to the high evaporation rate indicating that most of the CdTe material was consumed at this layer, then a sudden drop in their intensities can be noticed at etching time of 180 s followed by a steady decrease until reaching the upper surface of the film. Similarly, W and O elements (Fig. 4.20b) and (Fig. 4.22b) grew steadily along with Cd and Te components from the bottom side to the top side of the film with a sharp

increase at etching time of 180 s, then they proceed in growth smoothly until reaching the topmost surface of the film. Furthermore, a relative W metal-enriched layer was formed after the early stages of etching, specifically at etching time of 420 s, and dominated the exposed surfaces of the film until the bottom side of the film. On other hand, the intensity of each component reflects the number of photoelectrons detected during acquisition of XPS data so one can expect that the intensities of Cd and Te components in each film increase with the increase of their concentrations. However, such expectation was not met in all samples. As reported, even for samples of the same thickness, the intensity from run to run is not the same due to the slow decrease in the sensitivity of the detector over time caused by adsorption of water vapor and other materials upon the cold detector surface [162]. Finally, in the films prepared at a CdTe concentration of 15%, it can be noted that the Cd and Te components (Fig. 4.21a) were distributed in the film with similar mechanism noted in the film prepared at CdTe concentration of 20% where their evolution was steady along with the etching time but with a remarkable increase at the middle layer of the film due to the high evaporation rate at this layer. However, W and O components (Fig. 4.21b) were distributed in the film in a mechanism similar to that observed in the film prepared at CdTe concentration of 25% where both components were evolved gradually from the top surface of the substrate toward the upper side of the film with great and relative enrichment of O on the exposed layer of the film at the early and lately stages of etching, respectively.

The enrichment of Te and Cd through the depths of the films prepared at 5% and 10% CdTe content respectively indicates the difference in the CdTe stoichiometry which can

be explained by the formation of oxide layers due to the change of the chemical states in the material caused by ion sputtering [165,166]. However, only few exposed surfaces in the films prepared at 15%, 20% and 25% CdTe content are enriched with Te. As a result, it can be stated that all constituents; Cd, Te, W and O were non-uniformly distributed throughout the thickness of the films due to their variation from site-to-site in a single film.
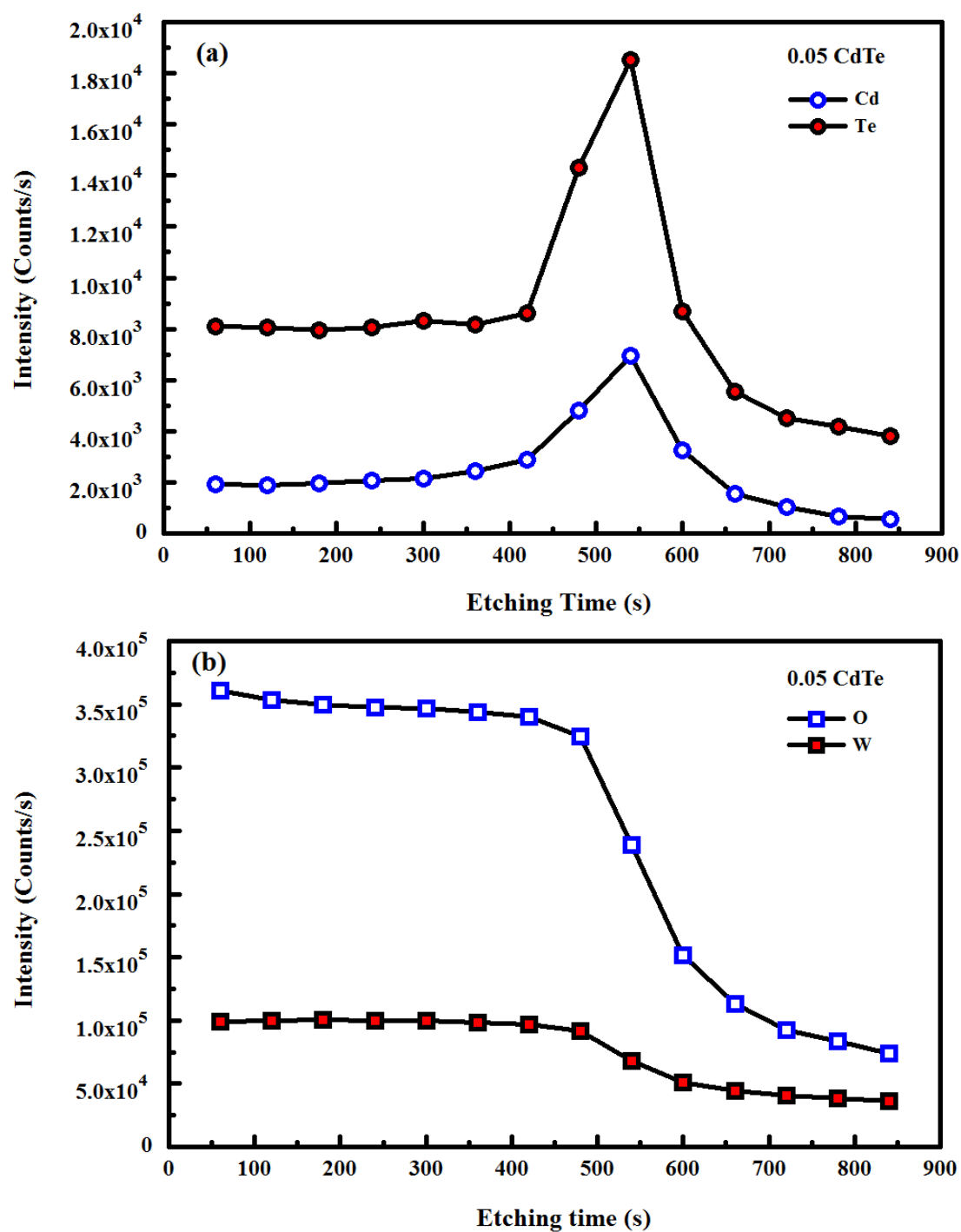
Fig. 4.19 XPS signal intensity versus etching time for WO₃ thin film alloyed with 5% CdTe, (a) Cd and Te components, (b) W and O components.
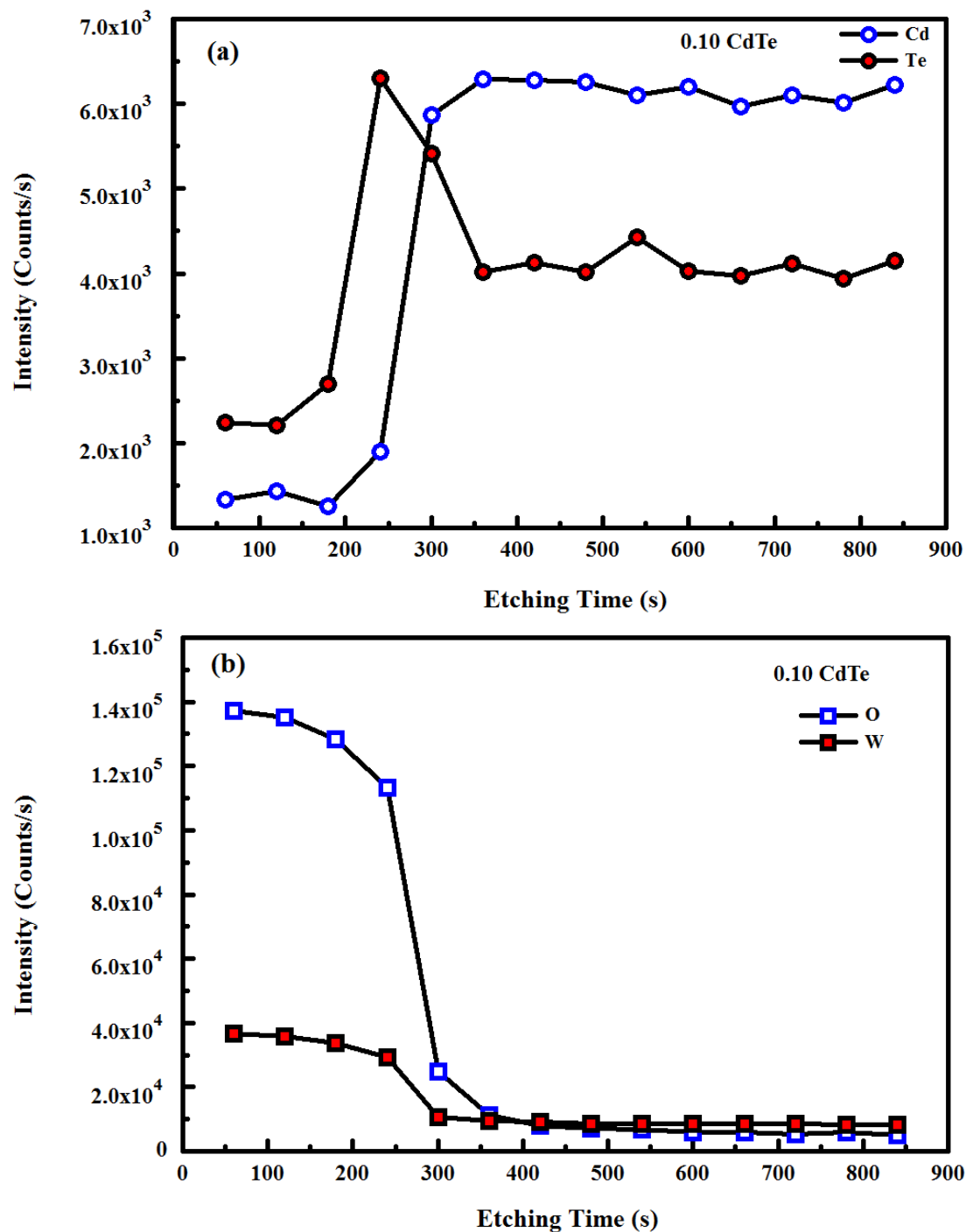
Fig. 4.20 XPS signal intensity versus time for WO₃ thin film alloyed with 10% CdTe, (a) Cd and Te components, (b) W and O components.
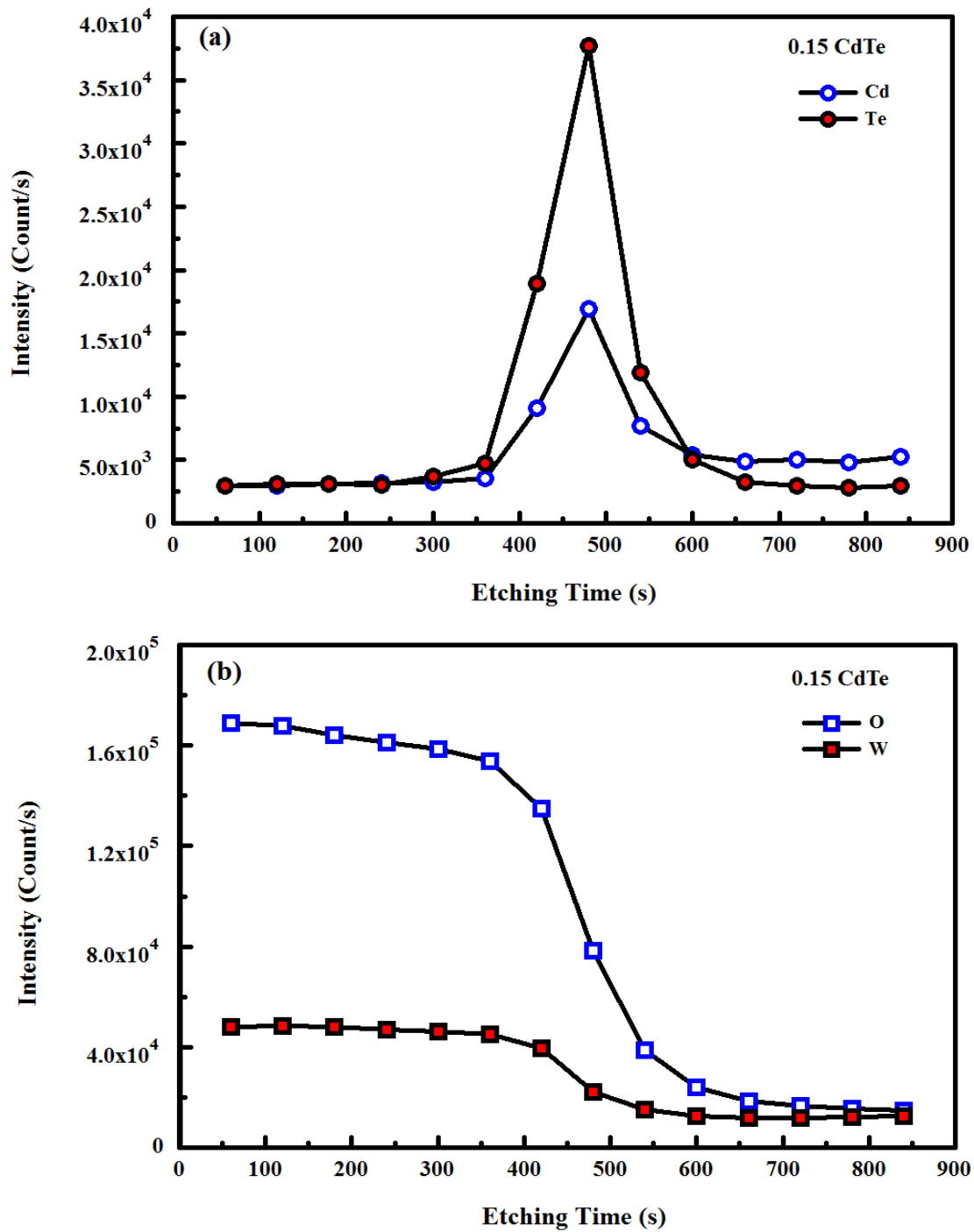
Fig. 4.21 XPS signal intensity versus etching time for WO$_3$ thin film alloyed with 15% CdTe, (a) Cd and Te components, (b) W and O components.
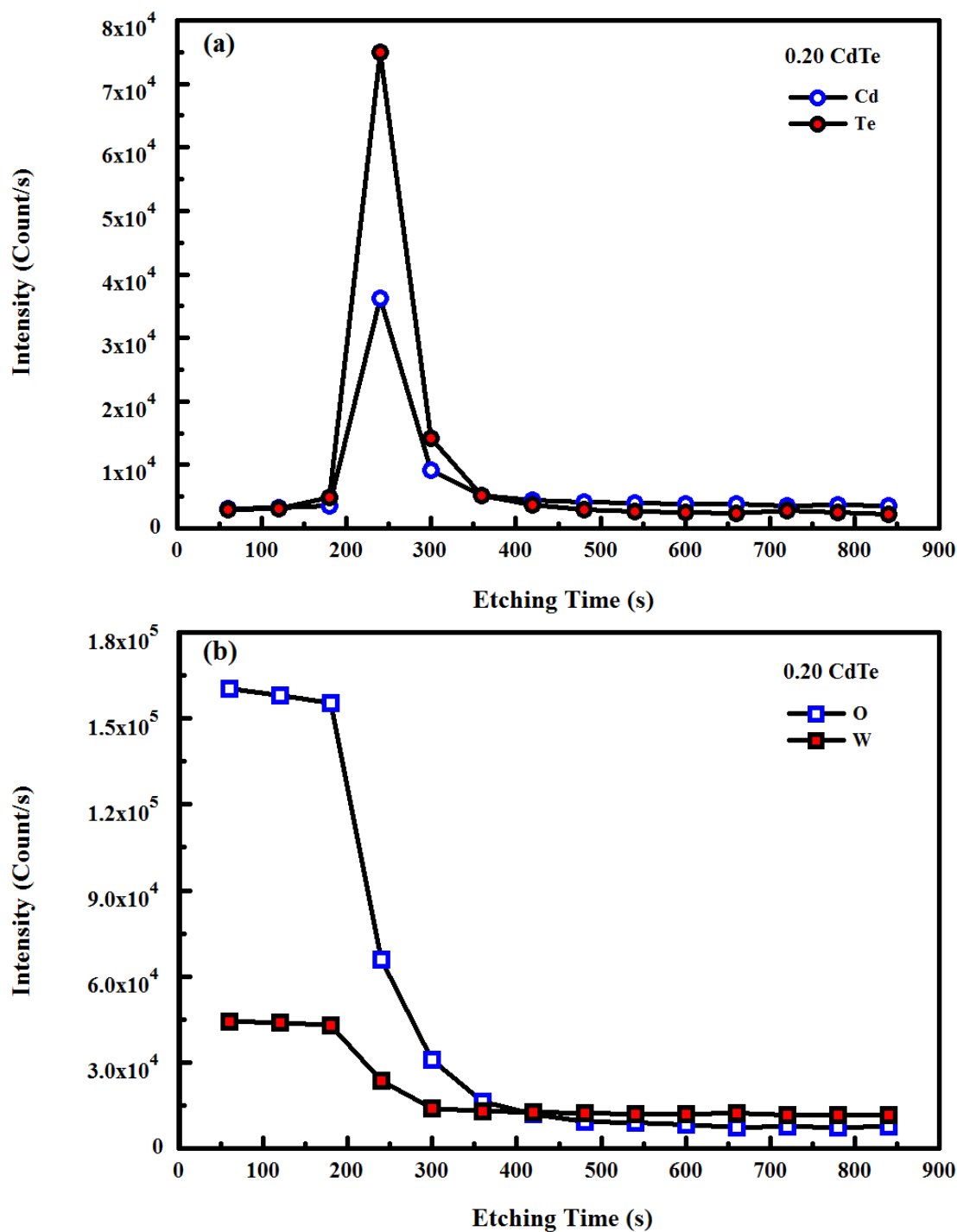
Fig. 4.22 XPS signal intensity versus etching time for WO₃ thin film alloyed with 20% CdTe, (a) Cd and Te components, (b) W and O components.
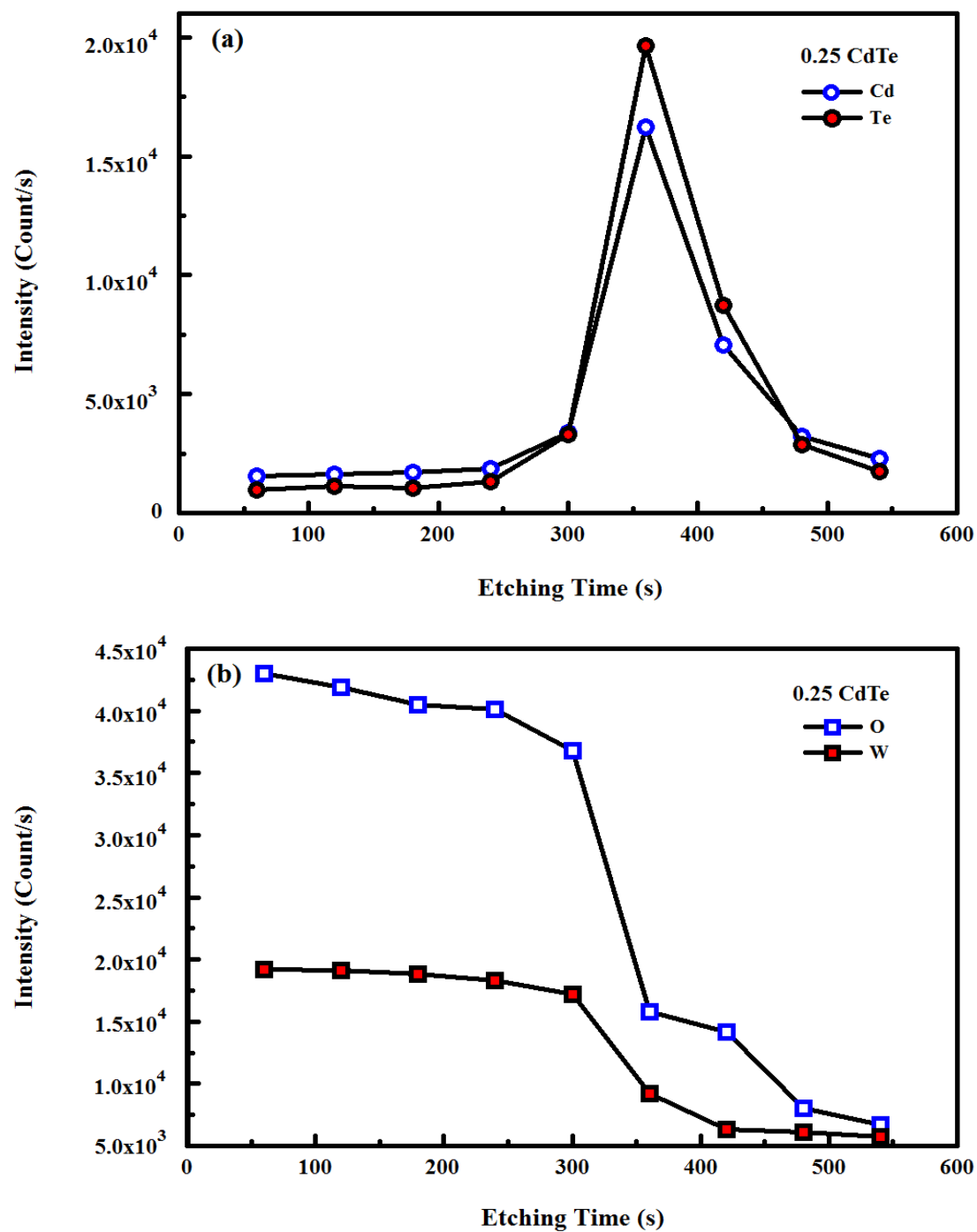
Fig. 4.23 XPS signal intensity versus etching time for WO$_3$ thin film alloyed with 25% CdTe, (a) Cd and Te components, (b) W and O components.
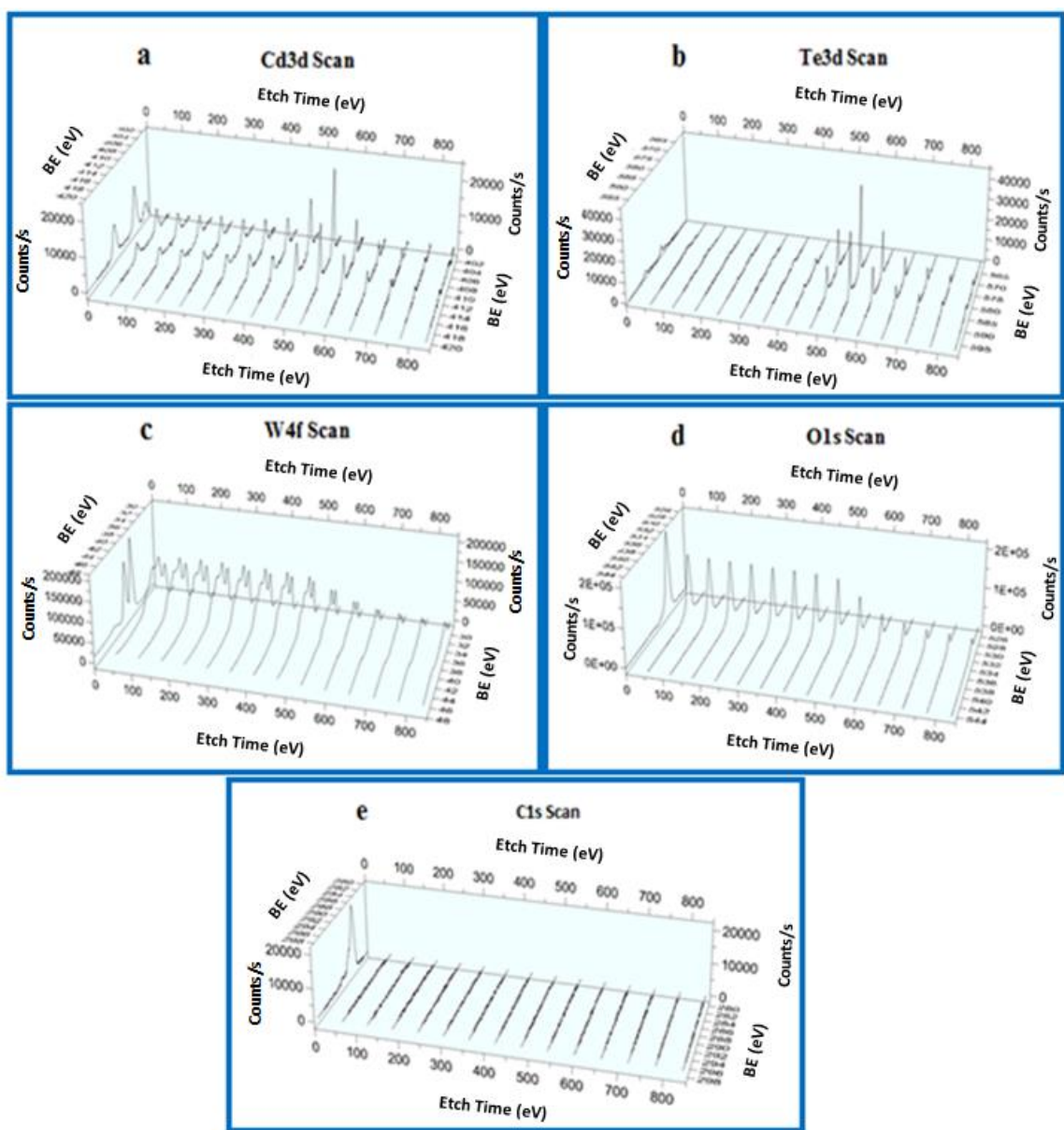
Fig. 4.24 XPS depth profile scan of (a) Cd 3d, (b) Te 3d, (c) W 4f, (d) O 1s and (e) C 1s regions in the WO₃ thin film alloyed with 5% CdTe.

4.5 Photocurrent measurements

The suitability of the CdTe-alloyed WO_3 thin films for photovoltaic applications was investigated by measuring the photocurrent density of the films. Figure 4.25a shows the variation of the photocurrent density of the fabricated films at various CdTe concentrations. It can be observed that the photocurrent density of the alloyed films increased monotonically with the applied potential. This increase is attributed to the enhanced mobility of the photogenerated excitons due to the increase of the band bending at the film/electrolyte interface [167]. Furthermore, applying a positive potential enables the separation of the photogenerated electrons and holes leading to enhancement of the photocurrent [168]. The dependence of the photocurrent density of the alloyed films on the CdTe concentration is shown in Fig. 4.25b, which represents the integrated area under the photocurrent density−potential curves versus CdTe concentration. Obviously, the photocurrent density increased gradually with the CdTe concentration to reach a maximum value at a CdTe concentration of 20%. This is ascribed to the decrease of the band gap of the alloyed films with CdTe concentration, which improves the light absorption at longer wavelengths, resulting in the enhancement of the photogenerated excitons [169]. However, the photocurrent density decreased at higher CdTe concentration (25%) despite its low band gap. This could be attributed to the increase of the impurity scattering centers at the grain boundaries in the film due to the increase of CdTe concentration, which in turn leads to the decrease of the photogenerated electron mobility and the enhancement of their recombination with diffusing holes [170,171].
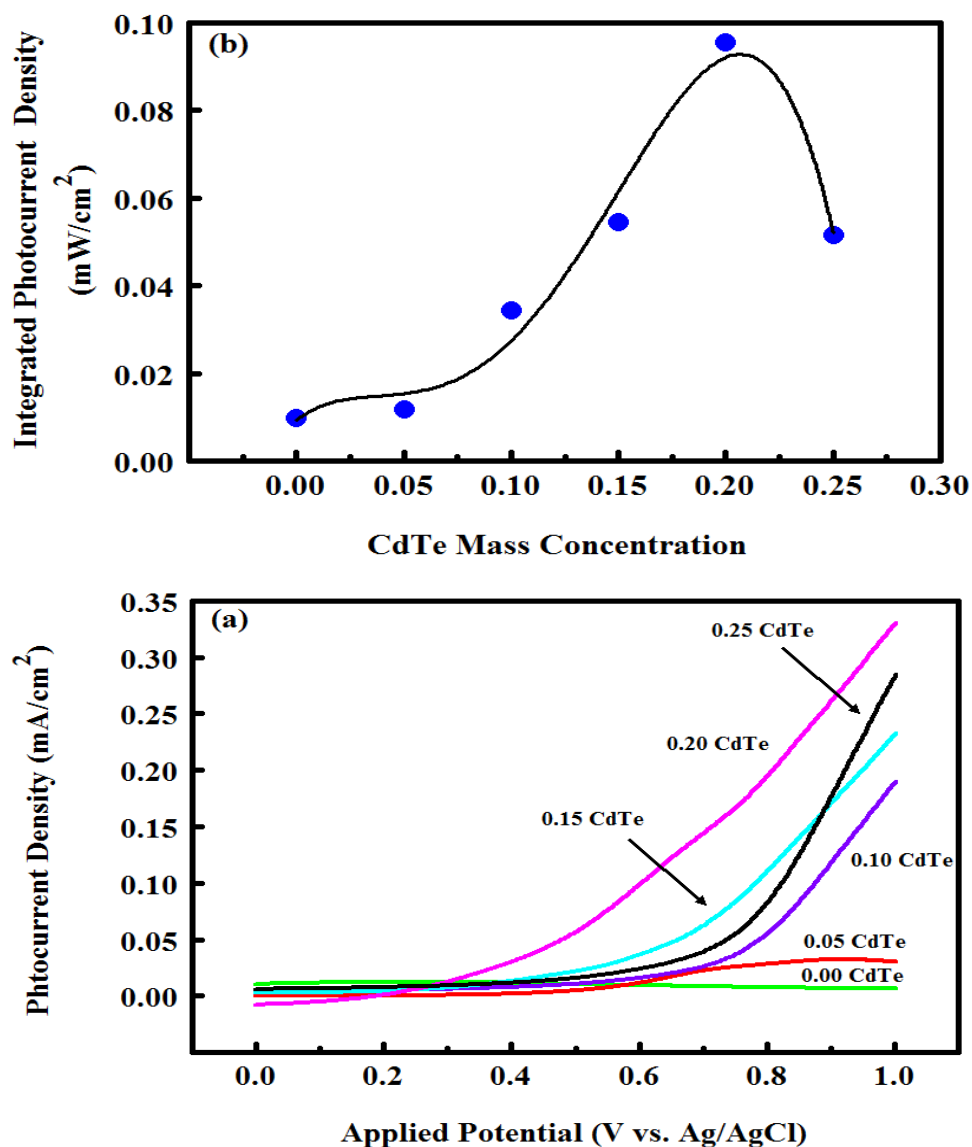
Fig. 4.25 (a) Photocurrent density-voltage curves of the pure and alloyed WO$_3$ thin films under light illumination with an artificial sunlight simulator (300 mW/cm^2) CdTe mass concentration is indicated on each spectrum (b) Integrated photocurrent density of the alloyed films versus CdTe mass concentration

98

CHAPTER 5

RESULTS and DISCUSSION

BAND GAP TUNING of MoO$_3$ THIN FILMS THROUGH ALLOYING with CdTe

5.1 Structural analysis

Thermally-evaporated MoO$_3$ thin film and films alloyed with 2%, 4%, 6%, 8% and 10% had an amorphous nature as revealed by XRD study. The absence of the CdTe crystalline peaks in these films compared to WO$_3$/CdTe films fabricated at high CdTe concentrations may be attributed to the low concentrations of CdTe which may be below the detection limit of XRD.

5.2 Morphological analysis

Figure 5.1a shows a three dimensional AFM micrograph of an MoO$_3$ thin film. It can be observed that the film had a columnar structure. However, in the film mixed with 2% of CdTe, some of the columnar growth was transformed into granular growth as shown in Fig.5.1b. The granular growth increased significantly with the increase of CdTe concentration into 4% and 6%, as depicted in Fig. 5.1c and Fig.5.1d, respectively. Further increase in CdTe concentration to 8% and 10% led to the formation of a dense granular structure, as shown in in Fig. 5.1e and Fig.5.1f, respectively. The surface roughness of the investigated films was characterized by root mean square roughness (R_{rms}) obtained

from the AFM micrographs. The R_{rms} values of the fabricated films were found to be slightly increased with CdTe as displayed in Fig. 5.2. The observed increase in the R_{rms} may be due to improper agglomeration of crystallites [172].
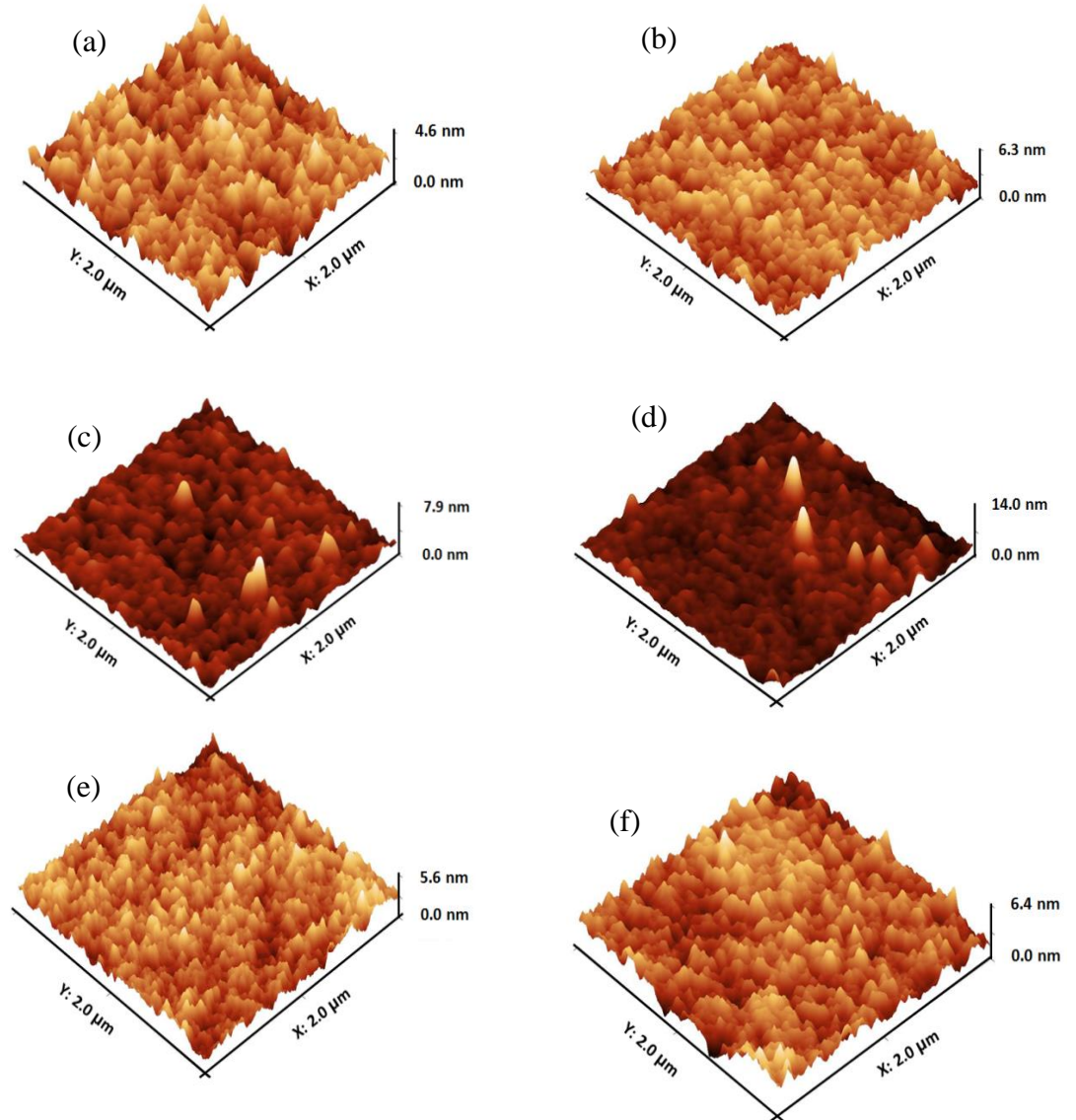
Fig. 5.1 Three dimensional AFM images of thermally evaporated MoO$_3$ film (a), and MoO$_3$ films alloyed with mass concentrations of 2% (b), 4% (c), 6% (d) 8%, (e) and 10% (f).
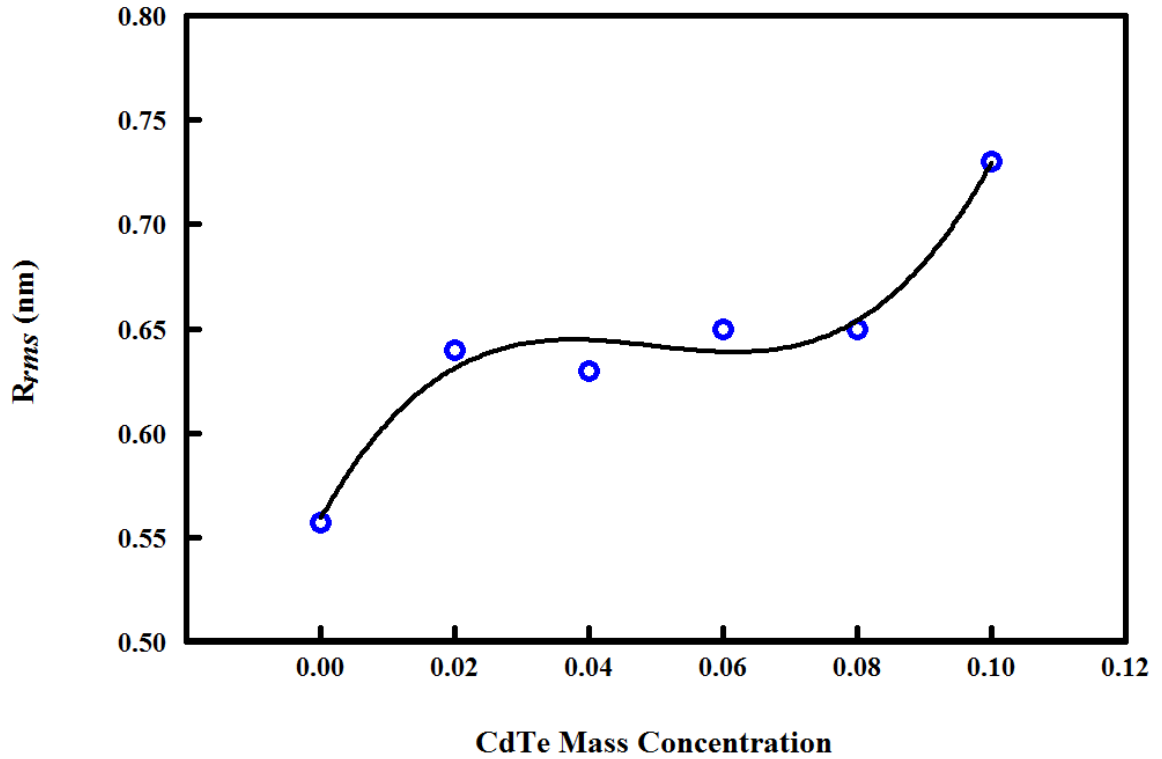
Fig. 5.2 Variation of R_{rms} of MoO_3 thin films with CdTe mass concentration.

5.3 Optical properties

5.3.1 Transmittance measurements

The transmittance spectrum of a pure MoO_3 thin film is displayed in Fig. 5.3a. The film has maximum transparency in the visible region down to a wavelength of 400 nm. A sharp absorption edge can be observed below 400 nm. The absorption edge of MoO_3 was shifted toward longer wavelengths by alloying with different concentrations of CdTe, as shown in Figs. 5.3b-5.3f. In this case, less CdTe concentrations were used with MoO_3

compared to that with WO_3 to avoid the deterioration of the optical properties (i.e. the significant decrease of transmittance at higher CdTe concentrations) of MoO_3 thin films. Furthermore, it is evident that the CdTe alloyed films demonstrated lower transmittance compared to the pure MoO_3 film. The same considerations concerning the lower optical transparency of WO_3 films due to mixing with CdTe are applicable here, in that the transparency of CdTe alloyed MoO_3 films is dominated by the absorption of these films. As the CdTe content increased, the absorption increased leading to lower transmittance, and the films became non-transparent at higher CdTe concentrations. This enhancement in the absorption is due to mixing with CdTe which is a good absorber for light.
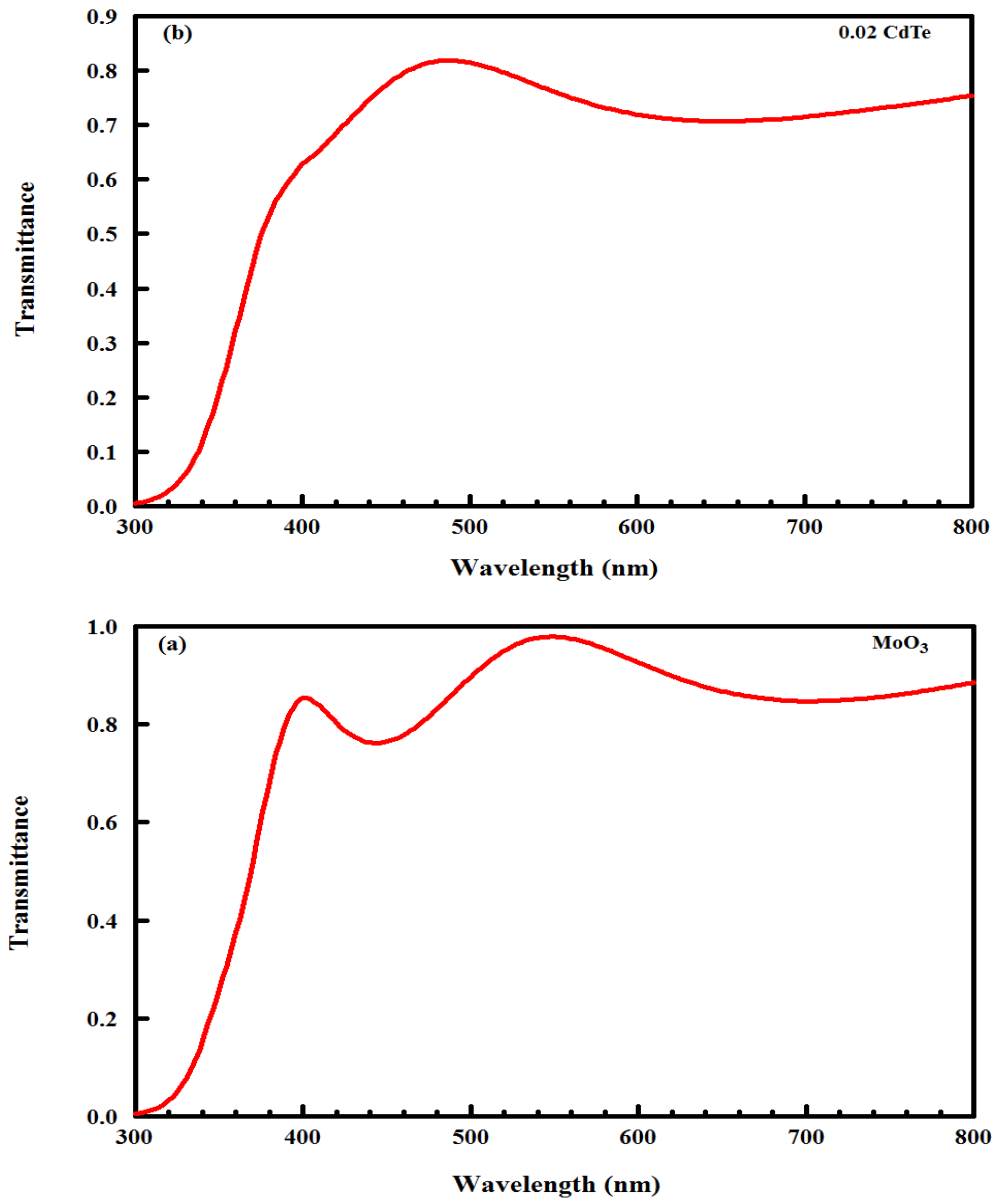
Fig. 5.3 Transmittance spectra of thermally-evaporated pure MoO₃ thin film (a) and MoO₃ thin film alloyed with CdTe mass concentrations of 2% (b), 4% (c), 6% (d), 8% (e) and 10% (f).

Fig. 5.3 Continued.

Fig. 5.3 Continued.

5.3.2 Thickness measurements of the films

The thickness of the pure MoO_3 film and CdTe-alloyed films was estimated following the same method described in section 4.3.2. Based on the interference maxima and minima of the transmittance spectra, the thickness of each film was calculated using Eq. 4.1. Figure 5.4 demonstrates representative interference maxima and minima of the transmittance spectrum of a pure MoO_3 thin film in the wavelength range 200-1400 nm, which was used for the estimation of the film thickness. The thickness of all films was found to be 270 ± 20 nm.
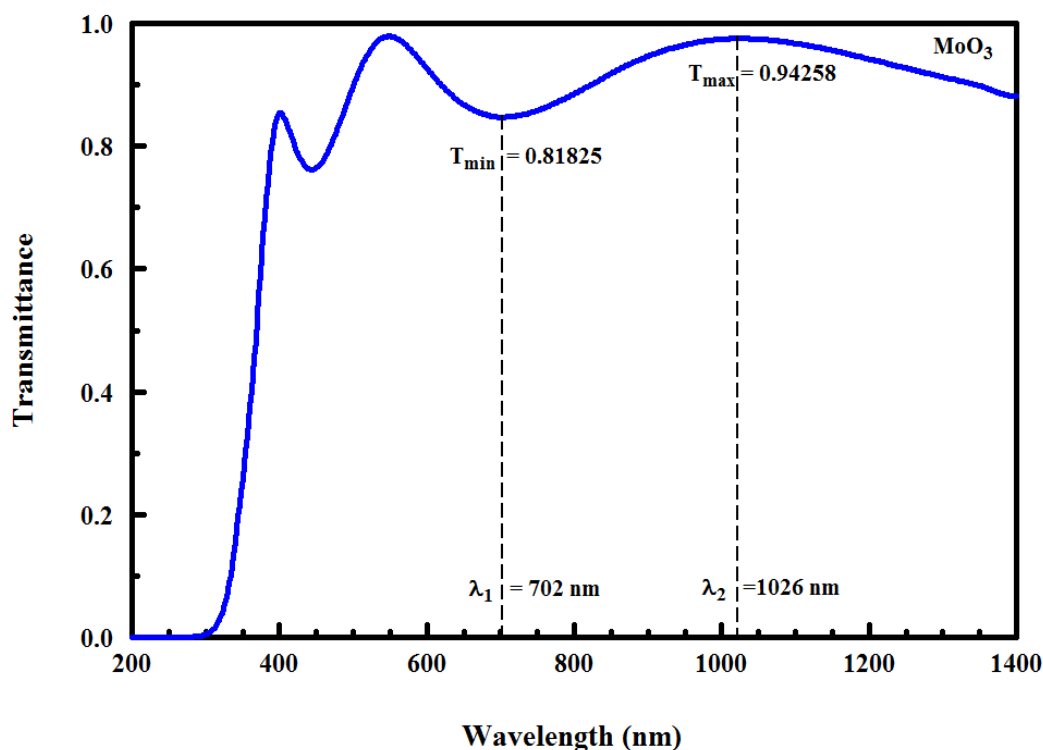
Fig. 5.4 Transmittance spectrum of a pure MoO_3 thin film in the wavelength range 200-1400 nm A maximum and an adjacent minimum and their corresponding wavelengths are depicted.

5.3.3 Absorption coefficient

The absorption coefficients of MoO_3 and CdTe-alloyed MoO_3 films were estimated following the same method described in section 4.3.3. Plots of the absorption coefficients of all films versus the wavelength are depicted in Fig. 5.5. It can be noted that the absorption edge of the pure MoO_3 film was located below 400 nm. This absorption edge was shifted up toward longer wavelengths (red-shift) with the increase of CdTe content, which coincides with the previous observation in the transmittance spectra of the films. In addition, it can be seen from the figure that the absorption coefficient of pure MoO_3 thin film increased gradually from 3.75×10^5 cm^{-1}in the UV region with the increase of CdTe content to reach three times of this value at a CdTe content of 10%. Since the absorption coefficient was greater than 10^5 cm^{-1} over the entire visible region, the alloyed films are able to absorb over 90% of the day light [125,126]. The physical interpretation considered with the results obtained from alloying of WO_3 film with CdTe could be applicable here, in that the enhancement of absorption of MoO_3 thin film is ascribed to the alloying with CdTe material which is a good absorber for light. The obtained results make our new designed films candidate for light energy harvesting and photovoltaic applications over larger portions of the visible spectrum.
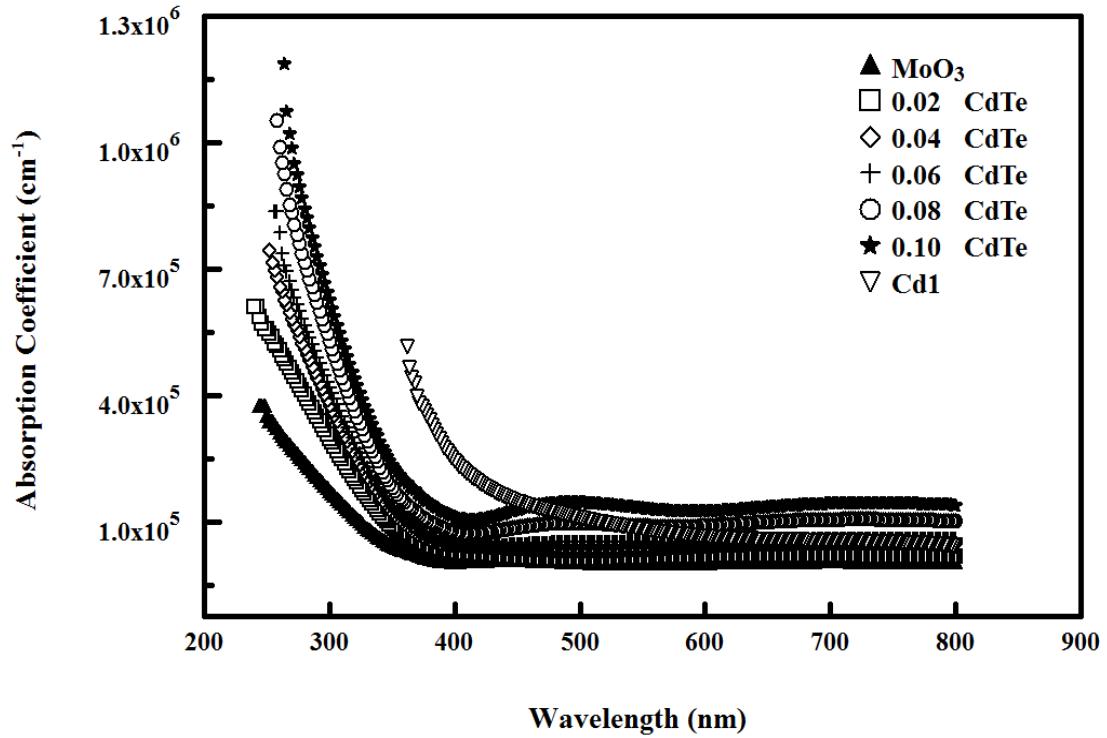
Fig. 5.5 The absorption coefficients of pure MoO₃, CdTe and CdTe-alloyed MoO₃ thin films as a function of the wavelength.

5.3.4 Determination of the optical band gap

The values of the indirect band gap, (E_g) of the films were obtained using the Tauc relation, Eq. 4.4. The plot of $(\alpha E)^{1/2}$ as a function of photon energy for the fabricated MoO₃ films is shown in Fig. 5.6a. The band gap was found to be 2.90 eV, which agrees with the previous reported values [173,174]. Figures 5.6b-5.6f demonstrate the graphs of $(\alpha E)^{1/2}$ as a function of photon energy for CdTe-alloyed MoO₃ films. The band gap values were 2.85, 2.75, 2.70, 2.65 and 2.60 eV at CdTe concentrations of 2%, 4%, 6%,

8% and 10%, respectively. It is clear that the band gap of the MoO_3 film was red-shifted with the increase of CdTe concentration.

Similar to the trend of the band gap values of WO_3/CdTe thin films, the band gap values of MoO_3/CdTe thin films obey the bowing Eq. 2.21. Thus, the method of fitting the band gap values of WO_3/CdTe thin films are applicable to those of MoO_3/CdTe thin films in that the dependence of band gap of the alloyed MoO_3 films on the CdTe content may be fitted using the quadratic bowing Eq. 4.5. However, in this case, a is given by $a = E_T - E_M - b$, where E_M is the band gap of pure MoO_3, and $E_g(0) = E_M$. Least-squares fitting of Eq. 4.5 to the experimental data presented in Fig. 5.6 is shown in Fig. 5.7, where the best fit values of the parameters a and b were -3.25 and 1.75eV, respectively. Furthermore, it is clear that the experimental variation of the band gap values with CdTe is described by the standard bowing quadratic equation for the whole range of CdTe concentration. The systematic red shift of the band gap of the $(MoO_3)_{1-x}$/$(CdTe)_x$ films from 2.90 eV at 0% CdTe to 2.60 eV at a maximum CdTe content of 10% reveals that the band gap of MoO_3 was engineered to cover a wide part of the visible region of the solar spectrum. Hence, we end up with similar results to those obtained by engineering the band gap of WO_3 films in that light harvesting may be extended over larger portion of the visible spectrum region.
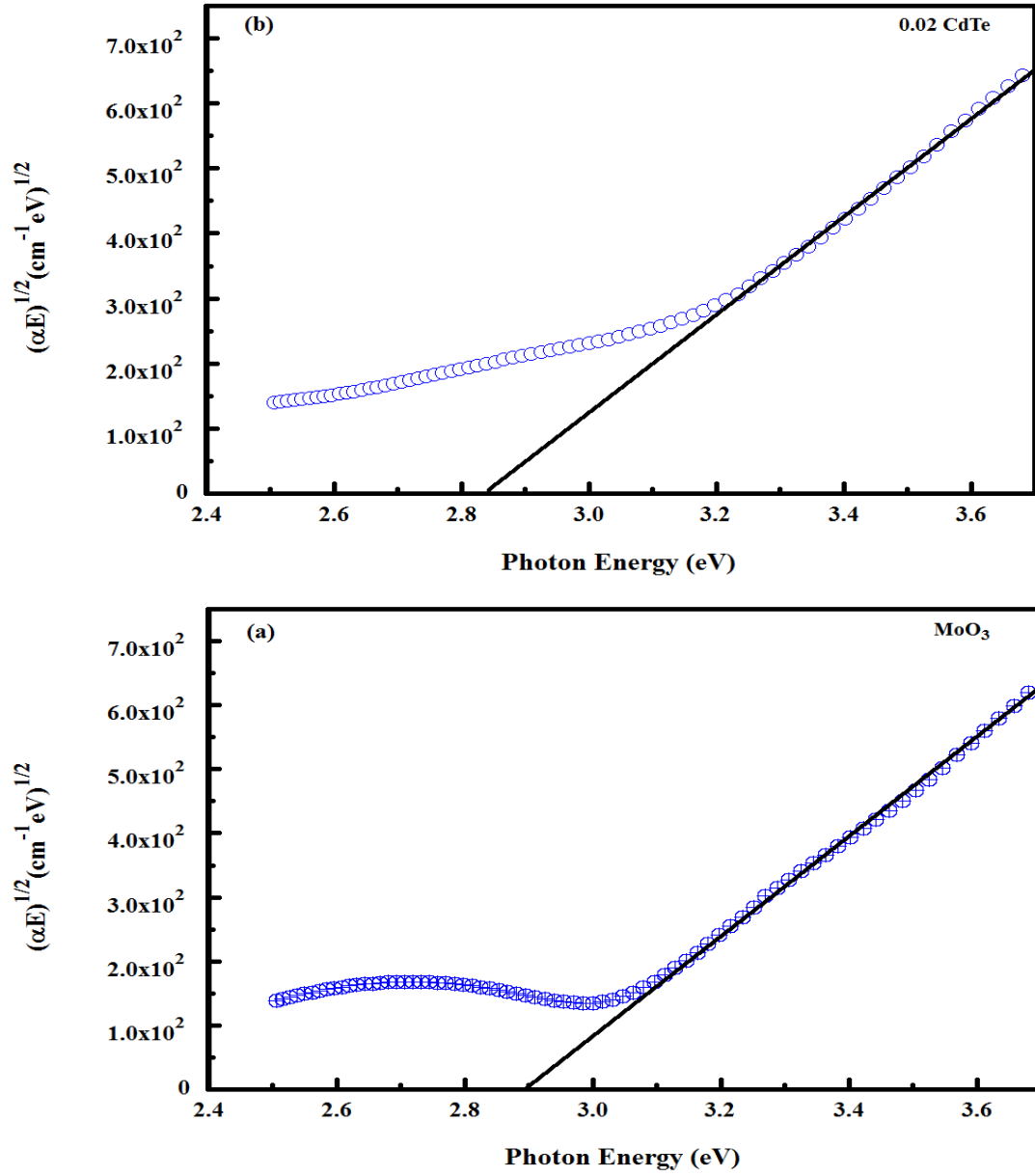
Fig. 5.6 Tauc plot of (αE) $^{1/2}$ as a function of photon energy for determining the band gap of MoO$_3$ thin film (a) and MoO$_3$ thin film alloyed with CdTe mass concentrations of 2% (b) , 4% (c), 6% (d), 8% (e) and 10% (f).
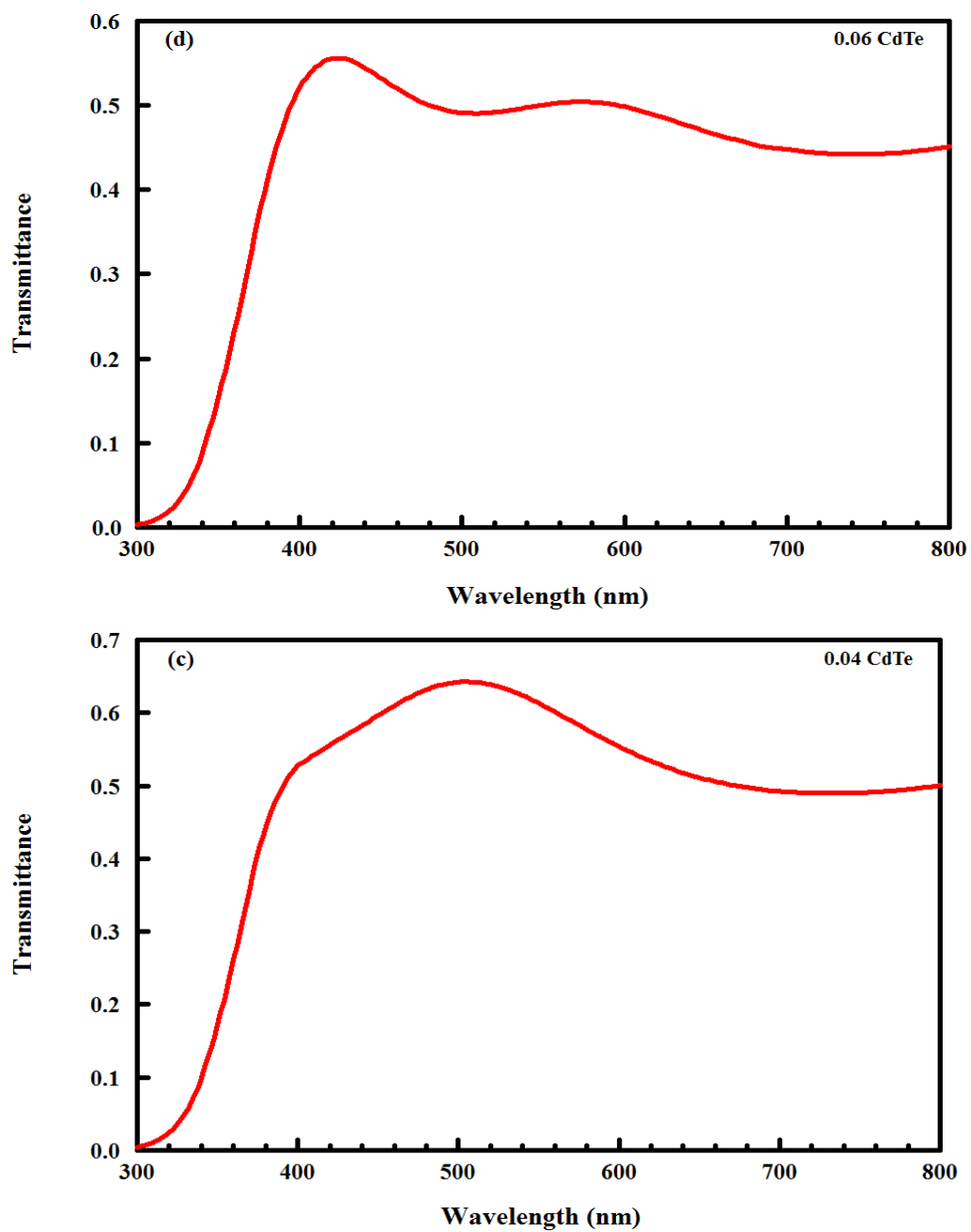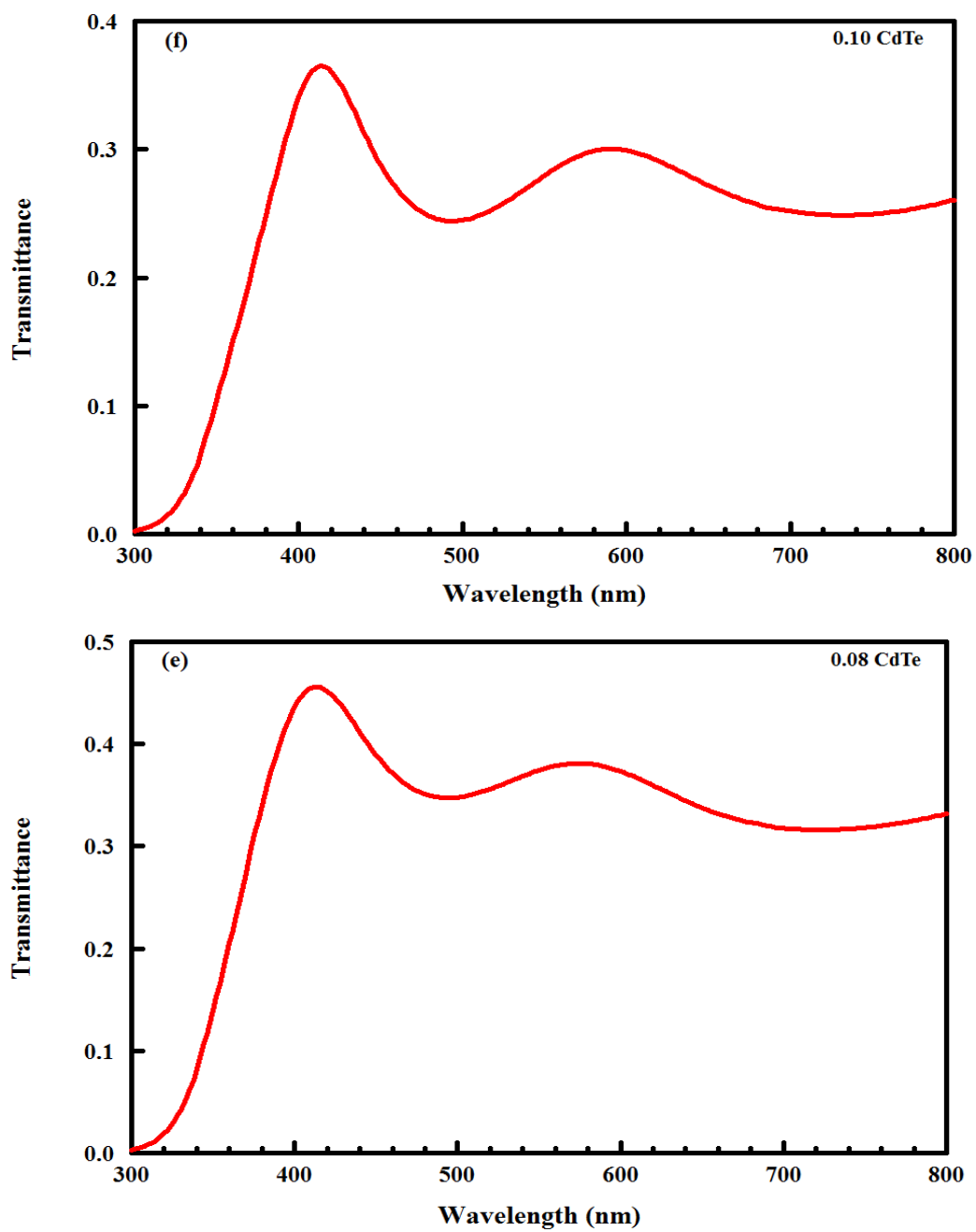
Fig. 5.6 Continued.

111

Fig. 5.6 Continued

112
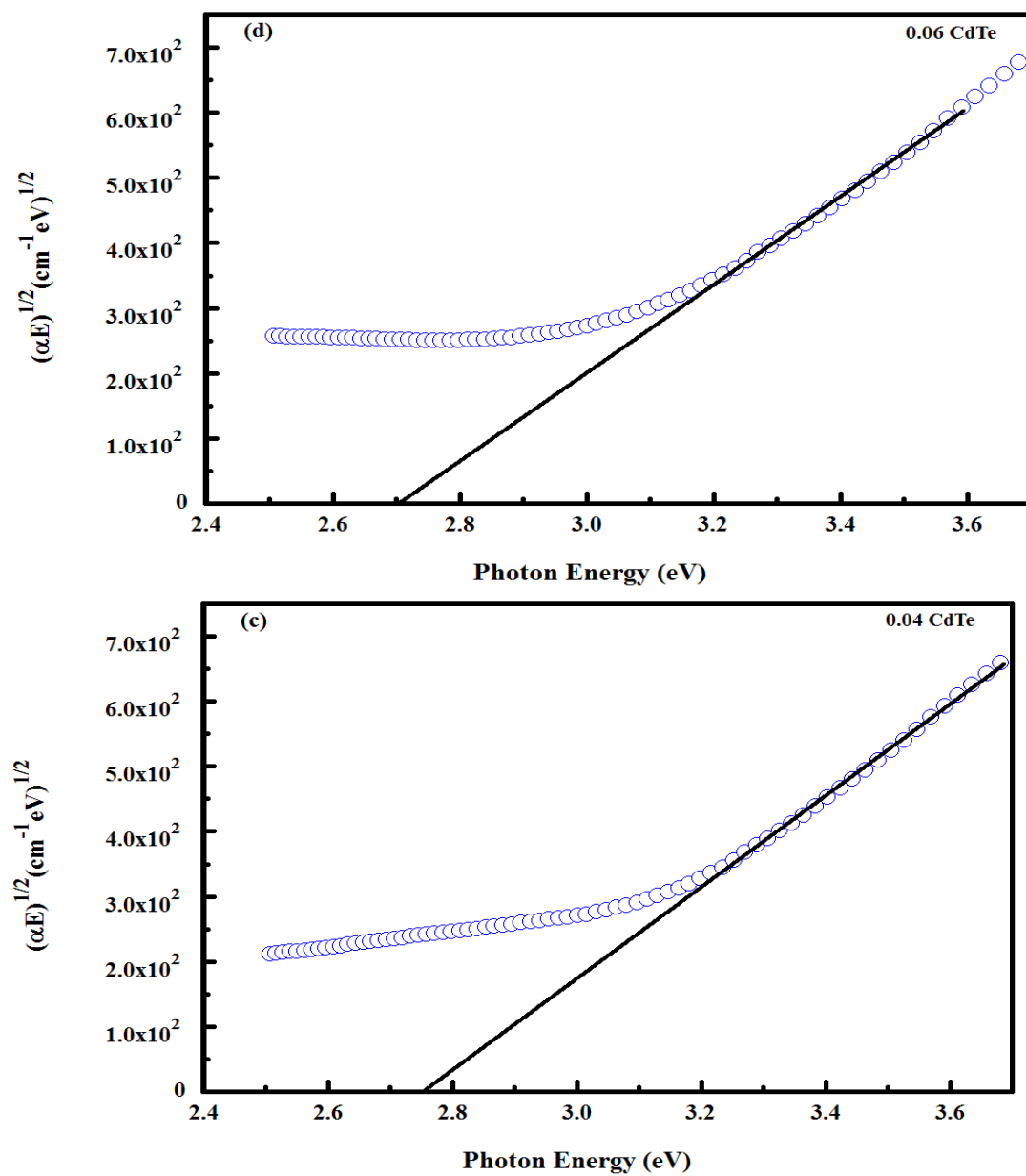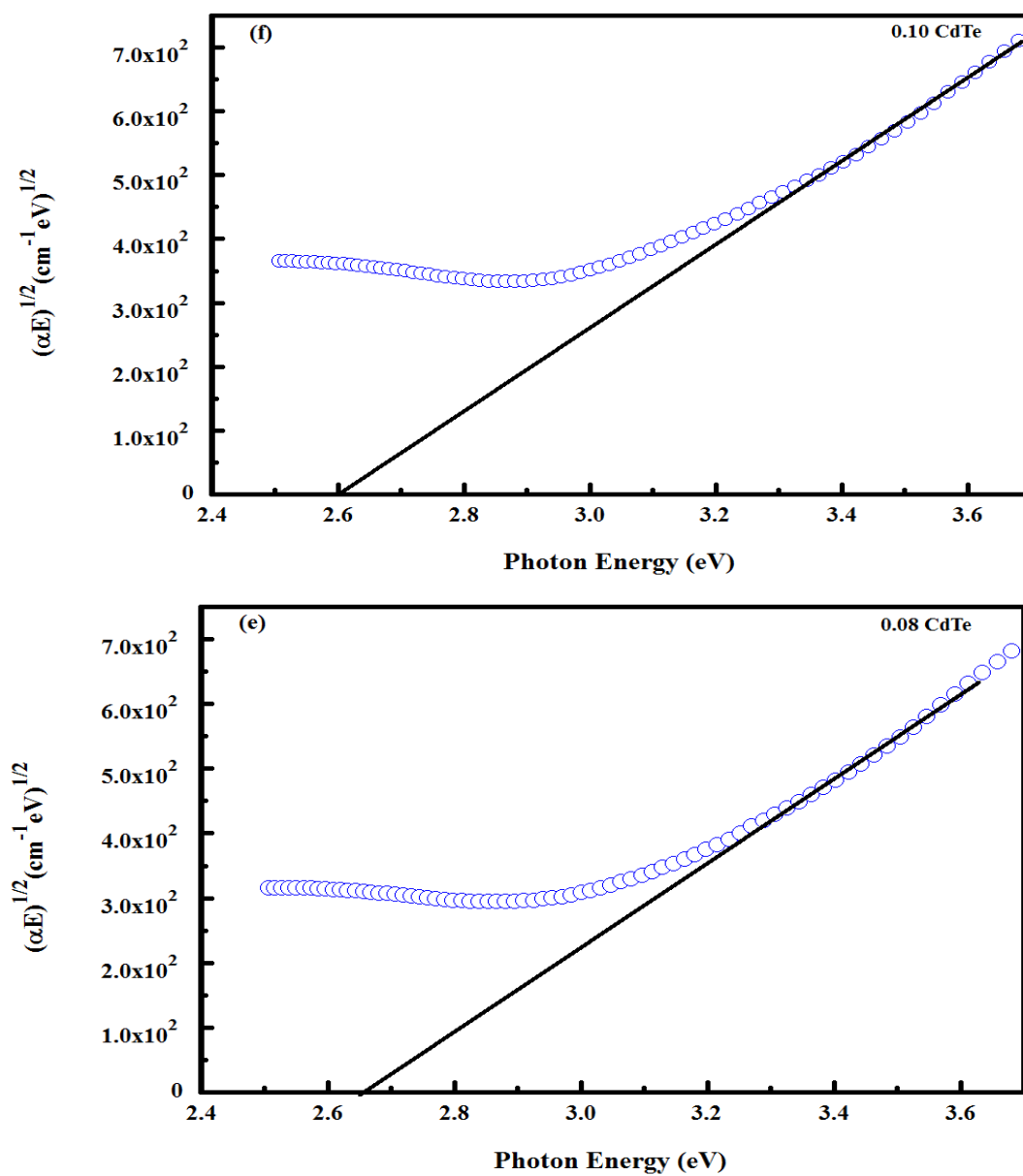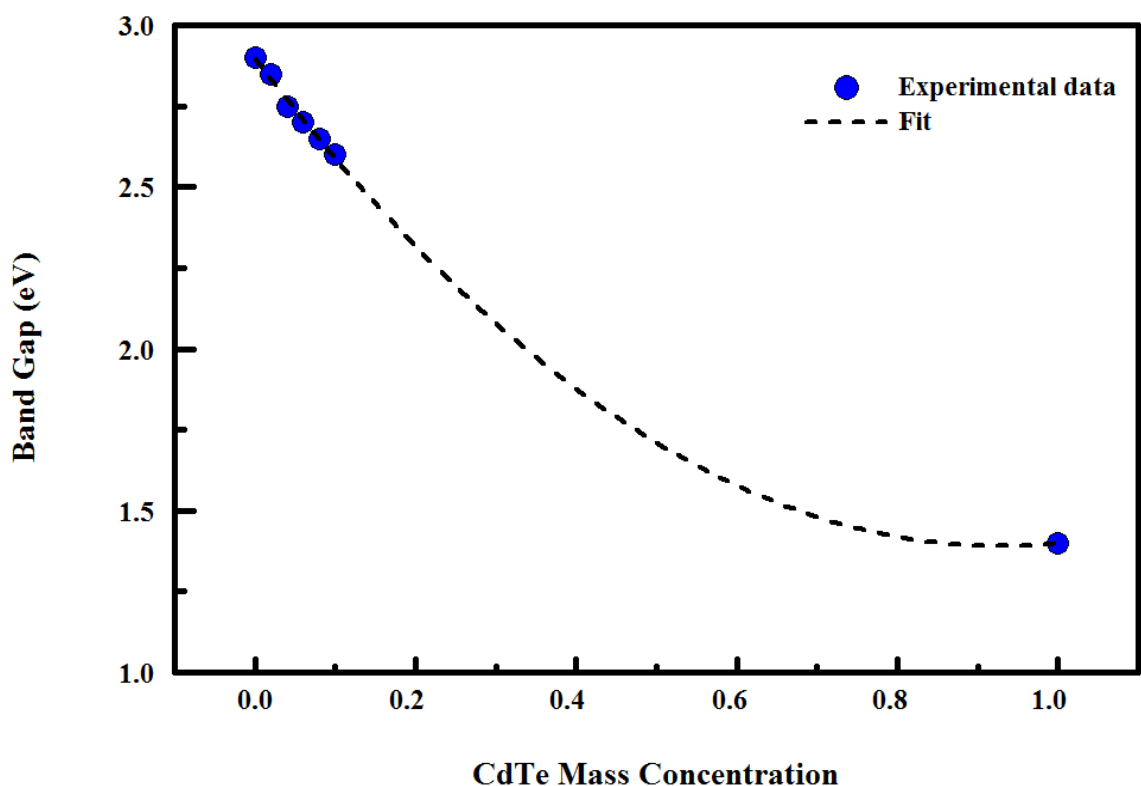
Fig. 5.7 Variation of the band gap of CdTe-alloyed MoO₃ thin films with CdTe mass concentration.

5.4 Chemical analysis

5.4.1 XPS analysis of MoO₃

The chemical composition of the fabricated MoO_3 thin film was investigated by XPS. The XPS survey spectrum for the film is shown in Fig. 5.8. As can be seen, the film contains only the main elements; Mo and O. The scan for Mo 3d core level (Fig. 5.9a.) reveals that Mo 3d level is splitted into two peaks (Mo $3d_{5/2}$ and Mo $3d_{3/2}$) centered at binding energies of 232.7 and 235.9 eV, respectively, and are attributable to MoO_3 [175-

179]. The intensity ratio of Mo $3d_{5/2}$ peak to Mo $3d_{3/2}$ peak is 1.5 and the spin-orbit splitting is 3.2 eV, which are in good agreement with the reported values [177,178, 180-182]. The existence of different oxidation states in the film was investigated by fitting the Mo 3d spectrum, as depicted in Fig. 5.9b. The fitting showed that Mo 3d spectrum was deconvoluted into two pairs of Mo $3d_{5/2}$ and Mo $3d_{3/2}$ peaks. Two peaks positioned at high binding energies of 232.8 eV and 235.8 eV were assigned to stoichiometric MoO_3 (Mo^{6+}), and two small peaks located at low binding energies of 231.5 eV and 234.5 eV were assigned to sub-stoichiometric $MoO_{2.5}$ (Mo^{5+}) [176,179, 183,184]. The decomposition results (Table 5.1) show that the amount of Mo^{5+} in the film was only 4% of the total Mo 3d peak, indicating that the film is predominantly in the Mo^{6+} oxidation state, i.e stoichiometric. Similarly, the O 1s core level spectrum was deconvoluted into two components centered at a lower binding energy of 530.7 eV and a higher binding energy of 531.8 Ev, as presented in Fig. 5.10. The lower binding energy component is attributable to oxygen bonded to molybdenum (Mo-O) while the higher binding energy component is ascribed to OH groups or adsorbed oxygen on the film surface [175,182, 185,186]. The ratio of the OH to the total O 1s peak was only 6%. The O/Mo ratio was calculated from Eq. 4.6, with replacing the statistical weight of W^{6+} and W^{5+} by those of Mo^{6+}, Mo^{5+}, respectively.
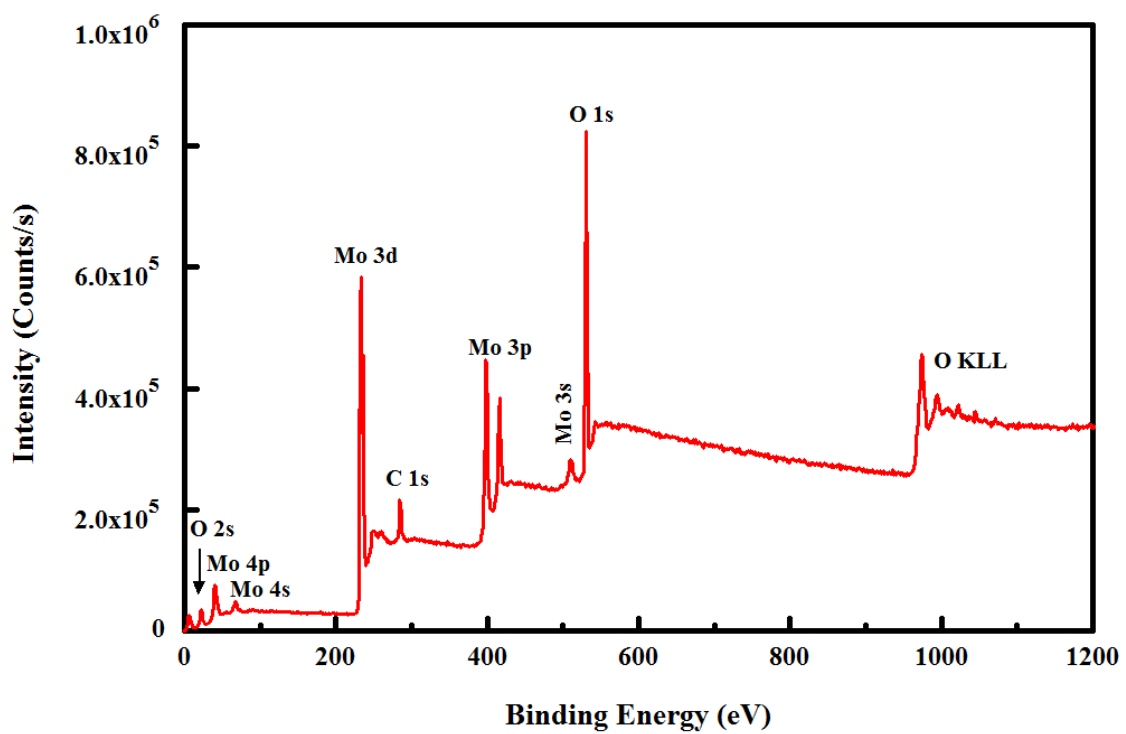
Fig. 5.8 XPS survey spectrum of the MoO$_3$ thin film.
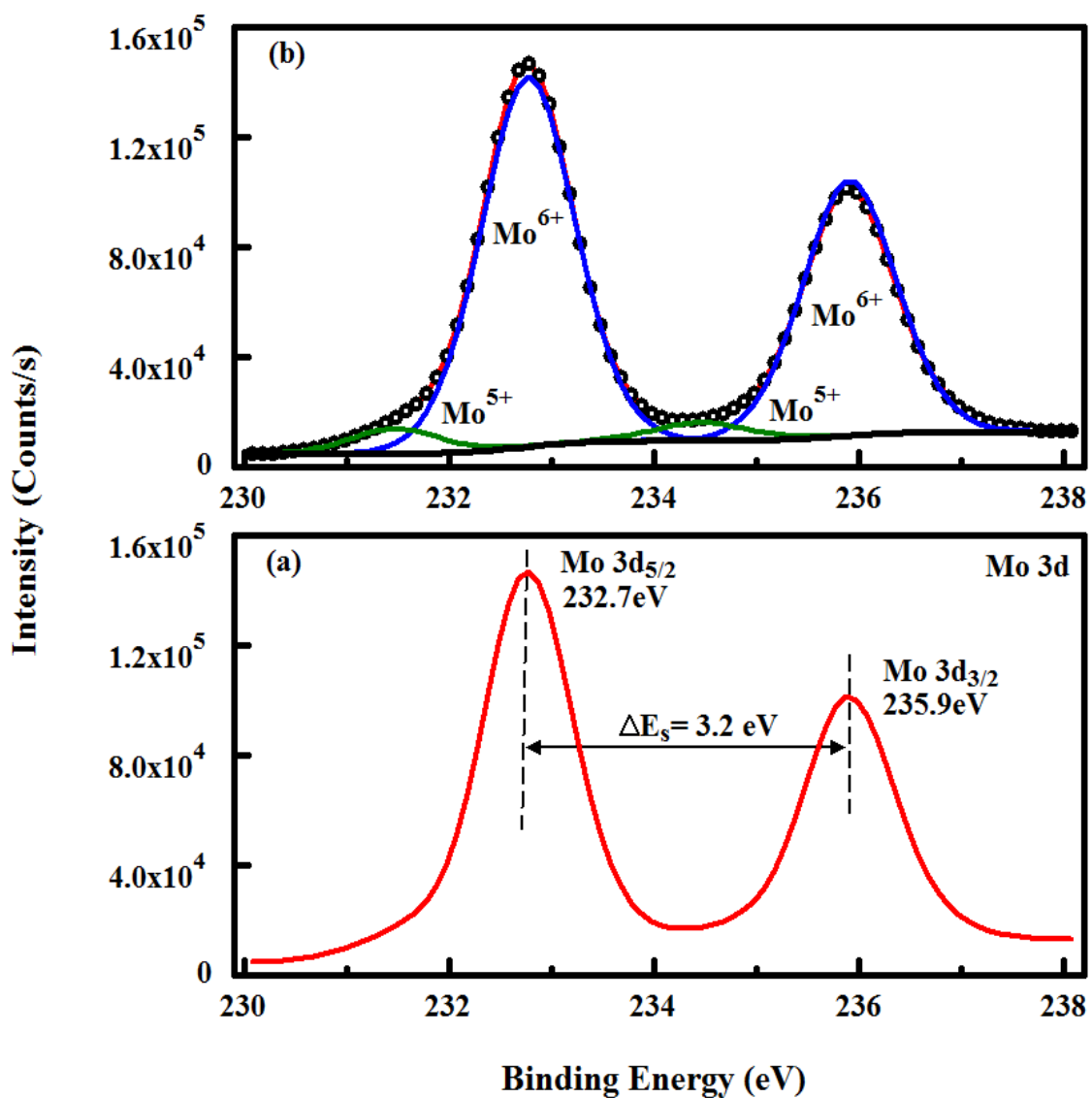
Fig. 5.9 (a) XPS spectrum in the Mo 3d core level region, showing the two doublets assigned to Mo 3d$_{5/2}$ and Mo 3d$_{3/2}$ of MoO$_3$ (b) Deconvolution of Mo 3d$_{5/2}$ and Mo 3d$_{3/2}$ peaks into Mo^{6+} and Mo^{5+} oxidation states.
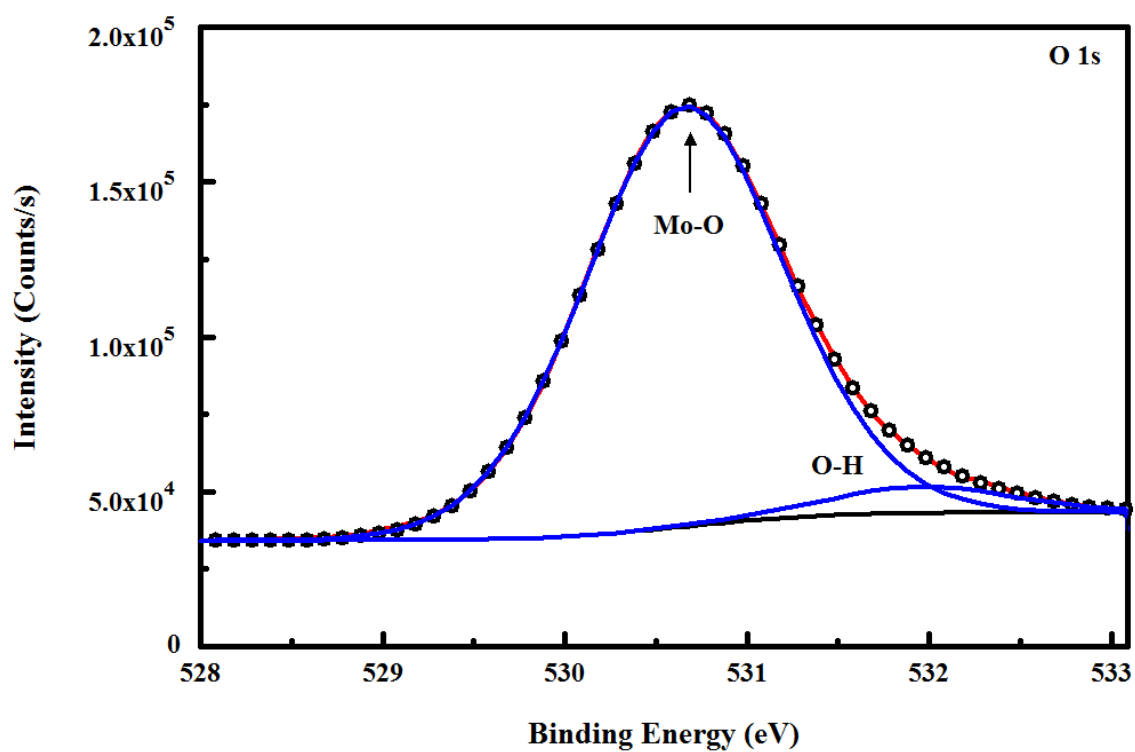
Fig. 5.10 Deconvolution of O 1s core level spectrum into two components in MoO$_3$ thin film.

Table 5.1: Deconvolution results of Mo 3d spectrum of MoO$_3$ thin film with corresponding binding energies (BE), statistical weight, and full-width at half maximum (FWHM) of each component Ratio of sub-stoichiometric oxide (Mo^{5+}) to the total Mo and ratio of oxygen to Mo in the film are also calculated and listed.

Component	Peak BE (eV)	FWHM (eV)	Area (CPS)	Statistical weight	Mo^{5+}/Mo	$R_{O/Mo}$
Mo^{6+} 3d$_{5/2}$	232.8	1.08	156670.03	96.25		
Mo^{6+} 3d$_{5/2}$	231.5	1.06	10323.11	3.75		
Mo^{5+} 3d$_{3/2}$	235.8	1.08	108163.65	-	0.04	2.98
Mo^{5+} 3d$_{3/2}$	234.5	1.1	7780.34	-		

5.4.2 *XPS depth profiling of MoO₃/CdTe*

The compositional depth profiles of the MoO_3/CdTe thin films were obtained by a sequential Ar^+ ion etching followed by XPS analysis. Each film was completely etched after 15 cycles with an etching period of 60 s for each cycle. The other parameters of XPS depth profile runs were the same as those fixed during performing depth profiling of WO_3/CdTe thin films. Figs. 5.11 shows typical representative XPS depth profile spectra of MoO_3 thin film alloyed with 6% CdTe. The discussion concerning the WO_3/CdTe thin films are applicable to the MoO_3/CdTe thin films in that the oxidation states were not investigated due to the shift in binding energy peak positions caused by Ar^+ ion sputtering as can be seen clearly in Figs. 5.11a-c, as well as the total disappearance of C1s peak reference after the first cycle of etching as shown in Fig. 5.11e. In order to investigate the variation of the constituents in each film, the XPS signal intensity was plotted versus the etching time. XPS depth profiling of MoO_3/CdTe thin films fabricated at CdTe concentrations of 2%, 4%, 6%, 8% and 10% are depicted in Figs. 5.12-5.16, respectively. Fig. 5.12 shows the depth profile of MoO_3/CdTe thin film fabricated at CdTe concentration of 2%, where both Te and Cd evolved gradually (Fig. 5.12a) starting from the early stages of evaporation at an etching time of 840 s and continued in growth smoothly throughout the film thickness until etching time of 60 s. Then, one can observe a significant increase in the content of Cd accompanied by a decrease in the intensity of Te until reaching the upper side of the film. As mentioned before in the discussion of the depth profiling of WO_3/CdTe thin films, such non-stoichiometry is explained by the formation of oxide layers. On other hand, it can also be seen that Mo and O evolved

119

smoothly (Fig. 5.12b) and in parallel with Cd and Te from the bottom side of the film at an etching time of 840 s until an etching time of 600 s followed by a remarkable increase in the intensity of O and slight decrease in the intensity Mo, then a stable behavior of distribution can be observed along with the decreasing of etching time until reaching the upper side of the film. Obviously, the late stages of etching show that the exposed surfaces of the lower layers are rich in Mo metal. A similar result was previously reported by Driscoll *et al.* [162] in thermally evaporated MoO_3 film with the co-presence of different oxidation states of MoO_3 film, specifically MoO_x and MoO_2 in addition to the primary MoO_3. The discussion concerning the depth profiling of $WO_3/CdTe$ thin films is applicable to depth profiling of $MoO_3/CdTe$ thin films in that the metal-enriched layers were explained by the increase in the amorphization of the film due to the initial etching and the variation of oxidation states was caused by sputtering. The presence of different oxidation states in the alloyed films is evident from the decrease in the intensities of O components along with etching which indicates that the stoichiometry of MoO_3 is no longer preserved and sub-stoichiometric oxides (MoO_x) were formed [162]. It is also noticed that contrary to consuming of Te and Cd components at the middle layers of $WO_3/CdTe$ thin films, smooth and continuous growth of these two components in parallel with Mo and O components until reaching the topmost side of the film can be observed. This observation may be attributed to the low energy of evaporation determined by the melting point of MoO_3 (795 ^{o}C).

When the CdTe content was increased to 4% (Fig. 5.13), both Cd and Te were evolved with leveled off signals throughout the film thickness as shown in Fig. 5.13a,

starting from the bottom side corresponding to an etching time of 840 s toward the top side of the film until reaching the upper level of the film specifically at an etching time of 300 s. Then, the Cd signal increased remarkably as the etching time decreased to 240 s and then leveled off until reaching the upper side of the film. On the contrary to the increase in the Cd signal, the Te signal was decreased and then leveled off until reaching the upper side of the film. The remarked increase in the Cd signal compared to that of Te indicates that the sample is rich in Cd due to the formation of oxide layer as discussed previously. Regarding the distribution of Mo and O in this sample, Fig. 5.13b shows a stable behavior for distribution of both components starting from the bottom side towards the top side of the film with decreasing the etching time to 360 s. Then, a sharp increase in the O signal accompanied by slight decrease in Mo signal were observed at the upper layer of the film corresponding to the etching time of 300 s followed by a stable level of distribution until reaching the side of the film. Moreover, one can observe that most of the exposed surfaces of this sample are rich in Mo metal. At a CdTe concentration of 6%, the distribution of Cd and Te elements in the film showed similar trend as that observed in the film prepared at CdTe concentration of 2%, as depicted in Fig. 5.14a. However, more exposed layers were rich in Te at the late stages of etching and a slight increase in the Te signal at the middle layers of the film compared to the sample prepared at CdTe concentration of 2%. Likewise, the depth distribution of Mo and O (Fig. 5.14b) was similar to that noted in the film prepared at Cd concentration of 2% with the slight increase of the exposed surfaces enriched with Mo at the late stages of etching. In case of increasing the content of CdTe into 8% (Fig. 5.15), the variation of depth distribution of the constituents in the film; Cd, Te, Mo and O showed behavior like that observed in the

film fabricated at CdTe content of 4%, where the film was rich in Cd throughout the depth of the film compared to Te and the exposed surfaces of the film at the late stages of etching are rich and Mo compared to O. However, a slight increase in the Te signal can be observed at the layer corresponding to the etching time of 300 s opposite to that observed in the film fabricated at CdTe content of 4%. Finally, further increase in the CdTe content into 10% (Fig. 5.16) resulted in a slight enrichment of Te element on the exposed layers of the film at the late stages of etching with remarked increase at the middle layer compared to that observed in the film prepared at CdTe concentration of 6%. Then, the signal of Te decreased gradually with decreasing of the etching time, showing similar behavior observed previously in the film prepared at CdTe concentration of 6% until an etching time of 360 s, then leveled off until reaching the topmost of the film. Regarding the distribution of the other components (Cd, Mo and O), it can be observed that they were roughly distributed throughout the film thickness by the exact mechanism of distribution observed in the sample prepared at CdTe concentration of 6%. As a result, it can be concluded that the XPS depth profiling demonstrated that the constituent elements were uniformly distributed along the depth of the alloyed films.
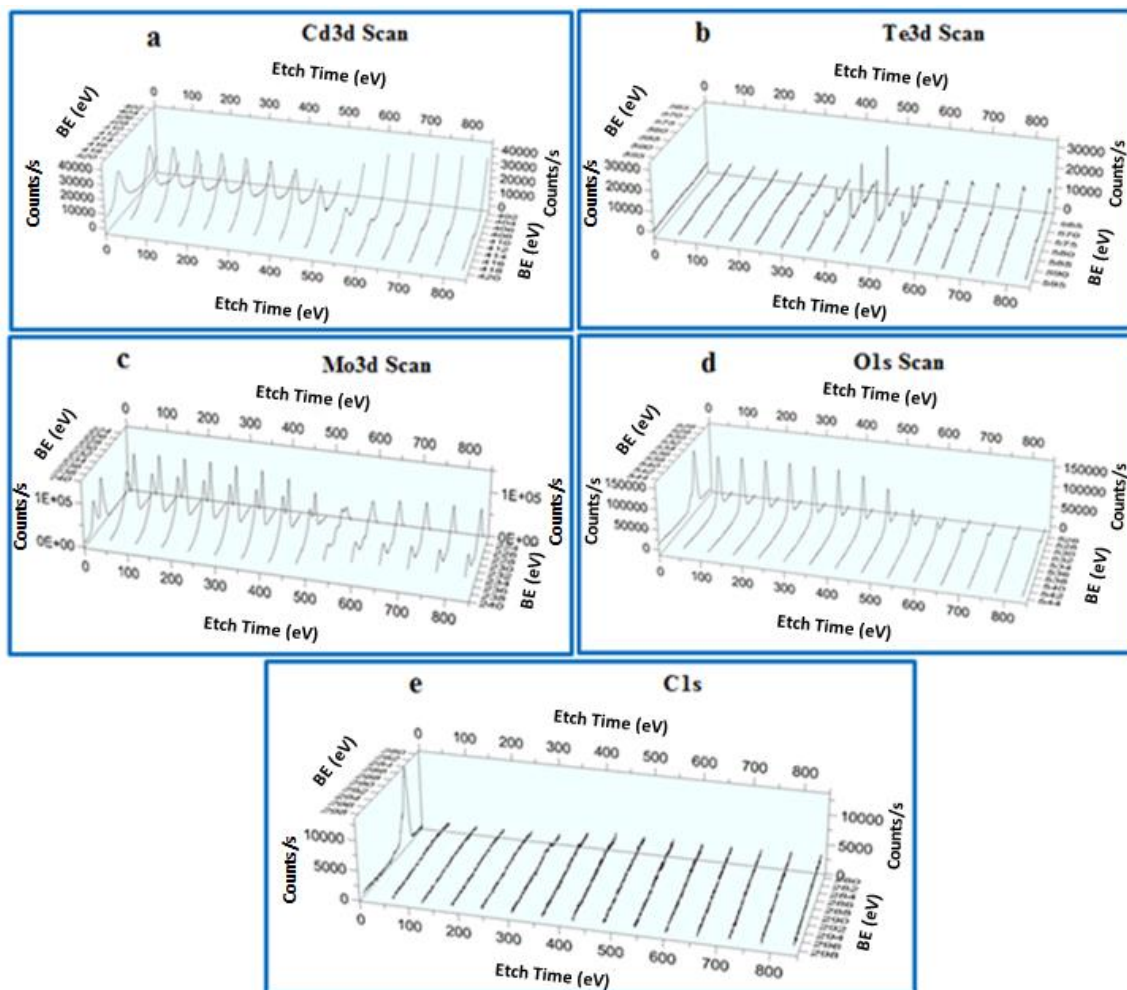
Fig. 5.11 XPS depth profile scan of (a) Cd 3d, (b) Te 3d, (c) Mo 3d, (d) O 1s and (e) C 1s regions in the MoO₃ thin film alloyed with 6% CdTe.
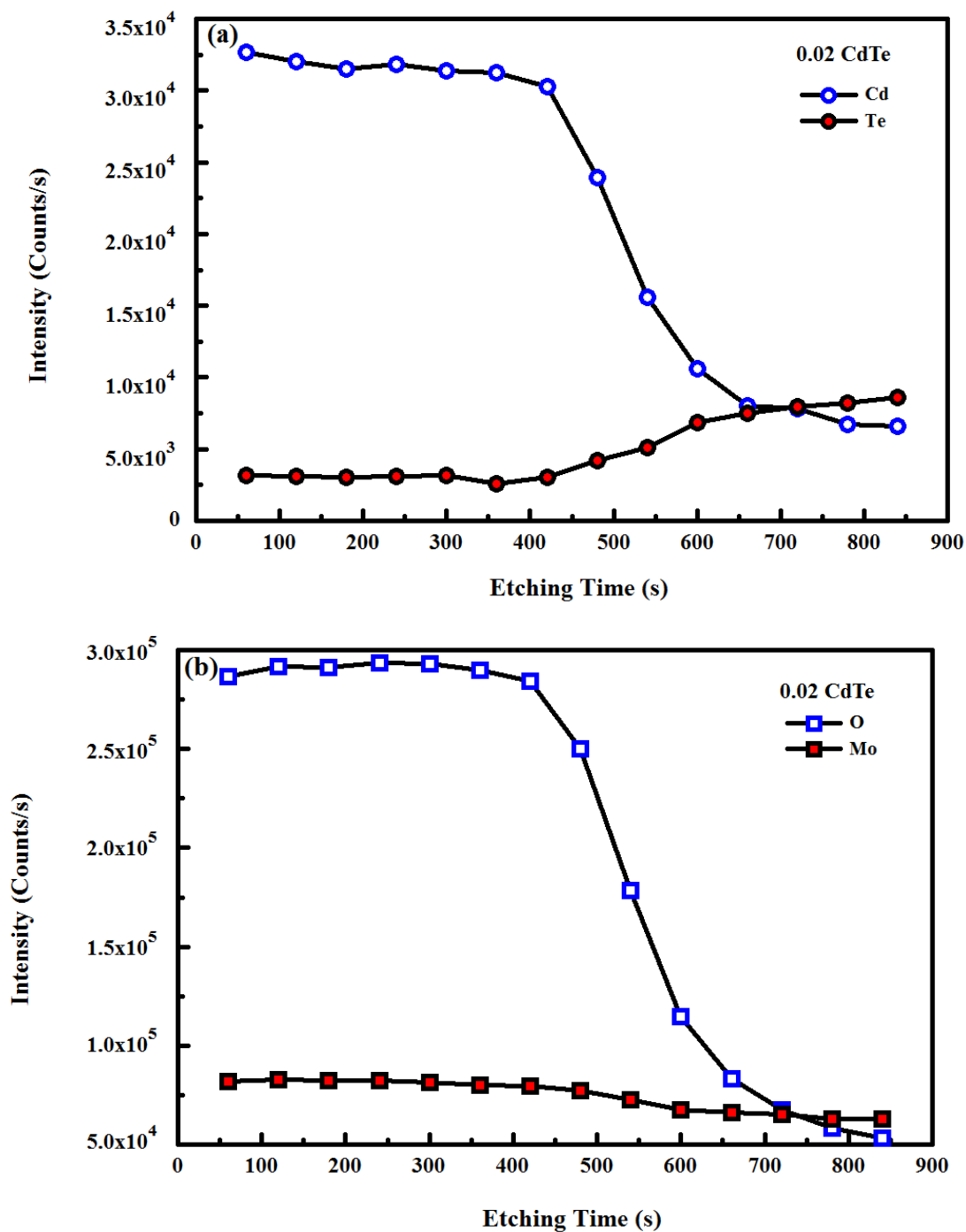
Fig. 5.12 XPS signal intensity versus etching time for MoO$_3$ thin film alloyed with 2% CdTe, (a) Cd and Te components, (b) Mo and O components.
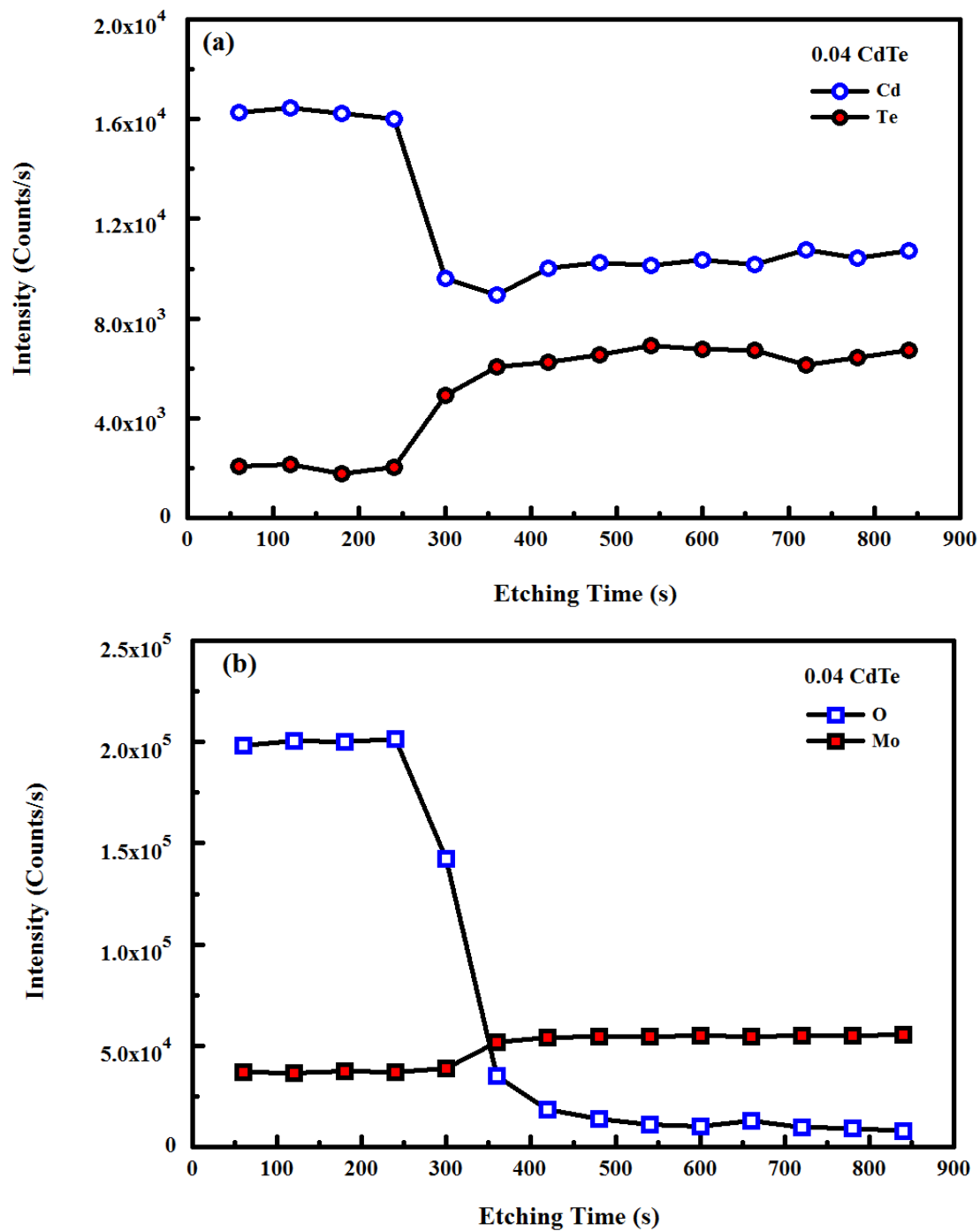
Fig. 5.13 XPS signal intensity versus etching time for MoO$_3$ thin film alloyed with 4% CdTe, (a) Cd and Te components, (b) Mo and O components.

125
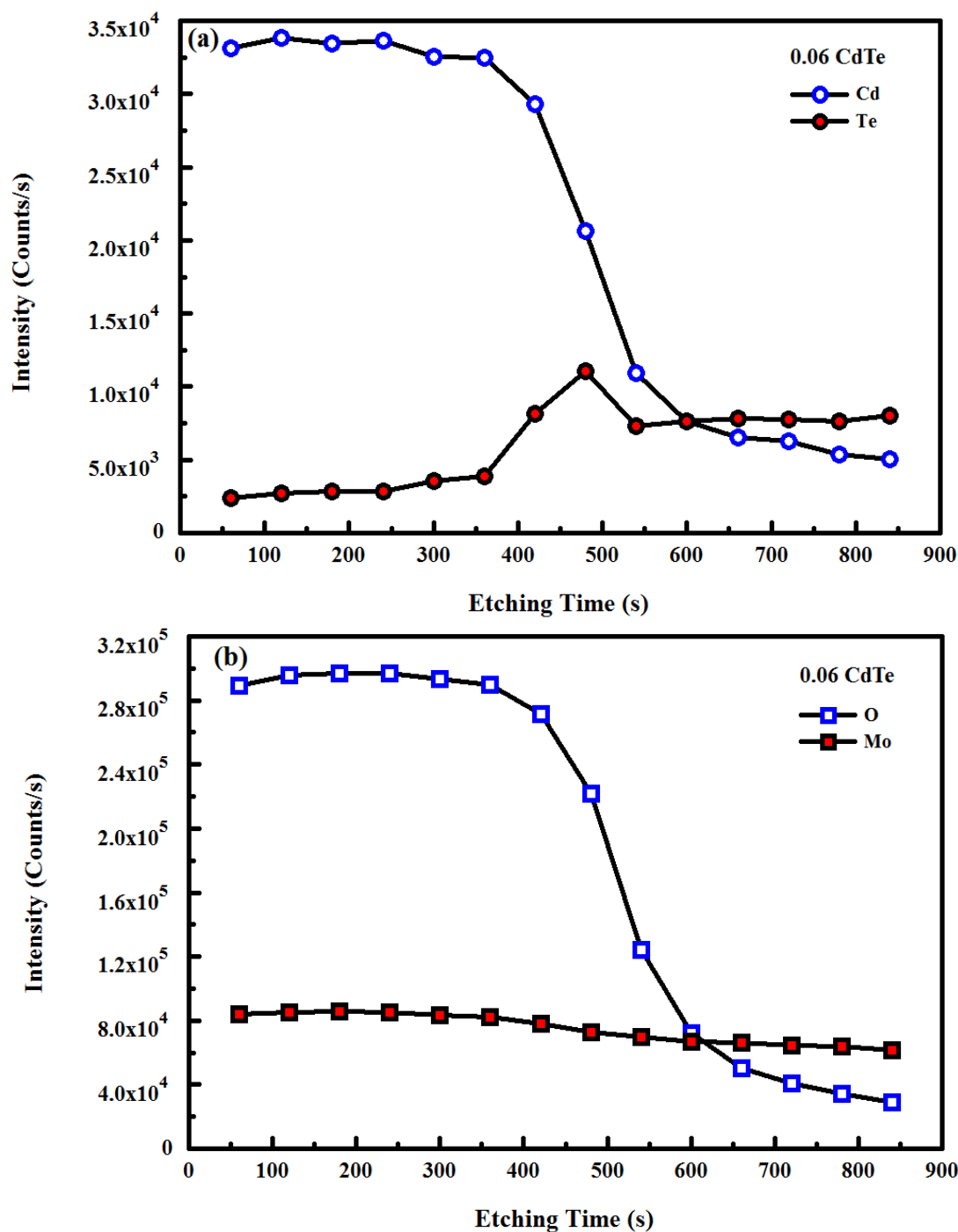
Fig. 5.14 XPS signal intensity versus etching time for MoO₃ thin film alloyed with 6% CdTe, (a) Cd and Te components, (b) Mo and O components.
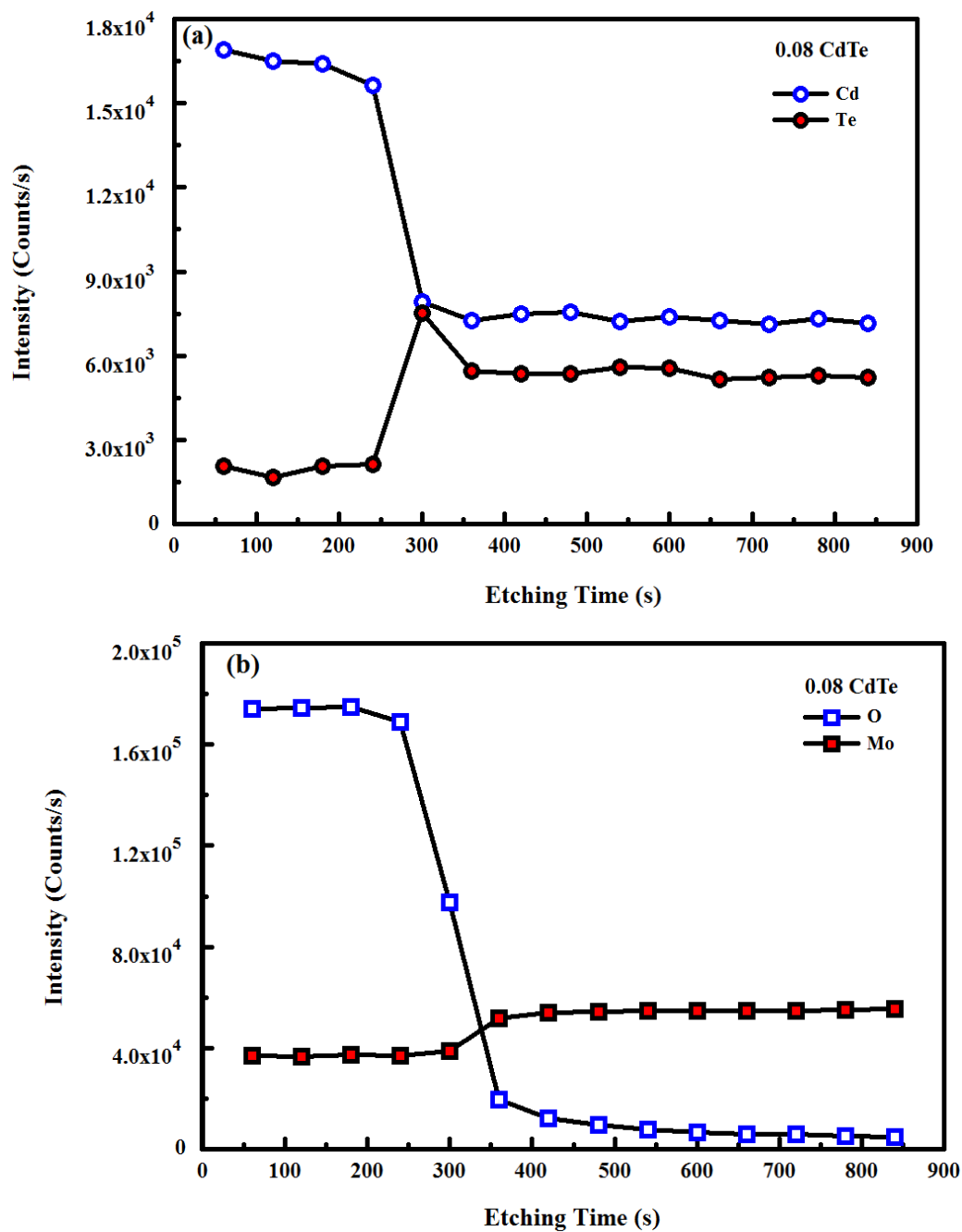
Fig. 5.15 XPS signal intensity versus etching time for MoO$_3$ thin film alloyed with 8% CdTe, (a) Cd and Te components, (b) Mo and O components.
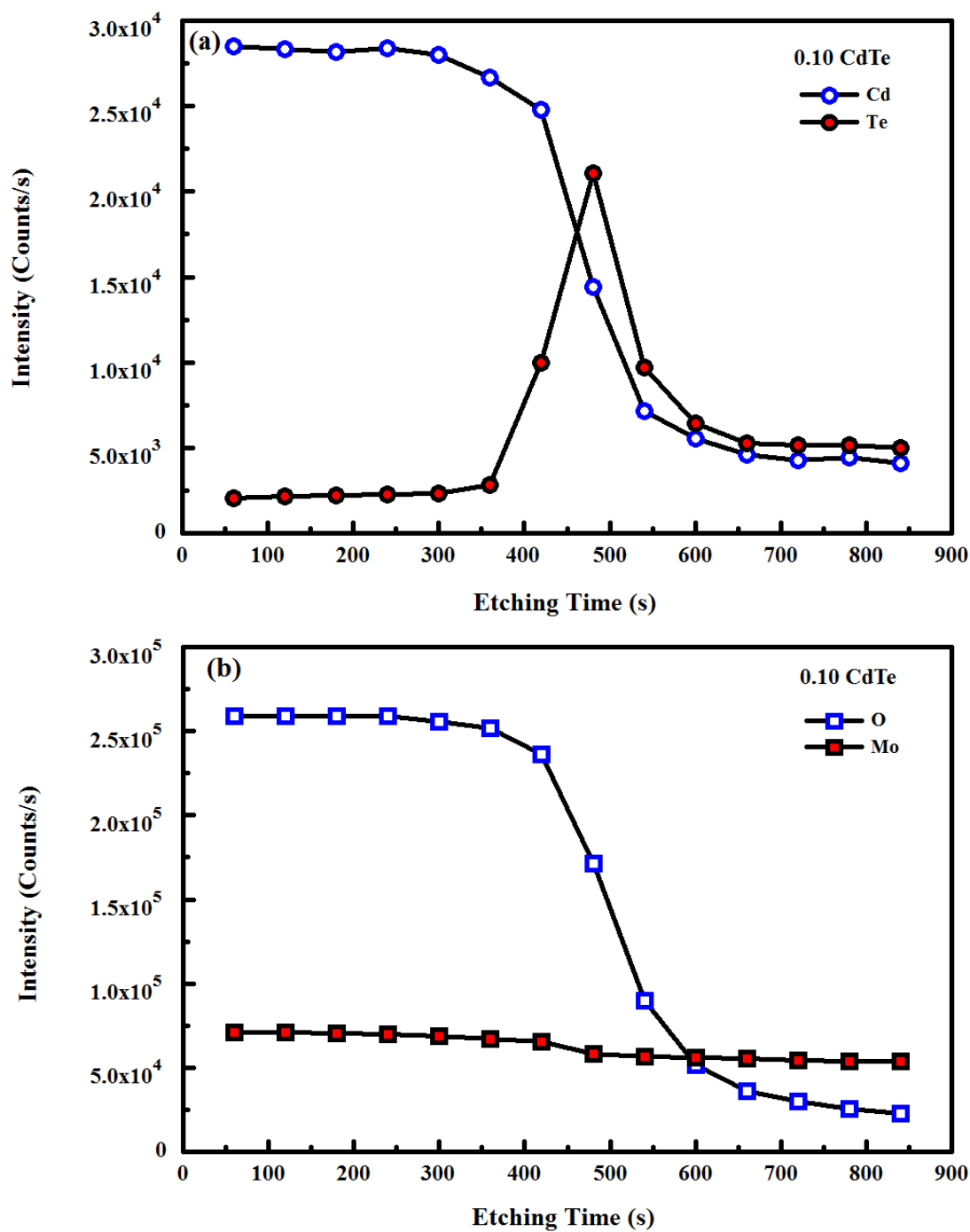
Fig. 5.16 XPS signal intensity versus etching time for MoO$_3$ thin film alloyed with 10% CdTe, (a) Cd and Te components, (b) Mo and O components.

5.5 Photocurrent measurements

The photoelectrochemical behavior of the prepared films was investigated by a linear sweep voltammetry technique. Figure 5.17a depicts the photocurrent density versus applied potential curves for the pure and CdTe-alloyed MoO_3 thin films as a function of the CdTe concentration. The photocurrent density of the pure MoO_3 film was negligible, whereas it increased steeply with the addition of CdTe. As discussed in section 4.5, the increase of the photocurrent can be explained by the potential-driven separation of photogenerated electrons and holes within the space-charge region of the alloyed films. The maximum photocurrent densities recorded at CdTe concentrations of 2%, 4%, 6%, 8% and 10% were 0.03, 0.13, 0.14, 0.21 and 0.24 mA/cm^2, respectively. It is obvious that the CdTe concentration had a great influence on the photocurrent response, which is attributable to the enhanced absorption of longer wavelengths of light. This behavior is explained by the decrease of the band gap of the alloyed films with the increase of the CdTe concentration, as previously discussed in the optical section. The variation of the integrated photocurrent density with CdTe concentration is shown in Fig. 5.17b.The continuous CdTe alloying improved the absorption in the alloyed films, leading to enhancement of the generation of electron-hole pairs that are the active species for producing the photocurrent.
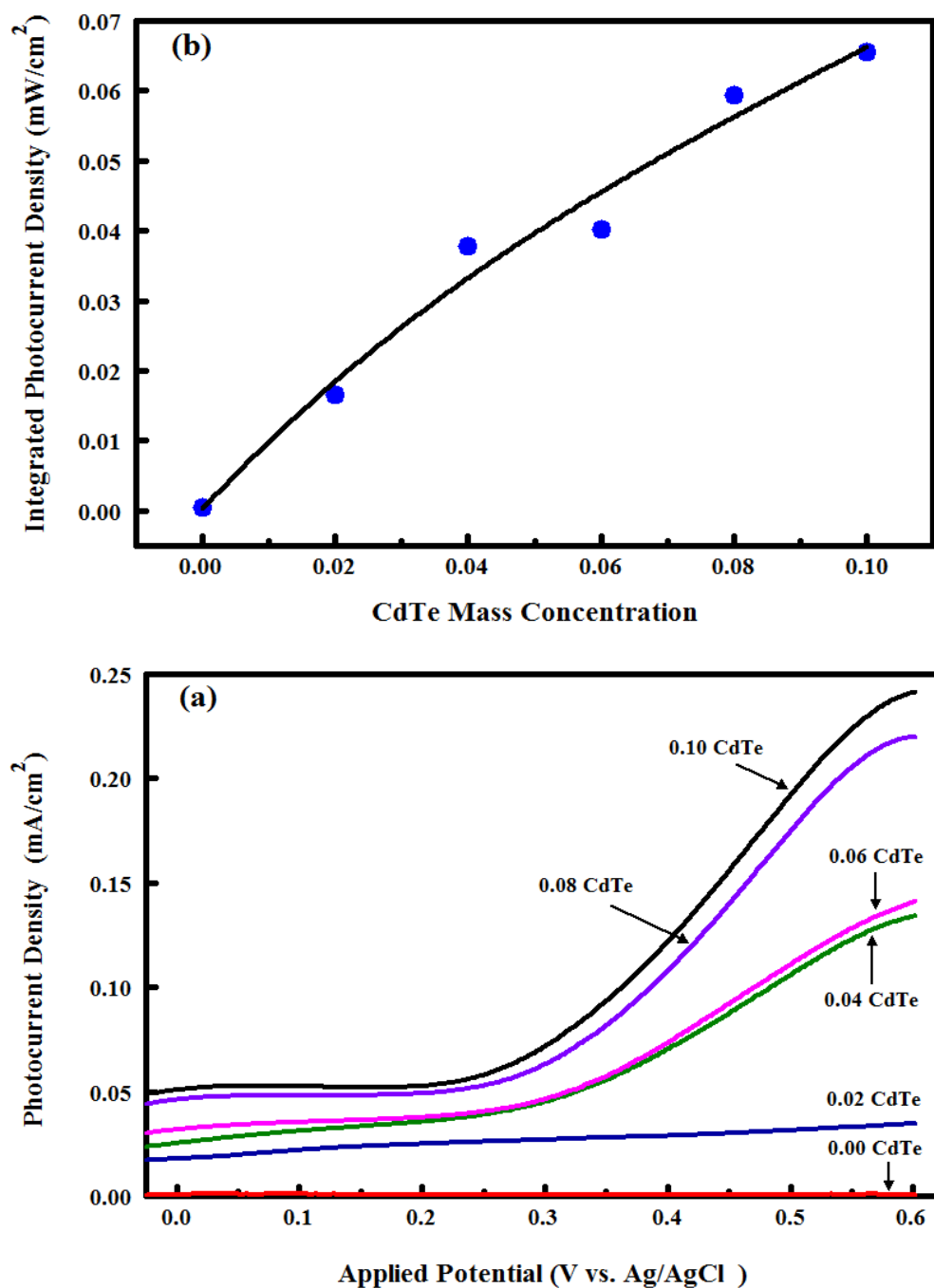
Fig. 5.17 (a) Photocurrent density-voltage curves of the pure and alloyed MoO$_3$ thin films under light illumination with an artificial sunlight simulator (300 mW/cm^2) CdTe mass concentration is indicated on each spectrum (b) Integrated photocurrent density of the alloyed films versus CdTe mass concentration

5.6 Comparison of band gap tenability of WO₃ and MoO₃ thin films in this study with previous reports

This section provides a comparison of the band gap tenability of WO_3 and MoO_3 thin films achieved in this study to the previous reports.

Table 5.2: Band gap (E_g) tenability of WO_3 and MoO_3 thin films by doping with elements and oxides using different methods. For comparison, the band gap tenability achieved in this study is also listed.

Dopant	Host (Metal oxide of interest)	Deposition Technique	Dopant Concentration	E_g Range (eV)	Ref.
Li	WO_3	RF	0.5-10 wt%	3.14–2.70	63
TiO_2		PLA	1-10 wt%	3.17–2.70	64
N		DC	4.7-12.5 at%	3.44–2.97	66
		Dual magnetron sputtering	5-50 sccm	3.19–2.93	68
		PLD	2.33-3.88 at%	3.15–2.84	70
V		DC	9-11 %	3.2–2.90	69
C		SP	0.04-0.13 mL	2.62–2.57	71
Fe_2O_3		hydrothermal reaction and post calcination	10-40 mmol/L	2.77–2.55	72
CdTe		Thermal evaporation	5-25 %	3.30–2.47	Current study
Li	MoO_3	SP	1-5 wt%	2.38–1.84	84
Ti		SP	3-9 wt%	3.04–3.25	85
ZnSe		Thermal evaporation	10-15 mol%	3.07–2.97	87
Nb		SP	3-9 at%	3.04–3.25	75
CdTe		Thermal evaporation	2-10 %	2.90–2.60	Current study

CHAPTER 6

CONCLUSIONS

The following conclusions can be drawn from the present study concerning band gap engineering of WO_3 and MoO_3 thin films through alloying with CdTe. WO_3 and MoO_3 thin films alloyed with CdTe were fabricated by thermal evaporation. Band gaps of WO_3 and MoO_3 thin films were engineered by mixing with specific mass concentrations of CdTe. The structural analysis showed that the pure WO_3 thin films were amorphous, while CdTe thin films were polycrystalline. No improvement in the crystallinity of WO_3 was observed as the concentration of CdTe increased. However, at the highest CdTe concentration, only CdTe polycrystalline phase was present. On other hand, the obtained pure MoO_3 and MoO_3 alloyed films were amorphous. The pure WO_3 and MoO_3 films had a columnar structure with a smooth surface. However, as the CdTe concentration increased, granular structures were developed with lighter roughness. The optical transparency of the mixed films was found to decrease with the increase of CdTe concentration indicating that the optical absorption increased and the absorption coefficient was raised from 4.5×10^5 cm^{-1} for pure WO_3 thin film to 9×10^5 cm^{-1} (twice that of pure film) at CdTe concentration of 25%. Similarly, the absorption coefficient of MoO_3 was raised from 3.75×10^5 cm^{-1} for pure MO_3 thin film to 1.18×10^6 cm^{-1} (triple that of pure film) at a CdTe concentration of 10%. A remarkable red-shift in the band gaps of WO_3 and MoO_3 thin films through alloying with CdTe was observed. The band gap values of the fabricated WO_3 thin films were found to be 3.35, 3.05, 2.87, 2.75, 2.58

and 2.47 eV at CdTe mass concentrations of 0%, 5%, 10%, 15%, 20% and 25%, respectively, while those of the fabricated MoO_3 thin films were found to be 2.90, 2.85, 2.75, 2.70, 2.65 and 2.60 at CdTe mass concentrations of 0%, 2%, 4%, 6%, 8% and 10%, respectively. The standard bowing equation described accurately the CdTe content dependence of the band gap of the alloyed films over the whole range of CdTe concentrations. The obtained experimental results indicate that the light absorption in the longer-wavelength portion of the visible light was enhanced, and hence the mixed films can be utilized for light harvesting, photovoltaic and photoelectrochemical applications over a wider portion of the visible spectrum. XPS analysis of unalloyed film showed that the sub-stoichiometric $WO_{2.96}$ and almost stoichiometric $MoO_{2.98}$ were obtained, and depth profiling analysis of the alloyed films confirmed the nonhomogeneous and homogeneous distributions of the constituent elements through the entire film depth of WO_3 and MoO_3, respectively. Moreover, the Cd:Te atomic ratio of unity in CdTe, W:O ratio in the stoichiometric WO_3 and Mo:O ratio in the stoichiometric MoO_3 compounds were no longer maintained as a result of the change of chemical states due to the Ar^+ bombardment. Photocurrent measurements showed a continuous increase in the photocurrent density of the alloyed films with the CdTe concentration and the optimum response in the alloyed WO_3 films was obtained at a CdTe concentration of 20%. The results obtained pave the way for the potential photovoltaic and photoelectrochemical applications of the CdTe-alloyed WO_3 thin films.

6.1 Suggestion for future work

This work is recommended to be redone in future by co-sputtering to control the band gap and crystallinity of the concerned metal oxides.

REFERENCES

[1]   C. Kittel, Introduction to Solid State Physics, 8th Edition. Hoboken, NJ: John Wiley &Sons, Inc., 2005.

[2]   M. Razeghi, Fundamental of Solid State Engineering, 2nd Edition, Springer Science+Business Media, Inc., USA, 2006.

[3]   J. J. Quinn, K. S. Yi, Solid State Physics - Principles and Modern Applications, Springer-Verlag, Berlin Heidelberg, New York, 2009.

[4]   B. E. A. Saleh, M. C. Teich, Fundamentals of Photonics, John Wiley & Sons, Inc., 1991.

[5]   S. M. Nadiu, Engineering Physics, Dorling Kindersley Pvt. Ltd., India, 2010.

[6]   M. E. Little, M. E. Kordesch, Band Gap Engineering in Sputter deposited $Sc_xGa_{1-x}N$, Applied Physics Letter, 78, 2001, 2891-2892.

[7]   S. Kasap, P. Capper, Springer Handbook of Electronic and Photonic Materials, Springer Science+ Business Media, Inc., 233 Spring Street, New York, 2006.

[8]   Y. Chen, J. Li, X. Yang, Z. Zhou, C. Q. Sun, Band Gap Modulation of the IV, III-V, and II-VI Semiconductors by Controlling the Solid Size and Dimension and the Temperature of Operation, The Journal of Physical Chemistry C, 115, 2011, 23338-23343.

[9]   S. Agarwal, K. H. Montgomery, T. B. Boykin, G. Klimeck, J. M. Woodall, Design Guidelines for True Green LEDs and High Efficiency Photovoltaics Using ZnSe/GaAs Digital alloys, Electrochemical and Solid State Letter, 13, 2010, H5-H7 .

[10]   P. K. Khanna, P. More, B.G. Bharate, A. K. Vishwanath, Studies on Light Emitting CdSe Quantum Dots in Commercial Polymethylmethacrylate, Journal of Luminescence, 130, 2010, 18–23.

[11]   N. M. Park, T. S. Kim, S. J. Park, Band gap Engineering of Amorphous Silicon Quantum Dots for Light-Emitting Diodes, Applied Physics Letter, 78, 2001, 2575-2577.

[12]   D. Bera, L. Qian, T. K. Tseng, P. H. Holloway, Quantum Dots and Their Multimodal Applications: A Review, Materials, 3, 2010, 2260-2345.

[13]   M. Chakrabarti, S. Dutta, S. Chttapadhyay, A. Sarkar, D. Sanyal, A. Chakrabarti, Grain Size Dependence of Optical Properties and Positron Annihilation Parameters in Bi_2O_3 Powder, Nanotechnology, 15, 2004, 1792-1796.

[14]   E. Jang, S. Jun, L. Pu, High Quality CdSeS Nanocrystals Synthesized by Facile Single Injection Process and Their Electroluminescence, Chemical Communications., 39, 2003, 2964–2965.

136

[15] J. S. Steckel, P. Snee, S. Coe-Sullivan, J. R. Zimmer, J. E. Halpert, P. Anikeeva, L.A. Kim, V. Bulovic, M.G. Bawendi, Color-Saturated Qreen-Emitting QD-LEDs, Angewandte Chemie International Edition, 45, 2006, 5796–5799.

[16] A. M. Smith, S. Nie, Semiconductor Nanocrystals: Structure, Properties, and Band Gap Engineering, Accounts of Chemical Research, 3, 2010, 190-200.

[17] J. Bang, J. Park, J. H. Lee, N. Won, J. Nam, J. Lim, B. Y. Chang, H. J. Lee, Bo. Chon, J. Shin, J. B. Park, J. H. Choi, K. Cho, S. M. Park, T. Joo, S. Kim, ZnTe/ZnSe (Core/Shell) Type-II Quantum Dots: Their Optical and Photovoltaic Properties, Chemistry of Materials., 22, 2010, 233–240.

[18] H. Morkoc, Handbook of Nitride Semiconductors and Devices, Volume 2, Electronic and Optical Processes in Nitrides, WILEY-VCH Verlag GmbH & Co. KGaA, Weinheim, , Germany, 2008.

[19] S. Kim, B. Fisher, H. J. Eisler, M. Bawendi, Type-II Quantum Dots: CdTe/CdSe (core/shell) and CdSe/ZnTe (core/shell) Heterostructures, Journal of the American Chemical Society, 125, 2003, 11466–11467.

[20] A. S. Ahmed, S. M. Muhamed, M. L. Singla, S. Tabassum, A. H. Naqvi, A. Azama, Band Gap Narrowing and Fuorescence Properties of Nickel Doped SnO_2 Nanoparticles, Journal of Luminescence, 131, 2011, 1–6.

[21] S. S. Pana, Y. D. Shen, X. M. Teng, Y. X. Zhang, L. Li, Z. Q. Chua, J. P. Zhang, G. H. Li, X. Hu, Substitutional Nitrogen-Doped Tin Oxide Single Crystalline

Submicrorod Arrays: Vertical Growth, Band Gap Tuning and Visible Light-Driven Photocatalysis, Materials Research Bulletin, 44, 2009, 2092–2098.

[22]   K. Nagamani, M.V. Reddy, Y. Lingappa, K. T. R. Reddy, R. W. Miles, Physical Properties of $Zn_xCd_{1-x}S$ Nanocrytalline Layers Synthesized by Solution Growth Method, International Journal of Optoelectronic Engineering, 2, 2012, 1-4.

[23]   D. A. Neamen, Semiconductor Physics and Devices Basic Principles, published by The McGraw-Hill Companies, Inc., New York, 2003.

[24]   D. P. Joseph, C. Venkateswaran , Band gap Engineering in ZnO by Doping with 3d Transition Metal Ions, Journal of Atomic, Molecular and Optical Physics, 2011, 2011, 1-7

[25]   F-H Wang, C-F Yang, Y-H Lee, Deposition of F-Doped ZnO Transparent Thin Films using ZnF_2-Doped ZnO Target under Different Sputtering Substrate Temperatures, Nanoscale Research Letters, 9, 2014, 97.

[26]   U. W. Pohl, Epitaxy of Semiconductors-Introduction to Physical Principles, Springer-Verlag Berlin Heidelberg, New York, 2013.

[27]   D. Lehr, M. Luka, M. R. Wagner, M. Bügler, A. Hoffmann, S. Polarz, Band-Gap Engineering of Zinc Oxide Colloids via Lattice Substitution with Sulfur Leading to Materials with Advanced Properties for Optical Applications Like Full Inorganic UV Protection, Chemistry of Matererials, 24, 2012, 1771−1778.

[28] S. Adachi, Properties of Semiconductor Alloys: Group-IV, III–V and II–VI Semiconductors, John Wiley & Sons Ltd, United Kingdom, 2009.

[29] P. Capper, M. Mauk, Liquid Phase Epitaxy of Electronic, Optical and Optoelectronic Materials, John Wiley & Sons Ltd, England, 2007.

[30] M. F. Al-Kuhaili, A. Kayani, S. M. A. Durrani , I. A. Bakhtiari, and M. B. Haider, Band Gap Engineering of Zinc Selenide Thin Films Through Alloying with Cadmium Telluride, ACS Applied Materials & Interfaces, 5, 2013, 5366−5372.

[31] Y. Wang, G. Ouyang, L. L. Wang , L. M. Tang , D. S. Tang , C. Q. Sun, Size and Composition-Induced Band Gap Change of Nanostructured Compound of II–VI Semiconductors, Chemical Physics Letters, 463, 2008, 383−386.

[32] K. Takahashi, A. Yoshikawa, A. Sandhu, Wide Band Gap Semiconductors: Fundamental Properties and Modern Photonic and Electronic Devices, Springer Science & Business Media, Springer-Verlag Berlin Heidelberg, New York, 2007.

[33] G. Turgut, E. Sönmez, Synthesis and Characterization of Mo-Doped SnO_2 Thin Films with Spray Pyrolysis, Superlattices and Microstructures, 69, 2014, 175−186.

[34] V. Musat, A. M. Rego, R. Monteiro, E. Fortunato, Microstructure and Gas-Sensing Properties of Sol–Gel ZnO Thin Films, Thin Solid Films, 516, 2008, 1512–1515.

[35] H. B. Huo, C. Wang, F. D. Yan, H. Z. Ren, M. Y. Shen, Room Temperature SnO_2 Thin Film Gas Sensor Fabricated on Si Nanospikes, Journal of Nanoscience and Nanotechnology, 9, 2009, 1–3.

[36] S. K. Deb, Dye-Sensitized TiO_2 Thin Film Solar Cell Research at the National Renewable Energy Laboratory (NREL), Solar Energy Materials & Solar Cells, 88, 2005, 1–10.

[37] R. J. Ellingson, J. B. Asbury, S. Ferrere, A. N. Ghosh, T. Lian, A. J. Nozik, Sub-Picosecond Injection of Electrons From Excited [Ru-complex dye] into TiO_2 using Transient Mid-Infrared Spectroscopy, Zeitschrift für Physikalische Chemie, Bd S., 212, 1999, 77–84.

[38] S. U. M. Khan, M. Al-Shahry, W. B. Ingler Jr., Efficient Photochemical Water Splitting by a Chemically Modified n-TiO_2, Science, 297, 2002, 2243–2245.

[39] K. R. Reyes-Gil , E. A. Reyes-García, D. Raftery, Nitrogen-Doped In_2O_3 Thin Film Electrodes for Photocatalytic Water Splitting, The Journal of Physical Chemistry C, 111, 2007, 14579–14588.

[40] F. Meng, J. Shi, Z. Liu, Y. Cui, Z. Lu, Z. Feng, High Mobility Transparent Conductive W-Doped In_2O_3 Thin Films Prepared at Low Substrate Temperature and its Application to Solar Cells, Solar Energy Materials and Solar Cells, 122, 2014, 70–74.

[41] Y. Huang, Z. Ji, C. Chen, Preparation and Characterization of p-type Transparent Conducting Tin-Gallium Oxide Films, Applied Surface Science, 253, 2007, 4819–4822.

[42] J. Papp , S. Soled , K. Dwight , A. Wold, Surface Acidity and Photocatalytic Activity of TiO_2, WO_3/TiO_2, and MoO_3/TiO_2 Photocatalysts, Chemistry of Matererials, 6, 1994, 496–500

[43] A. A. Ashkarran, A. I. zad, M. M. Ahadian, S. A. M. Ardakani, Synthesis and Photocatalytic Activity of WO_3 Nanoparticles Prepared by the arc Discharge Method in Deionized Water, Nanotechnology, 19, 2008, 195709.

[44] K. Girija, S. Thirumalairajan, G. S. Avadhani, D. Mangalaraj, N. Ponpandian, C. Viswanathan, Synthesis, Morphology, Optical and Photocatalytic Performance of Nanostructured β-Ga_2O_3, Materials Research Bulletin, 48, 2013, 2296–2303.

[45] Y. Chen, C. Lu, L. Xu, Y. Ma, W. Hou, J-J Zhu, Single-Crystalline Orthorhombic Molybdenum Oxide Nanobelts: Synthesis and Photocatalytic Properties, Crystal Engineering Communications, 12, 2010, 3740-3747.

[46] M. A. Carpenter, S. Mathur, A. Kolmakov, Metal Oxide Nanomaterials for Chemical Sensors, Springer Science+Business Media, New York, 2013.

[47] Z. Wei, Y. Liu, Y. Yang, P. Wu, Band Gap Engineering of SnO_2 by Epitaxial Strain: Experimental and Theoretical Investigations, Journal of Physical Chemistry C, 118, 20014, 6448-6453.

[48]   P. S. Shewale, S. I. Patil, M. D. Uplane, Preparation of fluorine-Doped Tin Oxide Films at Low Substrate Temperature by an Advanced Spray Pyrolysis Technique, and their Characterization, Semiconductor Science and Technology, 25, 2010, 115008.

[49]   T. Katoda, Photonic Device Comprising Molybdenum Oxide and Method of Fabrication, Patent EP1681730 A2, Jul 19, 2006.

[50]   A. Enesca, L. Andronic, A. Duta, S. Manolache, Optical Properties and Chemical Stability of WO_3 and TiO_2 Thin Films Photocatalysts, Roman Journal of Information Science and Technology 10, 2007, 269-277.

[51]   L. E. Deperoa, S. Groppellia, I. Natali-Soraa, L. Sangalettia, G. Sberveglieria, E. Tondellob, Structural Studies of Tungsten–Titanium Oxide Thin Films, Journal of Solid State Chemistry, 121, 1996, 379–387.

[52]   Y. Djaoued, P. V. Ashrit, S. Badilescu, R. Br̈uning, Synthesis and Characterization of Macroporous Tungsten Oxide Films for Electrochromic Application, Journal of Sol-Gel Science and Technology, 28, 2003, 235–244.

[53]   E. O. Zayim, P. Liu, S.-H. Lee, C. E. Tracy, J. A. Turner, J. R. Pitts, S. K. Deb, Mesoporous Sol-Gel WO_3 Thin Films via Poly(styrene-co-allyl-alcohol) Copolymer Templates, Solid State Ionics, 165, 2003, 65–72.

[54]   L. Yang, D. Ge, J. Zhao, Y. Ding, X. Kong, Y. Li, Improved Electrochromic Performance of Ordered Macroporous Tungsten Oxide Films for IR

Electrochromic Device, Solar Energy Materials and Solar Cells, 100, 2012, 251–257.

[55]   C. G. Granqvist, Handbook of Inorganic Electrochromic Materials, Elsevier Science, Amsterdam, The Netherlands, 1995.

[56]   W. H. Tao, C. H. Tasi, H_2S Sensing Properties of Noble Metal Doped WO_3 Thin Film Sensor Fabricated by Micromachining, Sensors and Actuators B: Chemical, 81, 2002, 237-247.

[57]   A. Ponzoni, E. Comini, G. Sberveglieri, J. Zhou, S. Z. Deng, N.S. Xu, Ding Y, Z. L. Wang, Ultrasensitive and Highly Selective Gas Sensors using Three-Dimensional Tungsten Oxide Nanowire Networks, Applied Physics Letters, 88, 2006, 203101-203103.

[58]   V. Khatko , S. Vallejos, J. Calderer, E. Llobet, X. Vilanova, X. Correig, Gas Sensing Properties of WO_3 Thin Films Deposited by rf Sputtering, Sensors and Actuators B: Chemical, 126, 2007, 400–405.

[59]   C. Santato, M. Odziemkowski, M. Ulmann, J. Augustynski, Crystallographically Oriented Mesoporous WO_3 Films: Synthesis, Characterization, and Applications, Journal of the American Chemical Society, 123, 2001, 10639-10649.

[60]   S. Berger, H. Tsuchiya, A. Ghicov, P. Schmuki, High Photocurrent Conversion Efficiency in Self-Organized Porous WO_3, Applied Physics Letters, 88, 2006, 203119.

[61] S.-H. Baeck, K.-S. Choi, T. F Jaramillo, G. D Stucky, E. W McFarland, Enhancement of Photocatalytic and Electrochromic Properties of Electrochemically Fabricated Mesoporous WO_3 Thin Films, Advanced Materials, 15, 2003, 1269–21673.

[62] S. Park, H. Kim, C. Jin, C. Lee, Intense Ultraviolet Emission from Needle-Like WO_3 Nanostructures Synthesized by Noncatalytic Thermal Evaporation, Nanoscale Research Letters, 6, 2011, 451-456.

[63] R. J. Bose, R. V. Kumar, S. K. Sudheer, V. R. Reddy, V. Ganesan, V. P. M. Pillai, Effect of Silver Incorporation in Phase Formation and Band Gap Tuning of Tungsten Oxide Thin Films, Journal of Applied Physics, 112, 2012, 114311.

[64] K. J. Lethy, D. Beena, V. P. M. Pillai, V. Ganesan, Band Gap Renormalization in Titania Modified Nanostructured Tungsten Oxide Thin Films Prepared by Pulsed Laser Deposition Technique for Solar Cell Applications, Journal of Applied Physics,104, 2008, 033515.

[65] H. Li, Y. Zhou, L. Chen, W. Luo, Q. Xu, X. Wang, M. Xiao, Z. Zou, Rational and Scalable Fabrication of High-Quality WO_3/CdS Core/Shell Nanowire Arrays for Photoanodes Toward Enhanced Charge Separation and Transport under Visible Light, Nanoscale, 5, 2013,11933.

[66] X. Sun, Z. Liu, H. Cao, Electrochromic Properties of N-Doped Tungsten Oxide Thin Films Prepared by Reactive DC-Pulsed Sputtering, Thin Solid Films, 519, 2011, 3032–3036.

[67] H. Watanabe, K. Fujikata, Y. Oaki, H. Imai, Band Gap Expansion of Tungsten Oxide Quantum Dots Synthesized in Sub-Nano Porous Silica, Chemical Communications., 49, 2013, 8477-8479.

[68] S. H. Mohamed, A. Anders, Structural, Optical and Electrical Properties of WO_xN_y Films Deposited by Reactive Dual Magnetron Sputtering, Surface and Coatings Technology, 201, 2006, 2977-2983.

[69] K. M. Karuppasamy, A Subrahmanyam, Results on the Electrochromic and Photocatalytic Properties of Vanadium Doped Tungsten Oxide Thin Films Prepared by Reactive dc Magnetron Sputtering Technique, Journal of Physics D: Applied Physics, 41, 2008, 035302.

[70] K. J. Lethy, S. Potdar, V. P. M. Pillai, V. Ganesan, Transparent and Low Resistive Nanostructured Laser Ablated Tungsten Oxide Thin Films by Nitrogen Doping: I. Nitrogen Pressure, Journal of Physics D: Applied Physics, 42, 2009, 095412.

[71] Y. Sun, C. J. Murphy, K. R. Reyes-Gil, E. A. Reyes-Garcia1, J. M. Thornton, N. A. Morris, D. Raftery, Photoelectrochemical and Structural Characterization of Carbon-Doped WO_3 Films Prepared via Spray Pyrolysis, International Journal of Hydrogen Energy, 34, 2009, 8476–8484.

[72] S. Han, J. Li, , X. Chen, Y. Huang, C. Liu, Y. Yang, Enhancing Photoelectrochemical Activity of Nanocrystalline WO_3 Electrodes by Surface

Tuning with Fe(III), International Journal of Hydrogen Energy, 37, 2012, 16810–16816.

[73]   M. F. Al-Kuhaili, S.M.A. Durrani, I.A. Bakhtiari, Pulsed Laser Deposition of Molybdenum Oxide Thin Films, Applied Physics A, 98, 2010, 609–615.

[74]   H. A. Tahini, X. Tan, S. N. Lou, J. Scott, R. Amal, Y. H. Ng, S. C. Smith, Mobile Polaronic States in α-MoO_3: An ab Initio Investigation of the Role of Oxygen Vacancies and Alkali Ions, ACS Applied Materials Interfaces, 8, 2016, 10911−10917.

[75]   S. S. Mahajan, S.H. Mujawar, P.S. Shinde, A.I. Inamdar, P.S. Patil, Structural, and Electrochromic Properties of Nb-Doped MoO_3 Thin Films, Applied Surface Science, 254, 2008, 5895–5898.

[76]   S. Calnan, Review: Applications of Oxide Coatings in Photovoltaic Devices, Coatings, 4, 2014, 162-202.

[77]   H. Simchi, B. E. McCandless, T. Meng, William N. Shafarman, Structure and Interface Chemistry of MoO_3 Back Contacts in $Cu(In,Ga)Se_2$ Thin Film Solar Cells, Journal of Applied Physics, 115, 2014, 033514.

[78]   H. M. Martínez, J. Torres, M.E. Rodríguez-García, L.D. López Carreño, Gas Sensing Properties of Nanostructured MoO_3 Thin Films Prepared by Spray Pyrolysis, Physica B: Condensed Matter, 407, 2012, 3199–3202.

[79] M. B. Rahmani, S.H. Keshmiri, J. Yua, A.Z. Sadekc, L. Al-Mashat, A. Moafi, K. Latham, Y.X. Li,W. Wlodarski, K. Kalantar-zadeh, Gas Sensing Properties of Thermally Evaporated Lamellar MoO_3, Sensors and Actuators B, 145, 2010, 13–19.

[80] M. Vasilopoulou, I. Kostis, A. M. Douvas, D. G. Georgiadou, A. Soultati, G. Papadimitropoulos, N. A. Stathopoulos, S. S. Savaidis, P. Argitis, D. Davazoglou, Vapor-Deposited Hydrogenated and Oxygen-Deficient Molybdenum Oxide Thin Films for Application in Organic Optoelectronics, Surface and Coatings Technology, 230, 2013, 202–207.

[81] M. Vasilopoulou, L. C. Palilis, D. G. Georgiadou, P. Argitis, S. Kennou, L. Sygellou, I. Kostis, G. Papadimitropoulos, N. Konofaos, A. A. Iliadis, D. Davazoglou, Reduced Molybdenum Oxide as an Efficient Electron Injection Layer in Polymer Light-Emitting Diodes, Applied Physics Letters, 98, 2011,123301.

[82] E. A. I. Saad, Dielectric Properties of Molybdenum Oxide Thin Films, Journal of optoelectronics and Advanced Materials, 7, 2005, 2743 – 2752.

[83] A. Chithambararaj, N. S. Sanjini, S. Velmathi, A. C. Bose, Preparation of h-MoO_3 and α-MoO_3 Nanocrystals: Comparative Study on Photocatalytic Degradation of Methylene Blue under Visible Light Irradiation, Physical Chemistry Chemical Physics, 15, 2013, 14761—14769.

[84]   M. Kovendhan, D. Joseph, P. Manimuthu, S. Sambasivam, S.N. Karthick,K. Vijayarangamuthu, A. Sendilkumar, K. Asokan, H. J. Kim, B. C. Choi, C. Venkateswaran, R. Mohan, 'Li' Doping Induced Physicochemical Property Modifications of MoO$_3$ Thin Films, Applied Surface Science, 284, 2013, 624–633.

[85]   S. S. Mahajan, S. H. Mujawar, P. S. Shinde, A.I.Inamdar, P. S. Patil, Structural, Morphological, Optical and Electrochromic Properties of Ti-Doped MoO$_3$ Thin Films, Solar Energy Materials & Solar Cells, 93, 2009, 183–187.

[86]   Y. J. Lee, W. T. Nichols, D.-G. Kim, Y. D. Kim, Chemical Vapour Transport Synthesis and Optical Characterization of MoO$_3$ Thin Films, Journal of Physics D: Applied Physics, 42, 2009, 115419.

[87]   S. A. Tomás, M.A. Arvizu, O. Zelaya-Angel, P. Rodríguez, Effect of ZnSe Doping on the Photochromic and Thermochromic Properties of MoO$_3$ Thin Films, Thin Solid Films, 518, 2009, 1332–1336

[88]   A. Bouzidi, N. Benramdane, H. Tabet-Derraz, C. Mathieu, B. Khelifa, R. Desfeux, Effect of Substrate Temperature on the Structural and Optical Properties of MoO$_3$ Thin Films Prepared by Spray Pyrolysis Technique, Materials Science and Engineering, B97, 2003, 5-8 .

[89]   R. Sivakumar, R. Gopalakrishnan, M. Jayachandran, C. Sanjeeviraja, Characterization on Electron Beam Evaporated α-MoO$_3$ Thin Films by the Influence of Substrate Temperature, Current Applied Physics, 7, 2007, 51–59.

[90] R. Sivakumar, C. Sanjeeviraja, M. Jayachandran, R. Gopalakrishnan, S. N. Sarangi, D. Paramanik, T. Som, MeV N$^+$-Ion Irradiation Effects on MoO$_3$ Thin Films, Journal of Applied Physics, 101, 2007, 034913.

[91] E. B. Santos, F. A. Sigoli, I. O. Mazali, Structural Evolution in Crystalline MoO$_3$ Nanoparticles with Tunable Size, Journal of Solid State Chemistry, 190, 2012, 80–84.

[92] X.-F. Gao, W.-T. Sun, G. Ai, L.-M. Peng, Photoelectric Performance of TiO$_2$ Nanotube Array Photoelectrodes Cosensitized with CdS/CdSe Quantum Dots, Applied Physics Letters, 96, 2010,153104.

[93] P. Lv, H. Yang, W. Fu, H. Sun, W. Zhang, M. Li, H. Yao, Y. Chen, Y. Mu, L. Yang, J. Ma, M. Sun, Q. Li, S. Su, The Enhanced Photoelectrochemical Performance of CdS Quantum Dots Sensitized TiO$_2$ Nanotube/Nanowire/Nanoparticle Arrays Hybrid Nanostructures, Crystal Engineering Communication, 16, 2014, 6955–6962.

[94] L. Irimpan, V. P. N. Nampoori, P.Radhakrishnan, Optical Engineering by the Nanocomposites of ZnO-CdS/TiO$_2$, Optical Engineering, 50, 2011, 069001.

[95] L. Irimpan, V. P. N. Nampoori, P. Radhakrishnan, Spectral and Nonlinear Optical Characteristics of Nanocomposites of ZnO–CdS, Journal of Applied Physics,103, 2008, 094914.

149

[96]   D. A. Bussian, S. A. Crooker, M. Yin, M. Brynda, A. L. Efros, V. I. Klimov, Tunable Magnetic Exchange Interactions in Manganese-Doped Inverted Core–Shell ZnSe–CdSe Nanocrystals, Nature Materials, 8, 2009, 35-40.

[97]   Z. Han, L. Wei, L. Tang, C. Chen, H. Pan, J. Chen, Aligned CdSe@ZnO Flower-Rod Core-Shell Nanocable as Photovoltaic Application, Journal of Power Sources, 239, 2013, 546-552.

[98]   S. Lalitha, S.Z. Karazhanov, P. Ravindran, S. Senthilarasu, R. Sathyamoorthy, J. Janabergenov, Electronic Structure, Structural and Optical Properties of Thermally Evaporated CdTe Thin Films, Physica B, 387, 2007, 227–238.

[99]   G. Yang,a Y. Jung, S. Chun, D. Kim, J. Kima, Materials CdCl$_2$ Activation Annealing of CdTe Microwires Grown by Close-Spaced Sublimation Method, ECS Solid State Letters, 3, 2014, 47-50.

[100] Z.-Q. Liu, X.-H. Xie, Q.-Z. Xu, S.-H. Guo, N Li, Y.-B. Chen, Y.-Z. Su, Electrochemical Synthesis of ZnO/CdTe Core-Shell Nanotube Arrays for Enhanced Photoelectrochemical Properties, Electrochimica Acta, 98, 2013, 268–273.

[101] X. Cao, C. Zhao, X. Lan, G. Gao, W. Qian, Y. Guo, Microwave-Enhanced Synthesis of Cu$_3$Se$_2$ Nanoplates and Assembly of Photovoltaic CdTe-Cu$_3$Se$_2$ Clusters, The Journal of Physical Chemistry C, 111, 2007, 6658-6662.

[102] Q. Wang, X. Yang, L. Chi, M. Cui, Photoelectrochemical Performance of CdTe Sensitized TiO_2 Nanotube Array Photoelectrodes, Electrochimica Acta, 91, 2013, 330– 336.

[103] H. Feng, T. T. ThanhThuy, L. Chen, L. Yuan, Q. Cai, Visible Light-Induced Efficiently Oxidative Decomposition of p-Nitrophenol by $CdTe/TiO_2$ Nanotube Arrays, Chemical Engineering Journal, 215–216 , 2013, 591–599.

[104] A. M. Smith, A. M. Mohs, S. Nie, Tuning the Optical and Electronic Properties of Colloidal Nanocrystals by Lattice Strain, Nature Nanotechnology, 4, 2009, 56-63.

[105] A. Rockett, The Materials Science of Semiconductors, 3rd Edition, published by Springer Science+Business Media, LLC, New York, 2008.

[106] J. Singh, Electronic and Optoelectronic of Semiconductor Structures, Cambridge University Press, New York, 2003.

[107] A. Erol Dilute III-V Nitride Semiconductors and Material Systems, Physics and Technology, Springer Berlin Heidelberg, New York, 2008.

[108] V. M. Huxter, Optical and Material Properties of Colloidal Semiconductor Nanocrystals, PhD Dissertation, Department of Chemistry, University of Toronto, 2009.

[109] M. S. Dresselhaus, Solid State Physics. Part II: Optical Properties of Solids, (MIT Solid State Physics Course) (Cambridge, MA: MIT), 2001.

[110] K.S. S. Harsha, Principles of Vapor Deposition of Thin Films, Elsevier, Great Britain, 2006.

[111] C. Suryanarayana, M.G. Norton, X-Ray Diffraction: A Practical Approach, Plenum Press, New York, 1998.

[112] S. Bucak, D. Rende, Cooloidand and Surface Chemistry, A Labratory Guide for Exploration of the Nano World, CRC Press, Taylor & Francis Group, LLC, US, 2004.

[113] C. A. Batt, M.-L. Tortorello, Encyclopedia of Food Microbiology, 2nd Edition, Elsevier , UK, 2014.

[114] D. E. Reisner, Bionanotechnology: Global Prospects, CRC Press, Taylor &Francis Group, LLC, US, 2009.

[115] A. Sengupta, S. K. Sarkar, Introduction to Nano: Basics to Nanoscience and Nanotechnology, Springer-Verlag Berlin Heidelberg, New York, 2015.

[116] H. A. Strobel, W. R. Heineman, Chemical Instrumentation: A Systematic Approach, 3rd Edition, John Wiley & Sons, Inc., New York, 1989.

[117] J. C. Vickerman, I.S. Gilmore, Surface analysis- the principal techniques, 2nd Edition, John Wiley & Sons, Ltd., UK, 2009.

[118] J. Cazes, Analytical Instrumentation Handbook, 3rd Edition, Taylor & Francis Group, LLC, US, 2004.

[119] R. W.   Kelsall, I. W. Hamley, M. Geoghegan, Nanoscale Science and Technology, John Wiley & Sons, Ltd., England, 2005.

[120] D. Briggs, S.M. Seah, Practical Surface Analysis, Wiley, New York, NY, USA, 1990.

[121] ICDD files: (00-010-0207 and 00-070-8041) for CdTe.

[122] K. R. Murali, M. Matheline, R. John, Characteristics of Brush Electrodeposited CdS films, Chalcogenide Letters, 6, 2009, 483 – 490.

[123] O. S. Heaven, Optical Properties of Thin Solid Films, published by Dover England, 1995.

[124] H. A. Wahab, A. A. Salama, A.A. El-Saeid, O. Nur, M. Willander, I.K. Battisha Optical, Structural and Morphological Studies of (ZnO) Nano-Rod Thin Films for Biosensor Applications using Sol Gel Technique, Results in Physics, 3, 2013, 46–51.

[125] S. C. Bhatia, Advanced Renewable Energy Systems, © Woodhead Publishing India Pvt. Ltd., 2014.

[126] Q. Deng, X. Han, Y. Gao, G. Shao, Remarkable Optical Red Shift and Extremely High Optical Absorption Coefficient of V-Ga Co-Doped TiO_2, Journal of Applied Physics, 112, 2012, 013523.

[127] J. Tauc, Amorphous and Liquid Semiconductors. Plenum Press, New York, 1974.

153

[128] S. M. A. Durrania,, E.E. Khawajaa, M.A. Salim, M.F. Al-Kuhaili, A.M. Al-Shukri, Effect of Preparation Conditions on the Optical, and Thermochromic Properties of Thin Films of Tungsten Oxide, Solar Energy Materials & Solar Cells, 71, 2002, 313–325.

[129] K. S. Rahman , F. Haque , N.A. Khan , M. A. Islam , M.M. Alam , Z.A. Alothman , K. Sopian, N. Amin, Effect of $CdCl_2$ Treatment on Thermally Evaporated CdTe Thin Films, Chalcogenide Letters, 11, 2014, 129 – 139.

[130] A. Erol, Dilute III-V Nitride Semiconductors and Material Systems, Physics and Technology, Springer Berlin Heidelberg, New York, 2008.

[131] Y. Liang, L. Zhai, X. Zhao, D. Xu, Band Gap Engineering for Semiconductor Nanowires Through Composition Modulation. The Journal of Physical Chemistry B, 109, 2005, 7120–7123.

[132] G. Orsal, Y. El Gmili, N. Fressengeas, J. Streque, R. Djerboub, T. Moudakir, S. Sundaram, A. Ougazzaden, J.P. Salvestrini, Band Gap Energy Bowing Parameter of Strained and Relaxed InGaN Layers, Optical Materials Express, 4, 2014, 1030.

[133] D. Gogova, K. Gesheva, A. Szekeres, M. Sendova-Vassileva, Structural and Optical Properties of CVD Thin Tungsten Oxide Films, Physica Status Solidi (a), 176, 1999, 969-984.

[134] L. M. Bertus , C. Faure , A. Danine , C. Labrugere , G. Campet , A. Rougier b, A. Duta, Synthesis and Characterization of WO_3 Thin Films by Surfactant Assisted

Spray Pyrolysis for Electrochromic Applications, Materials Chemistry and Physics, 140, 2013, 49-59.

[135] V. V. Ganbavle, G.L. Agawane, A.V. Moholkar, J. H. Kim, K.Y. Rajpure, Structural, Optical, Electrical and Dielectric Properties of the Spray-Deposited WO$_3$ Thin Films, Journal of Materials Engineering and Performance, 23, 2014, 1204–1213.

[136] R. Sivakumar, R. Gopalakrishnan, M. Jayachandran, C. Sanjeeviraja, Investigation of X-ray Photoelectron Spectroscopic (XPS), Cyclic Voltammetric Analyses of WO$_3$ Films and their Electrochromic Response in FTO/WO$_3$/electrolyte/FTO Cells, Smart Materials and Structures, 15, 2006, 877–888.

[137] D. Barreca, S. Bozza, G. Carta, G. Rossetto, E. Tondello, P. Zanella, Structural and Morphological Analyses of Tungsten Oxide Nanophasic Thin Films Obtained by MOCVD, Surface Science, 532–535, 2003, 439–443.

[138] S. Bai, K. Zhang, L. Wang, J. Sun, R. Luo, D. Li, A. Chen, Synthesis Mechanism and Gas Sensing Application of Nanosheet-Assembled Tungsten Oxide Microspheres, Journal of Materials Chemistry A, 2, 2014, 7927-7934.

[139] A. Mozalev, V. Khatko, C. Bittencourt, A. W. Hassel, G. Gorokh, E. Llobet, X. Correig, Nanostructured Column-like Tungsten Oxide Film by Anodizing Al/W/Ti Layers on Si, Chemistry of Materials, 20, 2008, 6482–6493.

[140] A. P. Shpak, A.M. Korduban , M.M. Medvedskij, V.O. Kandyba, XPS Studies of Active Elements Surface of Gas Sensors Based on WO_{3-x} Nanoparticles, Journal of Electron Spectroscopy and Related Phenomena, 156–158, 2007, 172–175.

[141] H. Al-Kandari, F. Al-Kharafi, N. Al-Awadi, O.M. El-Dusouqui, A. Katrib, Surface Electronic Structure–Catalytic Activity Relationship of Partially Reduced WO_3 Bulk or Deposited on TiO_2, Journal of Electron Spectroscopy and Related Phenomena, 151, 2006, 128–134.

[142] G. Wang, Y. Ling, H. Wang, X. Yang, C. Wang, J. Z. Zhang, Y. Li, Hydrogen-Treated WO_3 Nanoflakes Show Enhanced Photostability, Energy & Environmental Science, 5, 2012, 6180-6187.

[143] T. Tesfamichael, M. Arita, T. Bostrom, J. Bell, Thin Film Deposition and Characterization of Pure and Iron-Doped Electron-Beam Evaporated Tungsten Oxide for Gas Sensors, Thin Solid Films, 518, 2010, 4791–4797.

[144] C. Guo, S. Yin, L. Huang, T. Sato, Synthesis of One-Dimensional Potassium Tungsten Bronze with Excellent near-Infrared Absorption Property, ACS Applied Material Interfaces, 3, 2011, 2794–2799.

[145] Y. F. Lu, and H. Qiu, Laser coloration and bleaching of amorphous WO_3 thin film, Journal of Applied Physics, 88, 2000, 1082-1087.

[146] R. Azimirad, N. Naseri, O. Akhavan, A. Z. Moshfegh, Hydrophilicity Variation of WO$_3$ Thin Films with Annealing Temperature, Journal of Physics D: Applied Physics, 40, 2007, 1134–1137.

[147] J. Li, Y. Liu, Z. Zhu, G. Zhang, T. Zou, Z. Zou, S. Zhang, D. Zeng, C. Xie, A Full-Sunlight-Driven Photocatalyst with Super Long-Persistent Energy Storage Ability, Scientific Reports, 3, 2013, 2409.

[148] A. M. Smith, M. G. Kast, B. A. Nail, S. Aloni, S. W. Boettcher, A Planar-Defect-Driven Growth Mechanism of Oxygen Deficient Tungsten Oxide Nanowires, Journal of Materials Chemistry A, 2, 2014, 6121.

[149] F. O. Silva, M. S. Carvalho, R. Mendonça, W. A. A. Macedo, K. Balzuweit, P. Reiss, M. A. Schiavon, Effect of Surface Ligands on the Optical Properties of Aqueous Soluble CdTe Quantum Dots, Nanoscale Research Letters, 7, 2012, 536.

[150] H. Borchert, D. V. Talapin, N. Gaponik, C. McGinley, S. Adam, A. Lobo, T. Mo1ller, H. Weller, Relations between the Photoluminescence Efficiency of CdTe Nanocrystals and Their Surface Properties Revealed by Synchrotron XPS, The Journal of Physical Chemistry B, 107, 2003, 9662-9668.

[151] M.-L. Chen, J.-W. Liu, B. Hu, M.-L. Chen, J.-H. Wang, Conjugation of Quantum Dots with Graphene for Fluorescence Imaging of Live Cells, Analyst, 136, 2011, 4277.

[152] D. N. Bose, M. S. Hedge, S. Basu, K. C. Mandal, XPS Investigation of CdTe Surfaces: Effect of Ru Modification, Semiconductor Science and Technology, 4, 1989, 866-870.

[153] A. J. Ricco, H. S. White, M. S. Wrighton, X-ray Photoelectron and Auger Electron Spectroscopic Study of the CdTe Surface Resulting from Various Surface Pretreatments: Correlation of Photoelectrochemical and Capacitance-Potential Behavior with Surface Chemical Composition, Journal of Vacuum Science & Technology A, 2, 1984, 910-915.

[154] M. S. Khan, M. N. Ashiq, M. F. Ehsan, T. He, S. Ijaz, Controlled-Synthesis of Cobalt Telluride Superstructures for the Visible Light Photoconversion of Carbon Dioxide into Methane, Applied Catalysis A: General, 487, 2014, 202-209.

[155] Y. Liu, W. Chen, A. G. Joly, Y. Wang, C.Pope, Y. Zhang, J.-O. Bovin, P. Sherwood, Comparison of Water-Soluble CdTe Nanoparticles Synthesized in Air and in Nitrogen, The Journal of Physical Chemistry B, 110, 2006, 16992-7000.

[156] B. Lv, S. Hu, W. Li, X. Di, L. Feng, J. Zhang, L. Wu, Y. Cai, B. Li, Z. Lei, Preparation and Characterization of Sb_2Te_3 Thin Films by Coevaporation, International Journal of Photoenergy, ID 476589,2010 , 1-4.

[157] A. Mekki, G.D. Khattak, L.E. Wenger, Structural and Magnetic Investigations of Fe_2O_3–TeO_2 Glasses, Journal of Non-Crystalline Solids, 352, 2006, 3326–3331.

158

[158] Q. LI, D. GU, F. GAN, TeO$_x$ Thin Films for Write-Once Optical Recording Media, Journal of Materials Science & Technology, 6, 2004, 678-680.

[159] F. Wang, A. Schwartzman, A. L. Fahrenbruch, R. Sinclair,R. H. Bubs, C. M. Stahle, Kinetics and Oxide Composition for Thermal Oxidation of Cadmium Telluride, Journal of Applied Physics, 62, 1987 1469-1476.

[160] C. Baslak, M. D. Kars, M. Karamana, M. Kus, Y. Cengeloglu, M. Ersoz, Biocompatible Multi-Walled Carbon Nanotube–CdTe Quantum Dot–Polymer Hybrids for Medical Applications, Journal of Luminescence, 160, 2015, 9–15.

[161] C. Luo, B. Li, H. Peng, X. Tang, Y. Wang, J. Travas-sejdic, The Effect of Photo-Irradiation on the Optical Properties of Thiol-Capped CdTe Quantum Dots, Journal of Nanoscience and Nanotechnology, 12, 2011, 1–8.

[162] T. J. Driscoll, L.D. McCormick, W.C. Lederer, Altered Layer Formation and Sputtering Yields for 5 keV Ar$^+$ Bombardment of MoO$_3$ and WO$_3$, Surface Science, 187, 1987, 539-558.

[163] H. Kaper, I. Djerdj, S. Gross, H. Amenitsch, M. Antonietti, B. M. Smarsly, Ionic Liquid- and Surfactant-Controlled Crystallization of WO$_3$ Films, Physical Chemistry Chemical Physics, 17, 2015, 18138-18145.

[164] J. Malherbe, H. Martinez, B. Fernández , C. Pécheyran, O. F.X. Donard, The Effect of Glow Discharge Sputtering on the Analysis of Metal Oxide Films, Spectrochimica Acta Part B, 64, 2009, 155–166.

[165] D. J. O'Connor, B. A. Sexton, R. St. C. Smart, Surface Analysis Methods in Materials Science, Springer-Verlag Berlin Heidelberg, New York, 1992.

[166] X. Mathew, G. W. Thompson, V.P. Singh, J.C. McClure, S. Velumani, N.R. Mathews, P.J. Sebastian, Development of CdTe Thin Films on Flexible Substrates-A Review, Solar Energy Materials & Solar Cells, 76 ,2003, 293–303.

[167] T. Zhua, M. N. Chonga, Y. W. Phuana, E-S Chana, Electrochemically Synthesized Tungsten Trioxide Nanostructures for Photoelectrochemical Water Splitting: Influence of Heat Treatment on Physicochemical Properties, Photocurrent Densities and Electron Shuttling, Colloid Surface A, 484, 2015, 297–303.

[168] R. Reichert, Z. Jusys, R. J. Behm, A Novel Photoelectrochemical Flow Cell with Online Mass Spectrometric Detection: Oxidation of Formic Acid on a Nanocrystalline TiO_2 Electrode, Physical Chemistry Chemical Physics, 16, 2014, 25076-25080.

[169] W. L. Kwong, H. Qiu, A. Nakaruk, P. Koshy, C.C. Sorrell, Photoelectrochemical Properties of WO_3 Thin Films Prepared by Electrodeposition, Energy Procedia, 34, 2013, 617 – 626.

[170] H-J Lin, D-Y Lin, J-Z Hong, C-S Yang, C-M Lin, C-F Lin, A Study of the Grain Size and Electric Properties of Mn-Doped ZnO Thin Films Grown by Plasma-Assisted Molecular Beam Epitaxy, Physica Status Solidi C, 6, 2009, 1468–1471.

[171] S. Mridha, D. Basak, Aluminium Doped ZnO Films: Electrical, Optical and Photoresponse Studies, Journal of Physics D: Applied Physics, 40, 2007, 6902−6907.

[172] A. Iqbal, A. Mahmood, T. M. Khan, E. Ahmed, Structural and Optical Properties of Cr-Doped ZnO Crystalline Thin Films Deposited by Reactive Electron Beam Evaporation Technique, Progress in Natural Science: Materials International 23, 2013, 64–69.

[173] Z. Hussain, Optical and Electrochromic Properties of Heated and Annealed MoO_3 Thin Films, Journal of Materials Research, 16, 2001, 2695-2708.

[174] S. Subbarayudu , V. Madhavi, S. Uthanna, Post-Deposition Annealing Controlled Structural and Optical Properties of RF Magnetron Sputtered MoO_3 Films, Advanced Materials Letters, 4, 2013, 637-642.

[175] A. Siokou, G. Leftheriotis, S. Papaefthimiou, P. Yianoulis, Effect of Tungsten and Molybdenum Oxidation States on the Thermal Coloration of Amorphous WO_3 and MoO_3 Films, Surface Science, 482-485, 2001, 294-299.

[176] P. Qin, G. Fang, W. Ke, F. Cheng, Q. Zheng, J. Wan, H. Lei, X. Zhao, In Situ Growth of Double-Layer MoO_3/MoS_2 Film from MoS_2 for Hole-Transport Layers in Organic Solar Cell, Journal of Materials Chemistry A, 2, 2014, 2742–2756.

[177] T. H. Chiang, H. C. Yeh, The Synthesis of MoO_3 by Ethylene Glycol, Materials, 6, 2013, 4609-4625.

[178] S. R. G. Carrazfin, C. Martfn, V. Rives , R. Vidal, Selective Oxidation of Isobutene to Methacrolein on Multiphasic Molybdate-based Catalysts, Applied Catalysis A: General, 135, 1996, 95-123.

[179] H. Lü, W. Ren, W. Liao, W. Chen, Y. Li, Z. Suo, Aerobic Oxidative Desulfurization of Model Diesel using a B-type Anderson Catalyst $[(C_{18}H_{37})_2N(CH_3)_2]_3Co(OH)_6Mo_6O_{18}\cdot3H_2O$, Applied Catalysis B: Environmental, 138– 139, 2013, 79- 83.

[180] O. M. Hussain, K.S. Rao, Characterization of Activated Reactive Evaporated MoO_3 Thin Films for Gas Sensor Applications, Materials Chemistry and Physics, 80, 2003, 638–646.

[181] R. Prakash, D. M. Phase, R. J. Choudhary, R. Kumar, Structural, Electrical, and Magnetic Properties of $Mo_{1-x}Fe_xO_2$ (x = 0-0.05) Thin Films Grown by Pulsed Laser Ablation, Journal of Applied Physics, 103, 2008, 043712-6.

[182] K. Dewangan, N. N. Sinha, P. K. Sharma, A. C. `Pandey, N. Munichandraiah, N. S. Gajbhiye, Synthesis and Characterization of Single-Crystalline α-MoO_3 Nanofibers for Enhanced Li-ion Intercalation Applications, Crystal Engineering Communication, 13, 2011, 927–933.

[183] N. Chaturvedi, S. K. Swami, V. Dutta, Electric Field Assisted Spray Deposited MoO_3 Thin Films as a Hole Transport Layer for Organic Solar Cells, Solar Energy 137, 2016, 379–384.

[184] W. Cui, N. Cheng, Q. Liu, C. Ge, A. M. Asiri, X. Sun, Mo_2C Nanoparticles Decorated Graphitic Carbon Sheets: Biopolymer-Derived Solid-State Synthesis and Application as an Efficient Electrocatalyst for Hydrogen Generation, ACS Catalysis, 4, 2014, 2658−2661.

[185] R. Cárdenas, J. Torres, J.E. Alfonso, Optical characterization of MoO_3 thin films produced by continuous wave CO_2 laser-assisted evaporation, Thin Solid Films 478, 2005, 146– 151.

[186] M. F. Al-Kuhaili, S. H. A. Ahmad, S.M.A. Durrani , M. M. Faiz, A. Ul-Hamid, Energy-saving spectrally-selective coatings based on MoO_3/Ag thin films, Materials and Design, 73, 2015, 15–19.

VITA

Full Name	:	Abdulmajeed Hasan Yahya Hendi
Place & date of Birth	:	Hajjah, Yemen, 1975
Nationality	:	Yemeni
Present address	:	Physics Department, King Fahd University of Petroleum & Minerals, Dhahran 31261, Saudi Arabia
Permanent address	:	Hajjah University, Department of Physics, Hajjah, R. O. Yemen
Email	:	ahendi@kfupm.edu.sa
		abutsneem@yahoo.com
Education	:	Philosophy of Doctorate in Physics from King Fahd University of Petroleum & Minerals, Saudi Arabia, December 2016
		Master of Science in Physics from King Fahd University of Petroleum & Minerals, Saudi Arabia, April 2012
		Bachelor of Physics from Sana'a University, Yemen, June 1998

Position held : Lecturer-B at Physics Department, King Fahd University of Petroleum & Minerals, Saudi Arabia (2013-2016)

Research assistant, Physics Department, King Fahd University of Petroleum & Minerals, Dhahran 31261, Saudi Arabia (2007-2012).

Graduate assistant at Physics Department, Sana'a University, Yemen, (2000-2006)

Publications

A. *Journal Papers:*

1. **A. H. Y. Hendi,** M. F. Al-Kuhaili, S. M. A. Durrani, M. M. Faiz, A. Ul-Hamid, A. Qurashi, I. Khan "Modulation of the Band Gap of Tungsten Oxide Thin Films through Mixing with Cadmium Telluride Towards Photovoltaic Applications", Materials Research Bulletin, Volume 87, March 2017, Pages 148–154.

2. **A. H. Y. Hendi,** M. F. Al-Kuhaili, S. M. A. Durrani "Chemical and optical properties of Mno_2 thin films prepared by reactive evaporation of manganese", International Journal of Research in Engineering and Technology, eISSN: 2319-1163, 2016, 320-328.

3. M. Saleem, M. F. Al-Kuhaili, S. M. A. Durranib, **A. H. Y. Hendi**, I.A. Bakhtiari and S. Ali, "Influence of hydrogen annealing on the optoelectronic properties of WO_3 thin films", International Journal of Hydrogen Energy, 40 (36), 12343, 2015.

4. **Abdulmajeed H. Y. Hendi**, Saleh I. Al Quraishi, and Nabil M. Maalej "Gas flow-controlled microwave combustion synthesis of bismuth oxide nanoparticles", J Nanopart Res, 16 (5) 237, 2014.

5. **A. H. Y. Hendi,** M. F. Al-Kuhaili, S. M. A. Durrani, M. M. Faiz, A. Ul-Hamid, A. Qurashi, I. Khan "Tunable visible light absorption of MoO_3-CdTe composite thin films", submitted to Thin Solid Films, Manuscript No. TSF-D-16-01256, Responses submitted to reviewers (In progress).

6. **A. H. Y. Hendi,** M. F. Al-Kuhaili, S. M. A. Durrani "Reactive evaporation of manganese oxide thin films", (to be submitted soon).

7. **A. H. Y. Hendi,** M. F. Al-Kuhaili, S. M. A. Durrani, **"**Effect of annealing on the structural and optical properties of bismuth oxide thin films**",** (to be submitted soon)

B. *Conferences:*

1. M. A. Gondal, **A. H. Y. Hendi**, **"**Synthesis and Characterization Of Cuo/ Bi_2O_3 Composite Thin Films Using Pulsed Laser Deposition Technique**"**, International Conference on **"**Oxide Thin Films for Advanced Energy Applications**"**, Bloomingdale, Illinois (13 - 16 July 2014) USA.

2. **Abdul Majeed H.Yahya**, "Synthesis and Characterization of Bismuth Oxide Nano-Powder produced by Microwave-assisted Combustion Method", Second Saudi Scientific Conference, Jeddah, Saudi Arabia, 28-31 March 2011.